UNIVERSITÀ DEGLI STUDI DI PADOVA

Sede amministrativa: Università degli Studi di Padova
Dipartimento di Fisica "Galileo Galilei"

SCUOLA DI DOTTORATO DI RICERCA IN FISICA
CICLO XX

In-beam test and imaging capabilities of the AGATA prototype detector

Direttore della Scuola: Ch.mo Prof. Attilio Stella
Supervisore: Ch.mo Prof. Santo Lunardi
Correlatore: Dott. Dino Bazzacco
Correlatore: Dott. Enrico Farnea

Dottorando: Francesco Recchia

31 gennaio 2008

Contents

Riassunto

La spettroscopia nucleare γ ad alta risoluzione è uno degli strumenti più potenti e sensibili per lo studio dei nuclei atomici. A partire dagli anni ottanta sono stati utilizzati array di rivelatori al germanio con schermi anti-Compton, che hanno permesso di scoprire nuovi fenomeni come ad esempio la superdeformazione nucleare.

È ora evidente che l'attuale generazione di rivelatori non avrà prestazioni sufficienti negli esperimenti futuri utilizzanti fasci radioattivi. Per questo sono in sviluppo nuovi rivelatori con una più elevata efficienza e risoluzione. La soluzione che è stata proposta negli ultimi anni si basa sulla possibilità di determinare la posizione e l'energia depositata dalla singola interazione di un fotone all'interno di un cristallo di germanio, e sulla capacità di ricostruire la sequenza delle interazioni attraverso sofisticati algoritmi di analisi dei segnali prodotti. I risultati di simulazioni Monte Carlo suggeriscono che un array di rivelatori al germanio che utilizzi queste tecniche, conosciute come *analisi di forma d'impulso* e *tracciamento* γ, raggiungerà le prestazioni richieste per un suo utilizzo in futuri esperimenti con fasci radioattivi. Attualmente due progetti mirano alla costruzione di un array di rivelatori di nuova generazione di questo tipo: AGATA in Europa e GRETA negli Stati Uniti.

Questa tesi descrive i risultati ottenuti durante il primo esperimento sotto fascio con un rivelatore prototipo di AGATA. L'obiettivo dell'esperimento era essenzialmente la misura della precisione con cui l'analisi di forma d'impulso determina la posizione dei singoli punti di interazione. Tale precisione gioca un ruolo fondamentale nel determinare le prestazioni finali dell'array.

Il capitolo 1 introduce brevemente i temi più attuali della spettroscopia nucleare, puntando alla necessità dello sviluppo di acceleratori per fasci radioattivi e di nuovi sistemi di rivelazione come AGATA.

Lo stato del progetto AGATA è riassunto nel capitolo 2, assieme a una breve introduzione ai principi del tracciamento γ e dell'analisi di forma d'impulso.

I risultati dell'esperimento sotto fascio con il cluster triplo prototipo di AGATA sono presentati nel capitolo 3, dove viene descritta in dettaglio l'analisi dati. Il confronto con i risultati di una realistica simulazione Monte Carlo suggerisce un valore per la risoluzione posizionale dell'ordine di 5 mm per fotoni di energia 1382 keV. Tale valore è considerato adeguato per raggiungere le prestazioni previste dallo spettrometro AGATA.

Nel capitolo 4 viene presentata una possibile tecnica per estrarre la risoluzione posizionale dei rivelatori di AGATA attraverso tecniche di Compton imaging. I risultati preliminari esposti confermano il valore ricavato dalla misura sotto fascio.

Introduction

High-resolution γ-ray spectroscopy is one of the most powerful and sensitive tools to investigate Nuclear Structure. Significant progress in this field was achieved through the use of arrays of Compton-suppressed high-purity germanium detectors, leading for instance to the discovery of phenomena such as nuclear superdeformation. However, it is apparent that the present generation devices are not suited to the expected experimental conditions at the planned and under construction radioactive ion beam facilities. Devices with higher efficiency and sensitivity should be developed. The solution which has been proposed since the mid-nineties relies on the possibility to determine the position and the energy deposition of the individual interaction points of a photon within a germanium crystal, and on the capability to reconstruct the photon scattering sequence through powerful signal analysis algorithms. The results of Monte Carlo simulations suggest that indeed an array of germanium detectors using such techniques, which are known as *Pulse Shape Analysis* and *γ-ray tracking*, will reach the performance required to operate effectively at the future radioactive ion beam facilities. Presently, two major projects aim at the construction of an array of germanium detectors based on the pulse shape analysis and γ-ray tracking techniques, namely GRETA in the USA and AGATA in Europe.

The present work describes the results obtained during the first in-beam test performed with the prototype detector of AGATA. The goal of the experiment was essentially to measure the precision on the position of the individual interaction points extracted with pulse shape analysis algorithms. Such a precision plays an essential role in determining the overall performance of the array.

Chapter 1 deals briefly with the most actual topics in Nuclear Structure studies, pointing to the necessity to develop new generation radioactive ion beam facilities, as well as new detection systems such as AGATA.

The status of the AGATA project is reviewed in Chapter 2, together with a short introduction to the principles of γ-ray tracking and of pulse shape analysis.

The results from the in-beam test with the AGATA prototype detector are presented in Chapter 3, where the data analysis procedure is described in detail.

Finally, in Chapter 4 a possible technique to extract the position resolution of the AGATA detectors through Compton imaging techniques is presented, together with some preliminary results.

Chapter 1

Nuclear Structure through in-beam γ-ray spectroscopy

The continuous development of beams and instrumentation has been crucial for Nuclear Structure studies. The experimental findings that have guided this field come from the exposure of nuclei to external probes and the study of their response under extreme conditions. Whenever innovative experimental techniques for accelerating and detecting particles and radiation have been developed, new and quite often unexpected features have shown up.

High-resolution γ-ray spectroscopy is one of the most sensitive tools at our disposal to study in detail the structure of nuclei. This leading role was achieved thanks to the technological advancements which culminated with the construction of large arrays of Compton-suppressed germanium detectors.

In this chapter, some of the current topics in Nuclear Structure will be reviewed, with particular care to the techniques required to address them and the new instrumentation needed when approaching exotic nuclei far from stability.

1.1 Nuclear structure at the extremes

The nucleus is a many-body quantal system composed of A nucleons (Z protons and N neutrons). Other quantum numbers characterising the state of a given nucleus are the third component of the isospin $T_z = (N - Z)/2$, its total angular momentum J and its excitation energy E. In alternative

to the excitation energy, a temperature parameter T is often used, which is actually related to the density of excited levels. Current topics in Nuclear Structure deal with the properties of nuclei at "extreme" values of spin, temperature and isospin. As sketched in figure 1.1, angular momentum is transferred to the nucleus, producing rapidly rotating nuclei, or the nucleus can be heated (temperature degree of freedom), or very proton- or neutron-rich nuclei can be formed (approaching and mapping the drip-line regions). Much work has been carried out in the past concerning the properties of nuclei with extreme values of spin and temperature, leading to the observation of phenomena such as nuclear superdeformation [1, 2] or giant dipole resonances [3]. The isospin degree of freedom remains largely unex-

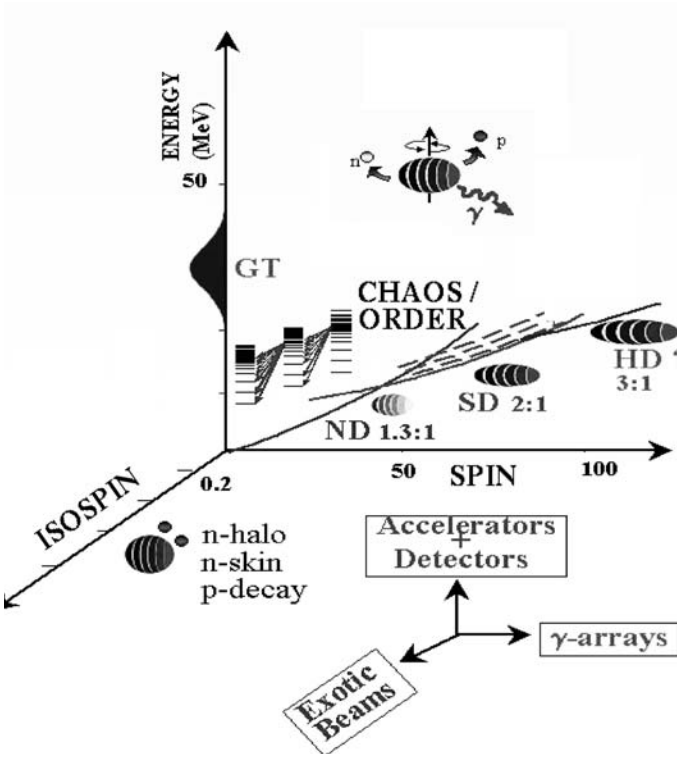

Figure 1.1: Schematic representation of the nuclear phase space displaying a variety of new perspectives in the study of Nuclear Structure Physics. The three dimensions of spin, isospin and temperature will be accessible to exploration with a combination of experimental probes composed of multi detector arrays for γ-rays, exotic beams and recoil mass spectrometers.

plored because of the experimental difficulties involved. In fact, contrary to the spin and temperature degrees of freedom, in order to produce nuclei with "extreme" values of isospin it will not be sufficient to increase the energy or the intensity of existing beams, but new (unstable) beams should be eventually developed.

There are many combinations of neutrons and protons which can form a nucleus of a given mass. Almost 300 stable nuclei exist, which are indicated by the black squares in figure 1.2. All other nuclei ultimately convert to a stable nucleus by a chain of radioactive decays which can have lifetimes ranging from nanoseconds to millions of years. Typically one or two stable isobars exist for each mass. Over 2500 nuclides are known and they are shown in blue in figure 1.2. However, there could be as many as an additional 5000 nuclei that have yet to be discovered. Potentially bound nuclei as predicted by Tachibana et al. [4] are shown in red.

The limits of nuclear stability provide a key benchmark of nuclear models. These limits also highlight the emergence of new phenomena leading

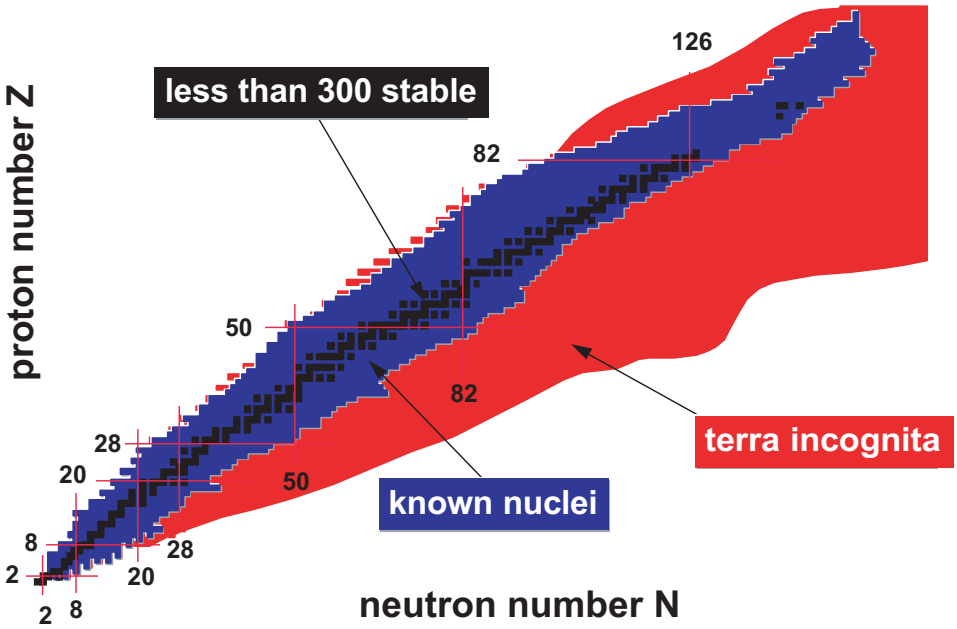

Figure 1.2: Isotope chart. The stable nuclei are shown as black squares; the observed unstable nuclei are shown as blue squares, while the expected (not yet observed) bound nuclei are shown as red squares.

to extra binding and an extension of the expected limits of stability, as it has been discovered for halo nuclei [5]. The limits of binding for extremely neutron-deficient nuclei and the location of the proton dripline are fairly well defined, but very little is known about the limits of binding of very neutron-rich nuclei and the location of the neutron dripline, which are established experimentally only for the eight lightest elements [6]. Actually it is experimentally easier to populate proton-rich nuclei with reactions using stable projectiles and targets, since in these cases the charge equilibration processes tend to unfavour the population of neutron-rich nuclei. Anyway multi-nucleon transfer and deep-inelastic reactions with heavy ions stable beams became recently a well established method for exploring moderately neutron-rich nuclei. In order to study neutron-rich nuclei very far from stability, new tools should be developed such as radioactive ion beams. Detailed studies of nuclear properties in heavy neutron-rich nuclei far from the line of stability will allow stringent tests of current theories of Nuclear Structure in a new territory and will drive the development of nuclear models with greatly improved predictive power. Indeed, there is broad agreement in the science community that the critical path to improvements in nuclear modelling passes through neutron-rich nuclei far from the line of stability. Their properties must be known to determine the effective degrees of freedom and constrain the effective interactions such as the tensor force [7], the symmetry energy [8], and isospin dependent three-body forces [9] which are, so far, only poorly determined.

In the following, some of the topics related with the study of neutron-rich nuclei will be discussed more in detail.

1.2 Exploring changes in shell structure

An important concept for the description of nuclear properties is that of single-particle motion in an average mean field. In nuclei near stability, bunchings of low-lying energy levels with related pronounced shell gaps are observed, which are ultimately caused by the spin-orbit interaction. As a consequence, certain numbers of protons and neutrons (the *magic numbers*) correspond to particularly stable nuclei. The location and size of shell gaps depend on the specific details of the mean field and the residual interaction between the valence nucleons.

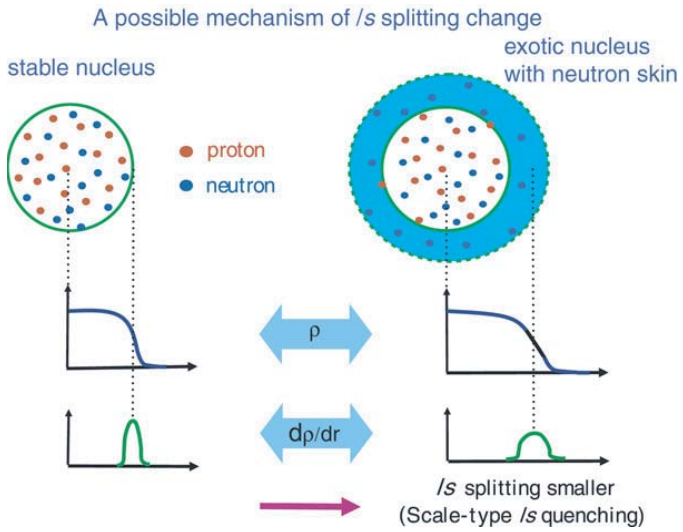

Figure 1.3: Scale-type *ls* quenching. In neutron-rich nuclei the spin-orbit force should be weaker as a consequence of the diffuseness of nuclear surface.

Huge extrapolations are needed in order to make predictions on exotic nuclei using the models developed and tested on the isotopes near the stability line. Hence, many theoretical schemes have been proposed. Considering that the spin-orbit force, being proportional to the radial derivative of the potential, may be weakened with a diffuse surface region (see figure 1.3), it is expected that the magic numbers identified near stability could change for neutron-rich nuclei (figure 1.4) because of the presence of a diffused neutron surface (or *skin*) [10]. Some calculations indicate that, near the neutron drip line, one may encounter quenching of existing shell gaps or perhaps even the emergence of new magic numbers. This is called *scale-type ls quenching* [10].

Another model is under development, predicting a different shell model evolution towards more exotic nuclei. Otsuka et al. started from Weinberg's Chiral Perturbation Idea [12] to make predictions on the parameters entering the general form of a potential for elastic, non relativistic nucleon-nucleon scattering. Two additional terms [13] should be considered in the nuclear Hamiltonian, because of their importance in the description of neutron-rich nuclei. The former term produces an attraction between a proton and a neutron in a spin-flip partner orbits. In other words,

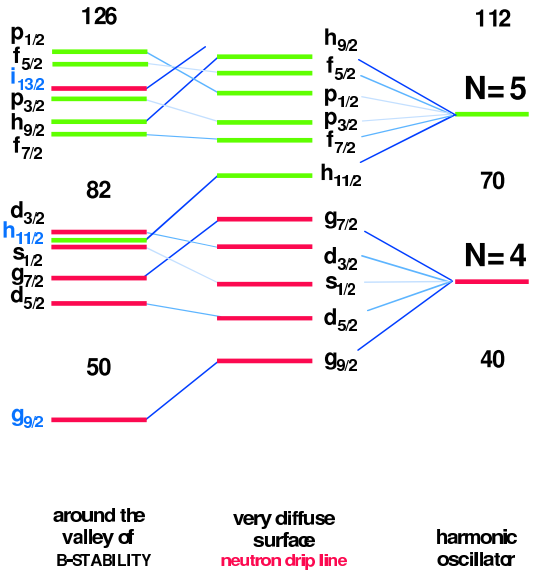

Figure 1.4: Possible evolution of shell model orbitals moving towards more exotic nuclei [11].

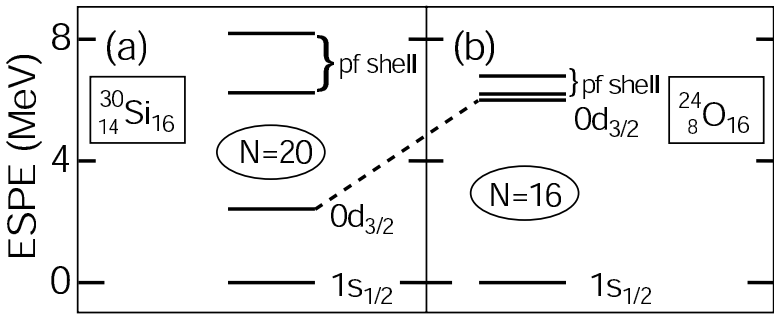

Figure 1.5: Effective single-particle energies for (a) ^{30}Si and (b) ^{24}O relative to $0d_{5/2}$. Figure taken from [15].

if a proton is in $j_> = l + 1/2$ and a neutron is in $j_< = l - 1/2$ (or vice versa), they attract each other. This means that, if the proton $j_>$ orbit is filled, the neutron $j_<$ orbit is lowered and its single-particle energy becomes smaller. An example of this mechanism is reported in figure 1.5 [14]. Both ^{30}Si and ^{24}O have $N = 16$. Valence protons are added in the $0d_{5/2}$ orbit as Z increases from 8 to 14. The energy of the $0d_{3/2}$ neutron orbit is thus lowered as a consequence of the attraction of the $0d_{5/2}$ proton orbit that is being

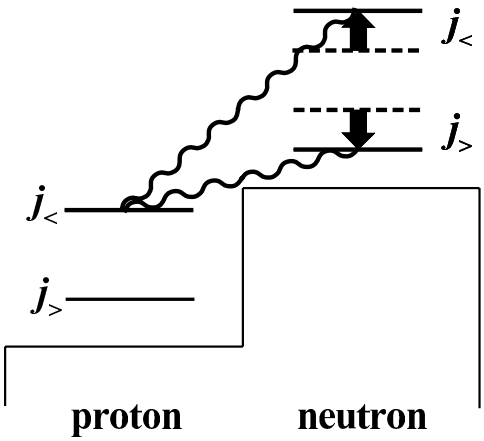

Figure 1.6: Schematic picture of the monopole interaction produced by the tensor interaction [17].

filled and a new gap appears.

Another term predicted to be important in the shell evolution is the tensorial term. The monopolar part of this interaction has been studied by Otsuka [16], in order to predict the changes on the effective single-particle energies. Neglecting the higher multipoles, the excited level pattern for the neutron-rich nuclei does not change. The monopole part of this interaction acts as depicted in figure 1.6 [17]. Differently from the former term, the tensor interaction acts also between nucleons with different orbital angular momentum and it is also predicted to be stronger. The radial wavefunctions of the two orbits must be similar in order to have a large overlap in the radial direction. This is fulfilled if the two orbits are both near the Fermi energy, because their radial wavefunctions are rather sharply peaked at the surface. For the same radial condition it is predicted that larger orbital momentum enhances the tensor monopole effect.

This model is in good agreement with the experimental findings, as shown for instance by the plot of figure 1.7. The energy difference between the $1h_{11/2}$ and the $1g_{7/2}$ proton orbitals, deduced from the structure of the known antimony isotopes [6], is compared to two different theoretical calculations. The former has been performed with the D1S interaction [19] used in the past for calculations in the same mass region, while the latter has been performed with the GT2 interaction developed by Otsuka and collaborators [7], which includes the tensor monopole force. It is clear that only

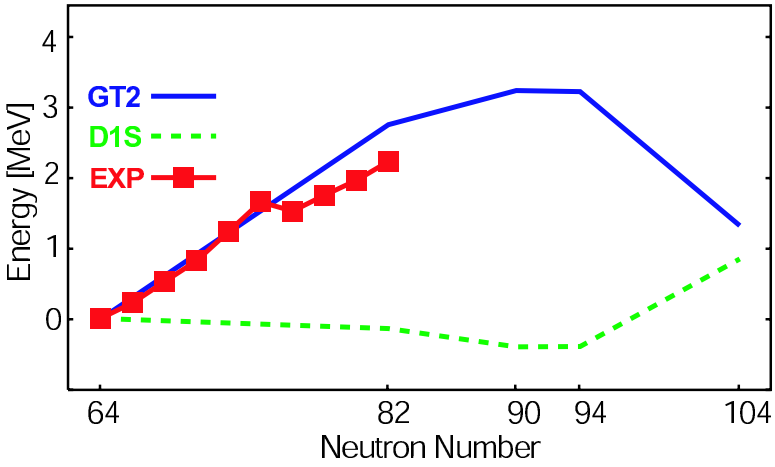

Figure 1.7: Evolution of $1h_{11/2}$-$1g_{7/2}$ shell gap in Sb isotopes. The difference from the value of $N = 64$ is plotted for experimental data [18] and calculated with GT2 [7] (with tensor monopole force included) and D1S interactions [19]. See text for details.

with the inclusion of the tensor monopole force the theoretical calculations and the experimental data are in good agreement.

Some consequences of these theoretical predictions on the shell evolution have been pointed out. A change in the magic numbers is expected [14] (see figure 1.8) and indeed new ones have been discovered in the recent years ($N = 16$, $N = 32$ ...) whereas, well established ones may disappear (e.g. $N = 20$, $Z = 14$). In looking for new (sub)shell closures the most sensitive and direct signature can be derived from binding energies. The second differences

$$\begin{aligned} \delta_{2n}(Z,N) &= S_{2n}(Z,N+2) - S_{2n}(Z,N) \\ \delta_{2p}(Z,N) &= S_{2p}(Z+2,N) - S_{2p}(Z,N) \end{aligned} \tag{1.1}$$

where

$$\begin{aligned} S_{2n}(Z,N) &= BE(Z,N) - BE(Z,N-2) \\ S_{2p}(Z,N) &= BE(Z,N) - BE(Z-2,N) \end{aligned} \tag{1.2}$$

show a distinct peak for closed-shell nuclei and its height represents the shell gap. However, a basic change of the underlying nuclear structure, as, e.g., quadrupole correlations, can severely distort δ, since the binding

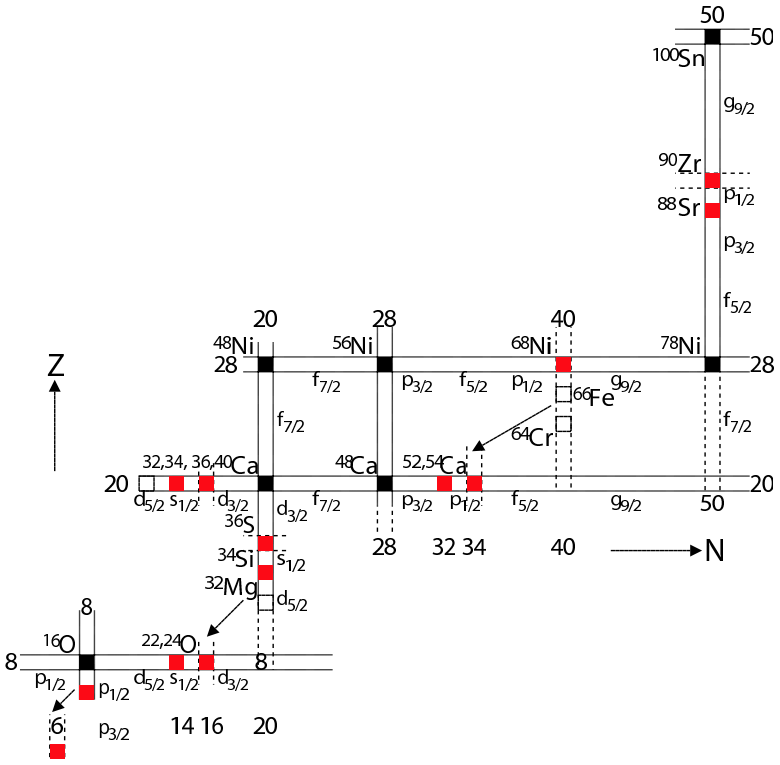

Figure 1.8: Schematic chart of known and expected new shell structure in $N \gg Z$ nuclei. Known and new closed shell nuclei are indicated respectively as full and hatched squares [14].

energies of three nuclei are involved in equation 1.1. More indirect measures for shell closures are the excitation energies of the first excited 2^+ states, $E(2^+)$, and the reduced transition strength, B(E2;$2^+ \rightarrow 0^+$). In figures 1.9 and 1.10 [20, 21] the $\delta_{2n/2p}$, B(E2) (in Weisskopf units) and $E(2^+)$ are shown for the closed shells $Z = 8$, $Z = 20$ and $Z = 28$. To demonstrate the isospin symmetry and to integrate the scarce data, the mirror nuclei with $N = 8,\ 20,\ 28$ are overlapped. The known magic nuclei, such as ^{16}O and ^{40}Ca, clearly stand out in these plots, and evidence for semimagicity of others, e.g. ^{34}Si, can be found.

The study of neutron-rich nuclei, as stated above, is one of the most actual themes of contemporary Nuclear Structure investigations. These studies are currently being pursued in several facilities, both using stable and unstable beams. For instance, a campaign of experiments has been recently

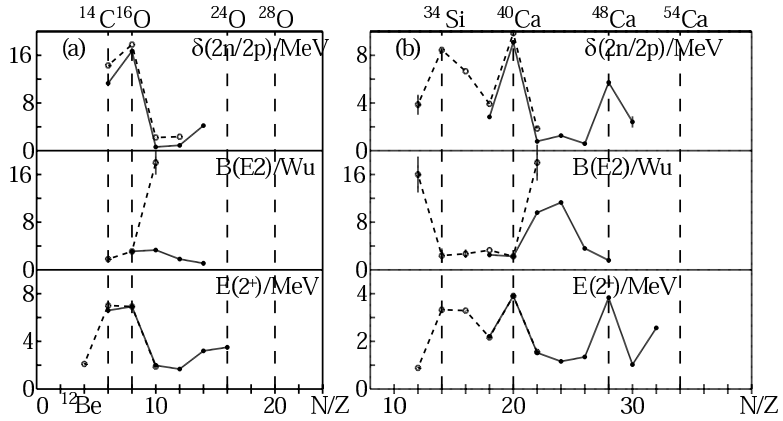

Figure 1.9: Shell signatures $\delta_{2n/2p}$, B(E2;$2^+ \rightarrow 0^+$) and $E(2^+)$ for shell evolution of nuclei. (a) $Z = 8$ oxygen isotopes (full-line) and $N = 8$ isotones (dashed); (b) $Z = 20$ calcium isotopes (full-line) and $N = 20$ isotones (dashed). [20]

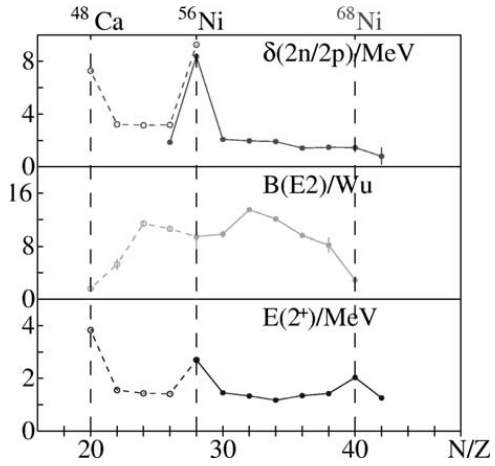

Figure 1.10: Shell signatures $\delta_{2n/2p}$, B(E2;$2^+ \rightarrow 0^+$) and $E(2^+)$ for shell evolution of $Z = 28$ nickel isotopes (full-line) and $N = 28$ isotones (dashed). [21]

carried out at the Laboratori Nazionali di Legnaro using the CLARA array of Clover detectors [22] in coupled operation with the PRISMA magnetic spectrometer [23]. The persistence or disappearance of the known shell gaps for large values of N/Z has been one of the main subjects of the experimental campaign. The moderately neutron-rich $N = 50$ isotones

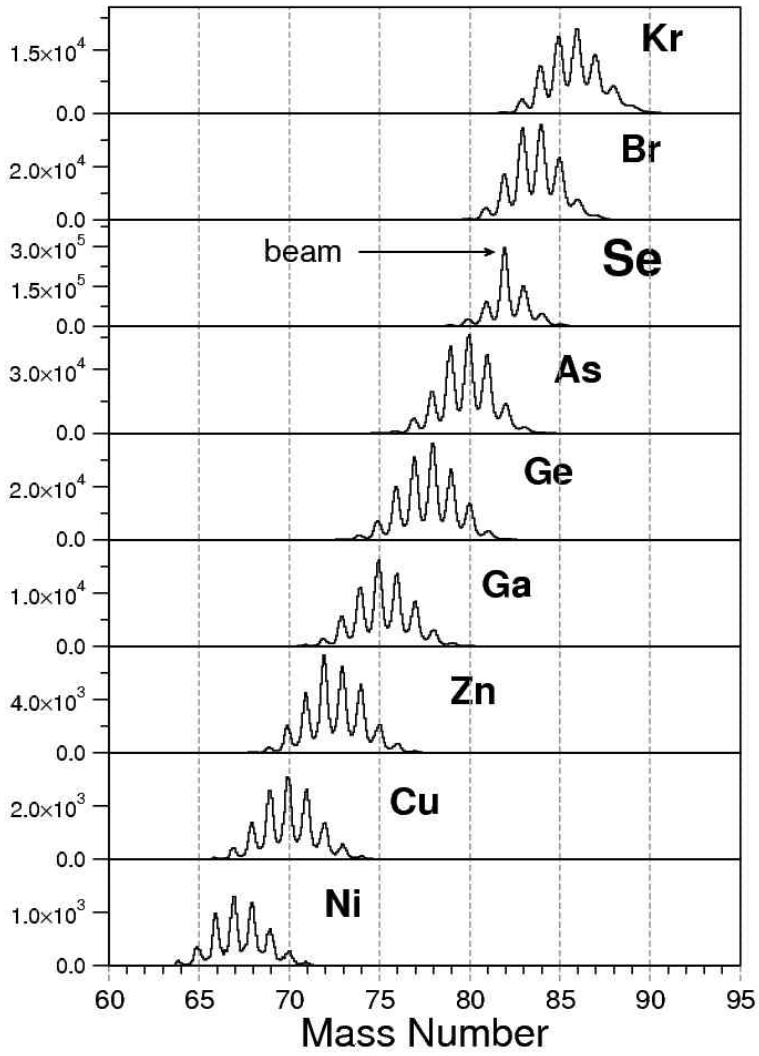

Figure 1.11: Mass distribution for the Kr to Ni isotopes populated in the ^{82}Se (505 MeV) + ^{238}U experiment.

have been studied in a series of measurements [24]. An example of the results obtained is presented in figures 1.11 and 1.12, both of which refer to an experiment performed with the ^{82}Se(505 MeV)+^{238}U reaction, where the beam was delivered by the Tandem-ALPI accelerator complex. The PRISMA spectrometer was placed at the grazing angle, in order to select mainly the quasi-elastic projectile-like reaction products from the multi-nucleon transfer process. More than 50 nuclear species were produced,

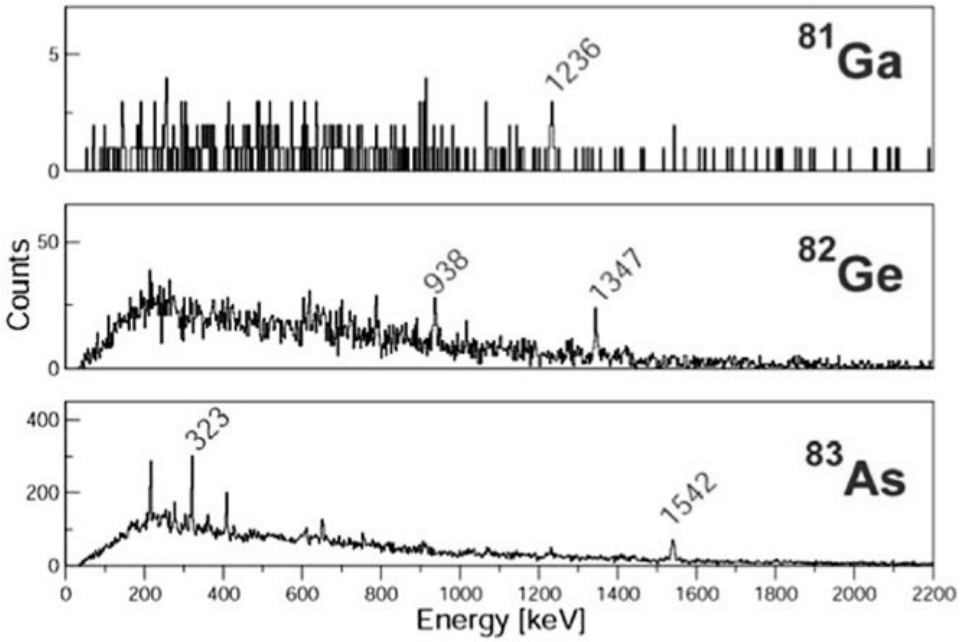

Figure 1.12: Doppler-corrected γ-ray spectra measured with the CLARA Ge-detector array for $Z = 31,\ 32,\ 33$ and $N = 50$ selected with the PRISMA spectrometer [25].

ranging from krypton to chromium isotopes, as shown by the mass distributions of figure 1.11. Sample spectra for some of the $N = 50$ isotones are shown in figure 1.12. The overall good agreement found between the shell-model calculations and the experimental data indicates that for the $N = 50$ isotones there is no evidence of a substantial reduction of the $N = 50$ shell gap down to ^{81}Ga [25].

Studies such as those performed with CLARA-PRISMA are currently at the limit of feasibility, on one hand because of the difficulty to populate the nuclei of interest with combinations of stable projectiles and targets, on the other hand because of the limitations of the experimental set-up, making it impossible, for instance, to collect $\gamma\gamma$-ion coincidences with adequate statistics and quality of the spectra. New facilities are needed in order to push these studies to more and more neutron-rich nuclei. It is necessary both to enhance the rate of production of such exotic nuclei by using unstable beams with large values of N/Z and to push the observational limits of the detection systems to weaker and weaker reaction channels.

1.3 Radioactive beam facilities

It is evident in the international Nuclear Structure community that the future developments in this field of research will depend strongly on the planned radioactive beam facilities. In fact, only using exotic projectiles it will be possible to study more and more exotic nuclei as discussed in the previous section.

Over the last decade the nuclear research community has undertaken the development, implementation and exploitation of the necessary new techniques, resulting in the commissioning of first-generation radioactive ion beam facilities and in the upgrade of existing facilities. The radioactive beam facilities in Europe at GANIL [26] and GSI [27], together with their counterparts at RIKEN [28], Japan, and MSU [29], USA, developed methods for extracting significant nuclear structure information from scattering experiments with intermediate-to-high energy secondary beams of unstable nuclei, although restricted to nuclear masses up to $A = 50$ and intensities up to 10^5–10^7 pps, which should be compared with the 10^{11} pps of a stable beam. Given the low beam intensities, the nuclear structure information is typically obtained through direct reactions such as single-nucleon transfer or Coulomb excitation. Even in the most favourable cases, it is extremely difficult, if not impossible, to identify high-spin states with these techniques. In particular, using γ-spectroscopy, it is very difficult to study excited levels lying above the first excited state. Therefore, an increase in beam intensities by several orders of magnitude is mandatory, involving a large number of technological challenges. Most of these have been identified, but for certain cases major R&D work is needed to find suitable solutions.

Beams of exotic nuclei can be produced in two complementary ways: the In-Flight separation method (IFS) and the ISOL method.

In the In-Flight Separation scheme, a heavy-ion beam at very high energy (of the order of 40–2000 MeV / u) collides with a target, resulting with high probability in projectile fragmentation. After the primary target area, a complex system, composed of electric and magnetic separators and degraders, selects the desired isotopes, which can be focused to the secondary target position for the studies of interest. This technique is used, for instance, at the RISING facility of GSI Darmstadt [30].

In principle, all ions lighter than the initial beam are produced, but only

the ones reasonably close to the primary beam have high enough intensities to create secondary beams that are useful for more than particle identification. The limit on the lifetime of the secondary beam ions is determined only by the flight-path through the separators and the velocity of the beam. Typically, nuclei with lifetimes down to the microsecond region can be studied. This allows for identification of very exotic species, such as ^{48}Ni which was recently shown to be bound by fragmenting a ^{58}Ni beam on a nickel target [31].

The experimental conditions at an IFS facility will be extremely challenging for γ-spectroscopy. The typically high energies and large emittance of the secondary beams point to a detector with very high effective granularity in order to perform good quality Doppler correction. As mentioned above, the intensities of these beams will be orders of magnitude lower than the intensities at the existing stable beam facilities and the nucleus of interest will have to be detected in a hostile environment, as the result of the cocktail of nuclear species reaching the secondary target and of the decay of part of the secondary beam. Hence, detection efficiency and selectivity will be essential.

In the Isotope Separation On-Line (ISOL) technique, the primary beam is typically composed of very light ions, such as protons and deuterons, hitting a bulk production target. In some cases, a converter target is used. The primary beam interacts with such a converter, releasing neutrons, which later induce reactions on the actual production target. The nuclei of interest can be extracted from the production target through chemical or physical methods. Following extraction, they are fed to an ion source and they are accelerated to the secondary target by means of "conventional" machines. As a result of this process, the quality of the secondary beam, in terms of energy and emittance, will be comparable to that of a stable beam from an existing facility. The drawback of the ISOL method is that the delay time from production to extraction of the secondary beam could be as high as several tens of milliseconds, thus making it impossible to accelerate the shortest-lived isotopes. The ISOL technique is used, for instance, in the ISOLDE facility [32] at CERN and it will be used in the planned EURISOL project [33]. It should be remarked that a project to build an ISOL facility at the Laboratori Nazionali di Legnaro has been recently approved. It is expected that the SPES (Study and Production of Exotic Species) [34] could be operational in the next few years.

As mentioned before, the quality in terms of emittance of the beams produced by the ISOL method will be less critic than what is expected at an in-flight facility. Anyway, the low intensity and purity of the beam will be a challenge for the detection and identification of the nuclei of interest. Also in this case, detection efficiency and selectivity turn out to be essential for γ-spectroscopy studies.

1.4 New instrumentation required for in-beam experiments with radioactive ion beams

As anticipated in the previous section, the new experimental conditions at the planned radioactive beam facilities will impose quite stringent requirements to the detection devices, strongly dependent on the reaction kinematics, i.e., beam energy and asymmetry of the projectile and target masses. Many results in the field of γ-spectroscopy have been obtained in the past few years, by using arrays of Compton-suppressed high-purity (HPGe) germanium detectors such as GASP [35, 36], GAMMASPHERE [37, 38] and EUROBALL [39, 40]. Given the technology on which such devices are based, it is apparent that these arrays will not meet the requirements

Reactions	Physics	Energy MeV/u	v/c %	γ Mult.	E_γ MeV
Fragmentation beams	Coulex, knock out, soft dipole	>70	>25	few	<5
Capture, inverse	Astrophysics	1-4	<10	low	<3
Coulomb Excitation:					
Inverse Kinematics	Collective properties	∼4	7-10	1-15	<5
Normal Kinematics	Collective properties	∼4	2-4	1-15	<5
Transfer Reactions:					
Inverse, heavy target	Single & multi-particle transfer	4-6	<10	<15	<3
Inverse, light target	Single-particle transfer	<15	<20	<5	<3
Normal, heavy ion	Single & multi-particle transfer	4-6	<7	<15	<3
Normal, light ion	Single-particle transfer	4-15	<3	<5	<3
Fusion:					
Inverse Kinematics	High spin, decay tagging, p-rich	4-5	<10	<25	<4
Normal Kinematics	High spin, decay tagging, p-rich	4-5	<6	<25	<4
Deep Inelastic Collisions:					
Inverse Kinematics	High spin, n-rich	>5	<10	<25	<5
Normal Kinematics	High spin, n-rich	>5	<5	<25	<3
Hot GDR	Giant Resonances	4-5	<6	<25	<25
Decay Tagging	Particle unbound, isomerism	4-5	<6	<25	<3

Table 1.1: Characteristics of reactions used for γ-ray spectroscopy.

posed by the planned and under construction radioactive ion beam facilities.

For instance, in the case of secondary beams produced following projectile fragmentation, very high velocities (v/c up to 50%) and low beam intensities (a few pps in the case of the most exotic species) are expected. Therefore, in order to perform γ-spectroscopy experiments, high photopeak efficiency (larger than $\epsilon_{ph} = 20\%$) should be combined with large granularity in order to keep the effective energy resolution, obtained following Doppler correction, below 1%. These values clearly exceed the possibilities provided by the existing devices, where the detection efficiency is typically lower than 10% for single photons and where, most importantly, such limiting resolution value is obtained at much lower recoil velocities, namely at $\beta \approx 5\%$. The situation is even worse at higher photon multiplicities since in this case the detection efficiency of the "conventional" devices drops rapidly with the increasing photon multiplicity.

Also in the case of reactions close to the Coulomb barrier, for instance fusion-evaporation reactions between heavy ions, the expected experimental conditions will be quite challenging. The expected photon multiplicities will be as high as 20–30, implying that high granularity will be essential to keep the probability of multiple hits within the same detection element to a minimum. On the other hand, also in this case Nuclear Structure studies with γ-spectroscopy techniques will require a detection efficiency as high as 20–25% for high photon multiplicity.

The expected situation for some cases interesting for γ-spectroscopy studies is summarised in table 1.1, together with the special requirements posed by the presence of background β and γ radiation originating from the decay of the secondary radioactive ion beams. It is altogether clear that the existing devices are not suited to perform γ-spectroscopy studies at the planned radioactive ion beam facilities, thus implying that new devices with much better performance should be developed. Following the discussion above, it is clear that such new instruments should have:

- high efficiency (larger that 30–40%) also at high multiplicities to allow the use of radioactive ion beams and the study of nuclei produced with a low cross section;
- good position resolution for the individual photon interaction points in order to perform good quality Doppler correction in case of pho-

tons emitted by fast moving recoils ($\beta > 20\%$);

- high granularity to minimise the probability of multiple hits even in case of high γ-multiplicity events;
- capability to stand a high count rate, to allow the use of high-intensity ion beams in experiments where the nuclei of interest are produced with a low branching ratio;
- high efficiency (larger than 5%) also for high-energy γ-rays;
- capability to measure Compton scattering angles to allow the measurement of the linear polarisation of photons.

It is also clear that it will not be feasible to push the technology of Compton-suppressed arrays to its limits in order to meet the requirements posed by the future radioactive ion beam facilities. An alternative solution has been proposed and investigated since the mid-nineties, which implies developments on the (digital) signal processing software rather than on the detector hardware alone. This technique requires the use of highly electrically-segmented germanium crystals combined with digital electronics in order to identify the positions of the single energy depositions within the crystals through a detailed analysis of the signal shape (*pulse shape analysis*). The energies of the individual photons will be subsequently extracted by powerful algorithms following (or *tracking*) the scattering sequences of each γ-ray.

Presently two major projects aim at the construction of an array of high-purity germanium detectors based on the novel concepts of *pulse shape analysis* and *γ-ray tracking*: AGATA [41] in Europe and GRETA [42] in the USA. These techniques will be reviewed in Chapter 2, together with a status of the AGATA project.

Chapter 2

The AGATA project

In this chapter the principles of γ-*ray tracking* and *pulse shape analysis* will be presented. The status of the AGATA project, aiming at the construction of an array based on such technologies, will be reviewed.

2.1 Arrays of germanium detectors

Major discoveries in the field of γ-spectroscopy have been triggered, in the past, by the technological achievements. Following the early works using inorganic scintillators, such as NaI(Tl), the major progress was the development of solid-state germanium detectors, namely Ge(Li) and HPGe crystals, which occurred around the end of the sixties. Given their intrinsic resolution, between one and two orders of magnitude better than a NaI(Tl) crystal coupled to a photomultiplier tube, high-resolution γ-spectroscopy became possible.

A limitation with the early, small-sized germanium crystals, having volumes of the order of 50 cm^3, was the large probability of photon escape following Compton scattering, resulting ultimately in poor response functions due to the large background generated. This limitation was overcome on one hand with the development of larger and larger crystals and on the other hand with the use of Compton-suppression shields, that is veto detectors shielded from the direct radiation and surrounding the germanium crystals. Using a germanium crystal with relative efficiency around 60%, that is having a volume of the order of 300 cm^3, a typical value of peak-to-total ratio is $P/T \approx 30\%$, which can increase up to 60% by using a Compton-suppression shield.

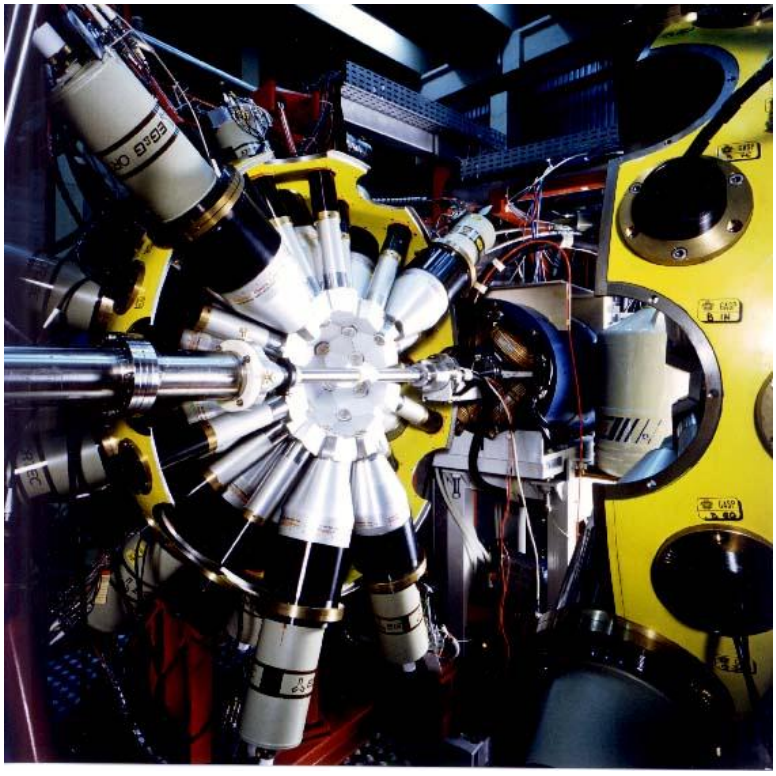

Figure 2.1: The GASP array. The beam is coming from the left. The Compton-shielded detectors and the multiplicity filter composed of BGO detectors are visible.

The final breakthrough in γ-spectroscopy occurred in the mid-eighties with the development of arrays of Compton-suppressed HPGe detectors. These devices have later become kind of standard tool and many valuable results have been obtained with devices such as GASP [35, 36] (a picture of which is shown in figure 2.1), EUROGAM [43], EUROBALL [39, 40] and GAMMASPHERE [37, 38]. It is clear that the future developments as well will rely on arrays of HPGe detectors and therefore it is convenient here to provide methods to properly characterise these devices.

The figure of merit characterising a multi-detector system is known as the *resolving power* of the array, which is a quantity proportional to the peak-to-total (P/T) ratio in the spectra and inversely proportional to the effective energy resolution of the detectors, including the Doppler broadening of peaks in case of in-flight emission of the photons.

These notions about multi-detector systems can be written down in a more formal way, as discussed in [44]. Imagine that one wants to study a cascade of M_γ transitions, populated with intensity α_0, with a mean separation SE_γ between the transitions. It is clear that only peaks standing out from the background can be properly identified. For instance, we could say arbitrarily [44] that a peak is identified when its peak-to-background ratio N_p/N_b is larger than 0.2 and its area is larger than 100 counts. The background consists of an uncorrelated, fold-independent part, coming from transitions that are not in coincidence with the cascade (both full-energy and Compton events), and of a correlated, fold-dependent part, coming from transitions in coincidence with the cascade (Compton contributions, statistical γ-rays, feeding transitions). Taking coincidences between $F \leq M_\gamma$ detectors, the peak-to-background ratio considering only the uncorrelated background can be calculated as [44]:

$$\left(\frac{N_p}{N_b}\right)_{(F)} = \alpha_0 R_0 (0.76R)^F \tag{2.1}$$

where R_0 is a background reduction factor coming from the use of external selection devices (namely, ancillary detectors) and R is a parameter called the *resolving power of the array*:

$$R = \left(\frac{SE_\gamma}{\Delta E_\gamma}\frac{P}{T}\right) \tag{2.2}$$

where P/T is the peak-to-total ratio and ΔE_γ can be taken as the resolution of the detectors. The factor 0.76, which is valid for gaussian peaks, originates from the fact that gates are normally put at the half-height of the peaks. It is clear that, in order to maximise the peak-to-background ratio, one has to maximise P/T and to minimise ΔE_γ, including the Doppler broadening of the peaks.

As mentioned earlier, for being properly identified a peak must stand above the background and it must have a minimum area. The probability of detecting an F-fold event is strongly dependent on the detection efficiency:

$$W(F) = \binom{M_\gamma}{F} \varepsilon_{ph}^F (1-\varepsilon_F)^{M_\gamma - F} \approx \frac{1}{F!}\varepsilon_{ph}^F \tag{2.3}$$

where the last approximation is valid for $F \ll M_\gamma$. It is clear that, for a fixed measurement time, since the probability of detecting F-fold events rapidly decreases with F, the area of F-dimensional peaks will decrease with F.

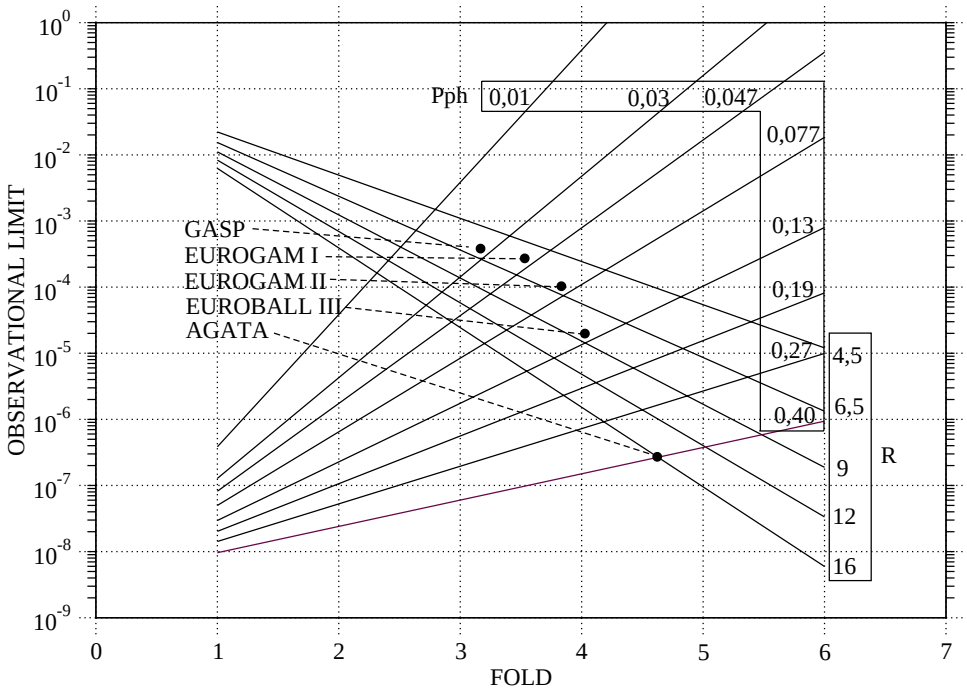

Figure 2.2: The observational limit of an array as a function of the resolving power and of the photopeak efficiency. The values for some arrays are presented, as well as the expected performance of the AGATA array evaluated through extensive Monte Carlo simulations.

The minimum intensity of a γ-ray transition that can be identified or, in other words, the *observational limit* I_o, depends on a balance between the resolving power and the efficiency of the multi-detector system. Working at higher folds the peak-to-background ratio improves, but the area of peaks decreases. The intersection of the two curves $I_o(R, F)$ and $I_o(\varepsilon_{ph}, F)$ defines the operating point of the spectrometer, that is it fixes the optimal fold at which the spectrometer should operate and the observational limit that can be reached, as shown in figure 2.2.

We can have a look at some numbers to get an idea of what has been reached in the recent past. The GASP array [35, 36], for instance, composed of 40 Compton-suppressed HPGe detectors, reaches a total photopeak efficiency $\epsilon_{ph} \approx 3\%$ for single 1.332 MeV photons and a peak-to-total ratio

$P/T \approx 60\%$. Each crystal covers a solid angle of approximately 30 msr, resulting in a resolving power $R \approx 6.5$ and in an observational limit of about $8 \cdot 10^{-4}$ at optimal fold $F = 3$.

The EUROBALL array [39, 40] was composed of 239 crystals, resulting in a larger photopeak efficiency $\epsilon_{ph} \approx 9\%$. The P/T ratio was around 60%, therefore similar to GASP, but with an increased granularity. In this case, $R \approx 9$ can be estimated, resulting in an observational limit almost one order of magnitude better than GASP, coming close to $1 \cdot 10^{-4}$ at optimal fold $F = 4$ (see figure 2.2).

Following the above discussion, it is clear that in developing an array of HPGe detectors a careful balance must be found between two contrasting needs. On one hand the detectors should be placed at large distances from the target position in order to subtend small solid angles with each element, thus keeping the effective energy resolution to acceptable values. On the other hand, in order to maximise the detection efficiency with a given number of detectors, each of them should be placed as close as possible to the target position. If the solid angle subtended by each element is limited because of the requirements on the effective energy resolution, a very large number of crystals might be needed in order to reach the required detection efficiency. In addition, the attainable detection efficiency is limited because the Compton-suppression shields cover a fraction of solid angle in which the high-resolution germanium detectors cannot be placed. The problem can be partially overcome by using composite detectors such as the Clover [45] and Cluster [46] detectors developed within the EUROBALL collaboration. In these detectors, more crystals (respectively 4 and 7) share the same cryostat and the same Compton-suppression shield. Efficiency and peak-to-total can be recovered by summing up (*adding back*) the energy deposited in neighbouring detectors.

This process could be taken to its extreme by conceiving an array composed solely of germanium detectors and performing Compton suppression through some “intelligent” add-back. Unfortunately, since each crystal should subtend quite a small solid angle (of the order of 1 msr) to keep double-hit effects and energy resolution to a minimum, thousands of crystals would be needed in order to reach a detection efficiency of the order of 25-30%, which would be hardly manageable and economically unfeasible. Furthermore, Monte Carlo simulations [41] suggest that such an array would reach P / T values around 30%. This means that the resolving power

of such an array would not be larger than the value for EUROBALL and that the increased price for the construction would not be justified.

In order to keep the solid angle subtended by each element to a minimum and at the same time cover a large fraction of the solid angle with a limited (around 200) number of crystals, a recently developed alternative relies on using electrically-segmented crystals, similar to those developed for MARS [47], MINIBALL [48], SeGA [49] or EXOGAM [50]. Early Monte Carlo simulations, however, proved that for such a device as well the attainable P/T ratio is no larger than 30% [41], resulting again in a resolving power comparable to existing devices such as EUROBALL and GAMMASPHERE. Also in this case the increased costs are not justified. It is therefore clear that, in order to build an array with a photopeak efficiency larger than 30%, having at the same time a P/T ratio around 60% and effective resolution better than 1%, new techniques have to be developed, implying using the detectors in a "smart" way.

Research and development on these new techniques, known as *γ-ray tracking* and *pulse shape analysis*, is being carried out since the mid-nineties. Presently two projects, AGATA in Europe [41] and GRETA in USA [42], aim at the construction of an array of highly-segmented HPGe detectors based on these techniques, which will be briefly reviewed in the following sections.

2.2 Principles of γ-ray tracking

Charged particles deposit their energy in matter through a continuous ionisation track, which can be followed (tracked) through the detector directly or indirectly through the temporal sequence of ionisation charges collected (in time projection chambers). The situation with the γ radiation is completely different as the photon energy is deposited in matter through discrete events which, being separated by macroscopic distances, often can not be directly associated to the photon that generated them. The situation is even more complicated for high γ-multiplicity events, where energy depositions generated by different photons can be geographically close as shown for instance in figure 2.3. These simulated data were produced by considering an ideal germanium shell covering the full 4π solid angle around a point source position emitting 1.33 MeV photons. The inner and outer ra-

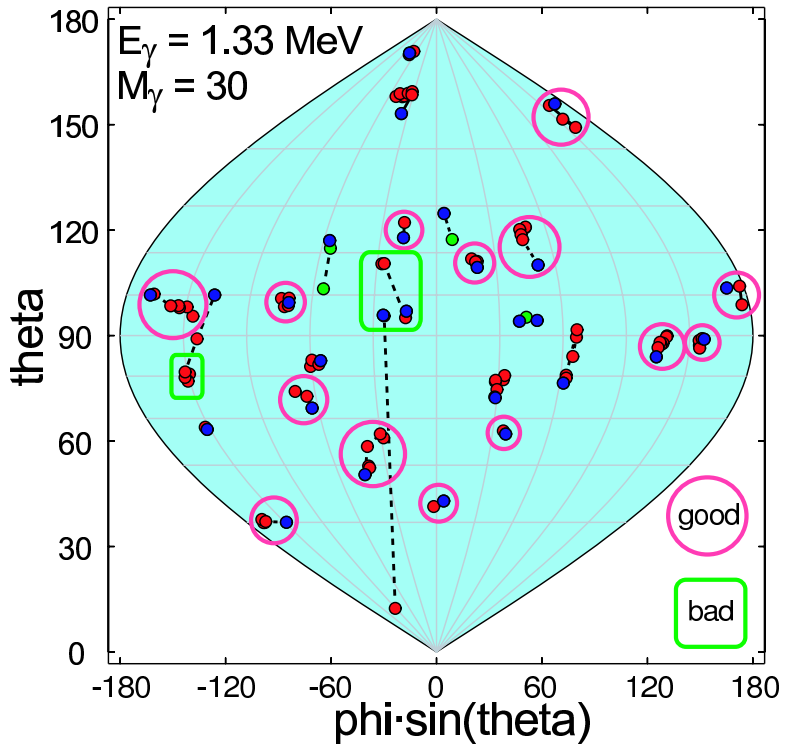

Figure 2.3: "World map" representation of an E_γ = 1.33 MeV, M_γ = 30 event detected in the ideal germanium shell and reconstructed with the "cluster-tracking" algorithm. Correctly reconstructed transitions are encircled; the two rectangles represent badly reconstructed events.

dius of the shell were $R_{int} = 15$ cm, $R_{out} = 24$ cm. In the case of figure 2.3, $M_\gamma = 30$ photons emitted in coincidence were considered. The first interaction point of each detected photon is marked in blue, the other points being drawn in red if the γ-ray is fully absorbed or in green if partly escaping. The interaction points were plotted according to their (θ, ϕ) angles in a polar coordinate system centred at the source. In this representation, some points (grouped with rectangles) are geographically close although generated by different photons. More details on this plot will be given later.

In principle, if the individual interaction points are known with sufficiently high precision, the scattering sequence of each photon could be disentangled and followed (tracked). The algorithms performing *γ-ray tracking* must take into account both the physical characteristics of the interaction mechanisms of γ-rays and the geometry of the detector. For the en-

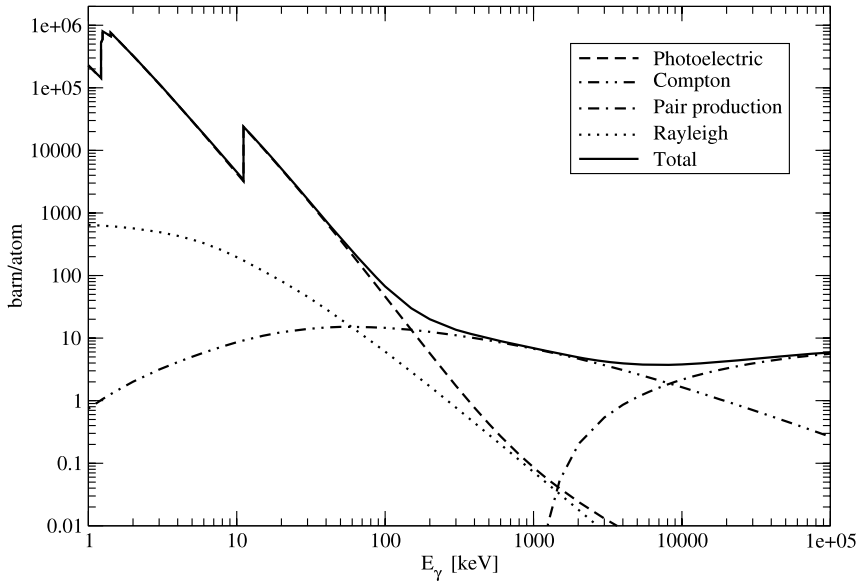

Figure 2.4: Interaction cross section for photons in Germanium [53]

ergy range of interest in Nuclear Spectroscopy, namely from 10 keV to a few tens of MeV, the interaction mechanisms that a photon can undergo in a solid state detector are restricted to photoelectric absorption, Compton scattering, electron-positron pair production and secondarily Rayleigh scattering [51, 52]. The relevance of each interaction mechanism as a function of energy is depicted in figure 2.4. It should be remarked that the most probable interaction for a photon in germanium is Compton scattering, which can be described analytically. Depending on the relative angle θ between the directions of the incoming and of the outgoing photons (see figure 2.5), the energy of the scattered photon takes the following value:

$$E'_\gamma = \frac{E_\gamma}{1 + \frac{E_\gamma}{m_e c^2}(1 - \cos\theta)} \tag{2.4}$$

This forms the basis for all the tracking algorithm developed so far.

In principle a γ-ray tracking algorithm should check which of the possible sequence within a set of points is compatible with the Compton scat-

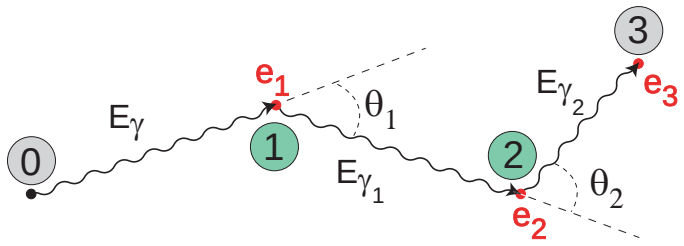

Figure 2.5: A photon going through two subsequent Compton scatterings and being finally photoabsorbed.

tering formula, as exemplified in figure 2.6. This is not feasible, in practice, in case of high-multiplicity events such as that shown in figure 2.3 because of the computational requirements. The problem can be reconduced to a treatable one by means of clustering techniques.

As the mean free path in germanium of the γ radiation with an energy around 1 MeV is approximately 3 cm, hence one order of magnitude smaller than the dimension of the full array, it is expected that the interaction points generated by a single photon will be localised in a small portion of the spectrometer. Clusters can be identified through several techniques, based ei-

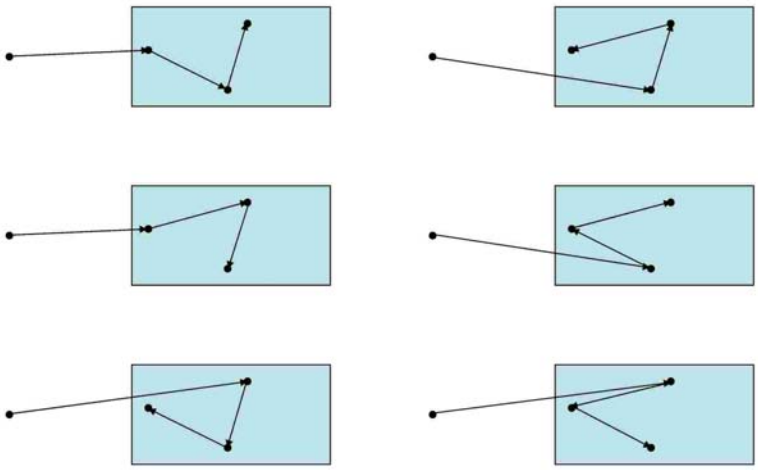

Figure 2.6: All possible scattering sequences which have to be sampled during the γ-ray tracking procedure for a cluster with 3 interactions.

ther on angular proximity or on linear proximity, taking into account the amount of material in between the interaction points. For instance, in the case of figure 2.3, a clustering algorithm based on angular proximity was applied to the data [54]. In most cases the algorithm identifies correctly the clusters generated by a single photon (marked as circles), although it fails in a fraction of the cases (marked as rectangles). It is also important to remark that the three incompletely detected γ-rays are not accepted at all, meaning that the reconstruction algorithm acts as a high-performance Compton-suppression shield.

Following the identification of the clusters, each of them can be checked for Compton scattering as discussed above. Actually, two alternative approaches are possible. The first one, known as forward tracking, is the approach followed within the GRETA collaboration [55]. A similar approach has been followed in the Orsay tracking code [56], which is the "official" tracking code for AGATA, and in the `mgt` (Mars Gamma Tracking) code developed earlier in Padova [54], which was actually used to calculate the performance of the AGATA array. Assuming a given origin for the photons, the agreement of each sequence with the Compton scattering formula is evaluated, taking also into account the probability that the photon travelled inside the detector without undergoing other interactions and the probability of a Compton scattering with respect to the total interaction cross section. If a γ-ray undergoes a pair production interaction, the reconstruction is quite simple since the annihilation photons do not travel long distances, thus resulting in a very characteristic pattern of the energy depositions. The clusters which are not accepted in this process can be rearranged together to form new clusters in an iterative procedure. Finally the remaining interactions are tested for photoelectric interaction on the basis of their travelling path inside the detector.

The alternative backtracking [56] approach relies on the empirical observation that the energy deposition in a photoelectric interaction usually lies within a narrow energy range (100–200 keV). The idea is to identify a candidate for a photoelectric absorption point and then to reconstruct a track back to the point of origin of the photons.

So far, the existing tracking algorithms have been developed on the basis of simulated data sets. The plot of figure 2.7 gives the photopeak efficiency of an ideal germanium shell (inner radius 15 cm, outer radius 24 cm) covering the full 4π solid angle around the source position. A point source

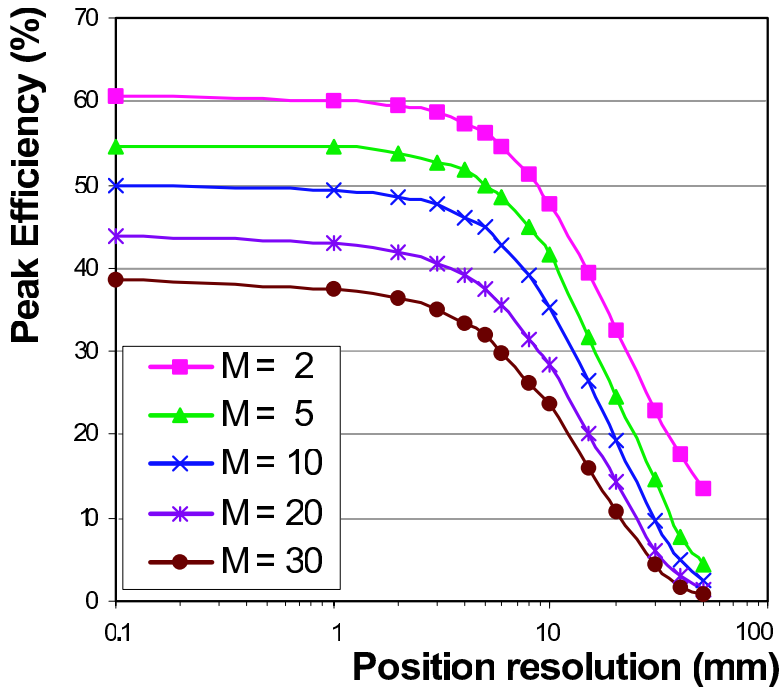

Figure 2.7: Photopeak efficiency of an ideal germanium shell for 1.332 MeV photons as a function of the position resolution. Tracking is performed. The different colours give the performance for different photon multiplicity.

at rest emitting 1332 keV γ-rays was considered. It was assumed to localise the individual interaction points with different position resolution. It is clear that in order to obtain photopeak efficiencies close to the limiting values (obtained with zero positional error) the interaction points should be measured with a precision of a few millimetres at most. In other words, even considering highly electrically-segmented detectors, techniques to go at sub-segment precision should be used, such as those outlined in the following section.

2.3 Pulse shape analysis

As discussed in the previous section, in order to obtain maximum values of photopeak efficiency for a γ-ray tracking array, sub-segment position resolution is required. The techniques used to obtain such a result rely on the detailed shape of the signals and are generally known as *pulse shape analysis*.

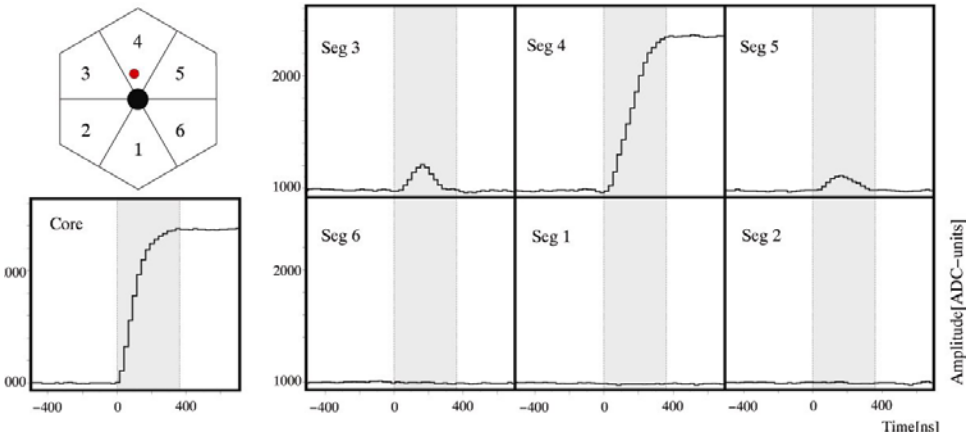

Figure 2.8: Signals produced in the core and in the segments for a 6-fold segmented detector when a photon is fully absorbed in segment 4. Since the interaction takes place closer to segment 3, the amplitude of the corresponding transient signal is larger than the amplitude for segment 5.

In principle, limited information could be obtained on the position of the interactions within a germanium crystal also with a conventional coaxial detector. Even with the simple model in the book by G.F. Knoll [57], it is clear that the radial position of the interaction can be extracted, in a coaxial detector, from the shape of the pulse. In order to extract more information, it is necessary to break the symmetry and to use electrically-segmented detectors.

The basic principle is that the drifting motion of the charges released following an interaction within the detector induces a signal not only in the segment where the actual interaction took place, but in the other electrodes as well. The main difference is that the signal of the segment where the interaction took place is a *net-charge* segment, with a non-vanishing integrated current, while, in contrast, the signals in the neighbouring segments are *transient* and the integral of the current over the collecting time is zero. Since the amplitude of the transient signals depends on the specific location of the primary interaction, this information can be exploited to deduce the position of the interaction. For instance, in figure 2.8 a 6-fold segmented detector is considered. A photon is fully absorbed in segment 4, inducing transient signals in the neighbouring segments 3 and 5. Since the interaction takes place closer to segment 3, the amplitude of the corresponding

transient signal is larger than the amplitude for segment 5.

This is basically the technique used with the MINIBALL detectors to extract the azimuthal coordinate of the interaction [48]. Unfortunately, this simple method cannot provide the kind of precision needed by the tracking algorithms and more sophisticated techniques had to be developed, involving digitisation of the signals from each segment and the comparison of the transient and net charge signals with a basis of reference signals (that is, a set of signals corresponding to interactions taking place in specific locations within the detectors).

Several algorithms have been developed and tested so far within the AGATA collaboration [58]. The method used in the present work is a simple grid search, consisting of a comparison between the recorded signals and the basis signals, which are sampled over a uniformly-spaced grid. A more detailed description of the algorithm, as well of the results obtained, will be given in section 3.7.

Since the construction of the reference basis is an essential ingredient for any pulse shape analysis algorithm, it is worth reviewing the techniques to measure and construct such basis.

2.3.1 Scanning tables

Several devices, known as *scanning tables*, have been developed within the AGATA collaboration in order to construct the reference basis needed by the PSA algorithms or, in other words, to measure in a semi-automatic way the signals corresponding to specific locations within the crystal (with the possibility to move such locations in any point of the detector).

In case a collimated photon beam is available, the position of the interaction can be determined by requiring the coincidence of the germanium signal with a second collimated detector, as schematised in figure 2.9. The main problem with this kind of measurement is that the constraints on the recorded events are stringent and as a consequence very long measurement times are needed to collect the required statistics. In addition, the measurement for points at the backward part of the detector is extremely difficult.

This technique is used in the scanning table built at the University of Liverpool [59, 60], which is shown in the pictures of figure 2.10. In order to save measurement time, the lateral collimation is actually performed through horizontal slits and the coincidence detectors, in this case BGO

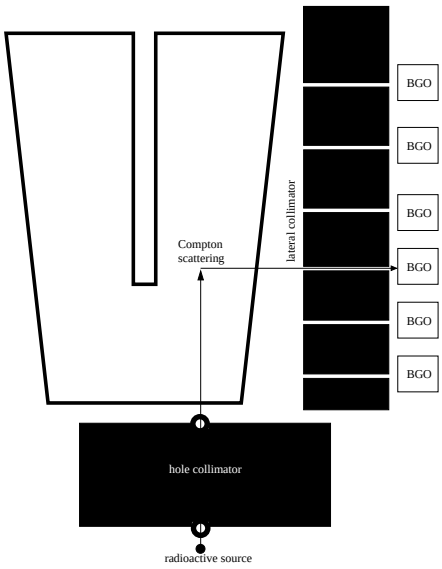

Figure 2.9: Schematic view of the scanning table in Liverpool. The collimated photon beam enters from the front face of the detector through a hole collimator. The trigger of the acquisition system selects only the events where the photon Compton scatters and the residual photon passes through a second collimator to reach one of the scintillator detectors placed around.

crystals, cover a 360° angle around the collimated incoming photon beam. The scanned point is therefore defined through the intersection of the photon beam (defined by the source collimator) and the orthogonal plane (corresponding to a scattering angle of 90°) defined by the slits. Further time can be saved by measuring simultaneously more interaction points, that is by defining more coincidence planes within the germanium crystal, as shown in figure 2.10.

It should be observed that, in principle, the information gathered with this kind of scanning table is redundant. In fact, the energy deposited by the photon inside the germanium detector is fixed by the geometrical arrangement since the source is monochromatic and the scattering angle fixed (with a minimum spread distribution around 90°). This information on the energy is used in combination with the equivalent information given by the coincidence detectors to clean the data from spurious events in which the photon underwent multiple Compton scattering.

The scanning table under development in Orsay [61] follows the same

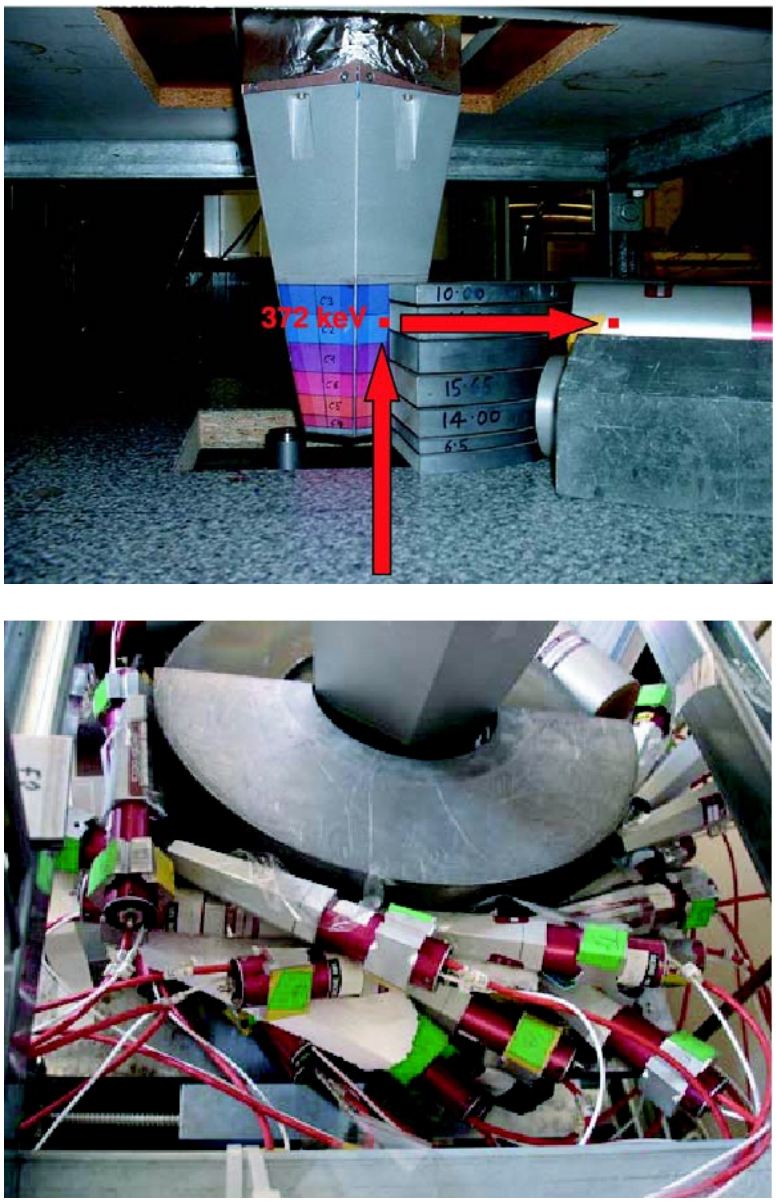

Figure 2.10: Photos of the scanning table in Liverpool [59]. The lateral collimation and the BGO detectors are visible. To enhance the counting rate the collimation covers the full 360° around the detector.

principle but a different strategy to reduce the time needed for a scan of the full detector. In this case an array of collimated NaI(Tl) scintillators is placed around the scanned detector as depicted in figure 2.11. The conver-

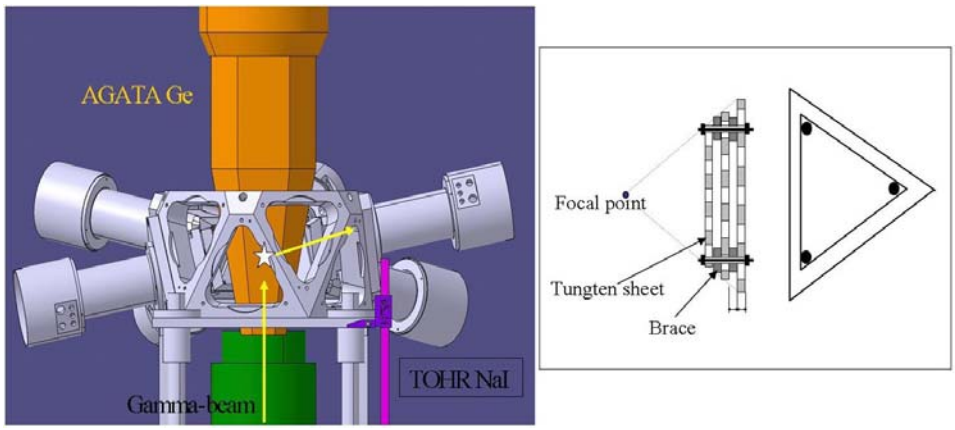

Figure 2.11: Drawing of the scanning table in Orsay (left) and of a NaI scintillator array with its convergent collimator. This setup will allow a fast scan of the detector thanks to the enhancement of the angular acceptance of the coincidence detectors.

gent layout of the collimators defines a point, through which the collimated incoming photon beam is sent. In this case, more scattering angles can be measured simultaneously, thus enhancing the angular acceptance with respect to the Liverpool scanning system, while preserving the accuracy in localisation of the interaction.

Other strategies are possible to decrease the time needed for a full scanning of the detector. For instance, it is possible to remove the front collimator and place a position-sensitive detector on the opposite side of the photon source instead, as schematised in figure 2.12. If a β^--decaying source is used, which emits two 511 keV photons following positron annihilation, the interaction position can be extracted by intersecting the lateral collimation plane with the line joining the firing position of the position-sensitive detector and the source. This method has actually been chosen by the GSI group working for AGATA [62] and the scanning table is under development.

2.3.2 Pulse shape calculations

Using the scanning methods presented in the previous section, it takes quite a long time (some months) to scan a full detector with a fine grid (1 mm x 1 mm x 1 mm). This means that years of scanning will be required to fully

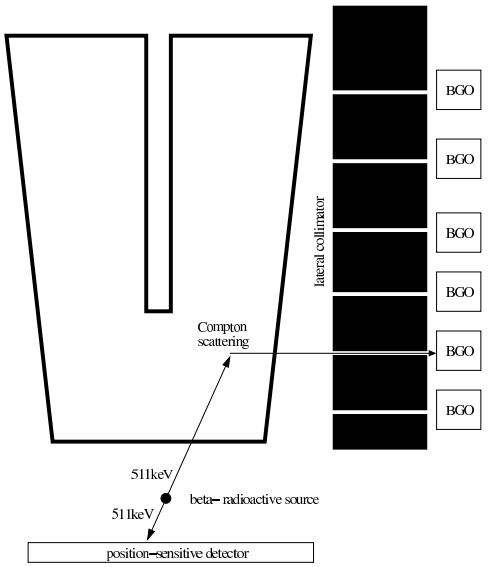

Figure 2.12: Schematic view of the scanning table under development at GSI. The β^--decaying source emits a positron that annihilates producing two 511 keV photons moving in opposite direction. One γ-ray is detected by a position-sensitive detector, the other one goes through a Compton scattering and, after passing through a lateral collimator, is detected by a scintillator.

characterise the detectors composing AGATA, which will be of the order of 200.

In principle, knowing the electric fields inside the detector, the signal shapes can be calculated and the data from the scanning tables can be used to tune the parameters of the calculations and to validate this "mathematical" solution. The sequence leading to the calculations is outlined in the following.

The interaction of nuclear radiation with matter generates primary charge carriers as energetic electrons or electron-positron pairs. While slowing down in the detector material, these primary charge carriers produce a large number of electron-hole pairs which are forced to drift to the electrodes (anode and cathode) by an electrical field. It is important to recognise [57] that the signals measured by the readout electronics correspond to the current induced at the electrodes by the moving charge carriers and that this current is only present during the motion and stops flowing once the charges

are fully collected. Following this scheme, the signals at the electrodes can be calculated by modelling, as precisely as possible, the steps described above. The interaction of nuclear radiation with matter and the generation of electron-hole pairs in semiconductor detectors are well known [57] and we will restrict here to a synthetic description of procedures related to the calculation of signals.

The (static) electric field inside the detector is calculated by solving the Poisson equation, which depends on the geometry of the crystal, the externally-applied high voltage and on the concentration and distribution of immobilised charges that build up in the depleted region as ionised residual impurities (positive charge for the donor atoms of n-type HPGe crystals). Due to the complicated geometry of the crystals, the Poisson equation has to be solved numerically. In principle this can be done with high accuracy but the actual precision is limited by the poor knowledge of the impurity concentration and profile. This is quoted by the crystal manufacturer as a range (typically $0.5 - 1.5 \cdot 10^{10}\,\mathrm{atoms/cm^3}$ for HPGe) and can only be measured with invasive techniques that destroy parts of the crystals. At this point the drift of the electrons and holes to the electrodes of the detector is calculated from their mobility ($\mathbf{v} = \mu_{e,h}\mathbf{E}$). The mobility is different for electrons and holes and is known to be a function of the local electric field strength and of its direction with respect to the crystallographic axis of the detector lattice. The factor limiting the accuracy of these calculations is again the incomplete knowledge of the mobility laws (in particular for the holes) and the uncertainty of the parameters.

Finally, from the motion of the charge carriers one can calculate the induced currents. To do this one should solve the Poisson equation for a large sequence of different charge configurations that exist during the collection time, but this is an extremely tedious and computing-intensive procedure which is rarely used. All practical signal calculations are instead performed using a much simpler procedure based on the Shockley-Ramo theorem [63, 64], which states that the signals induced by a charge (moving or not) on one of the electrodes of the system can be calculated by removing all other charges and solving the much simpler Laplace equation with a (unit) voltage applied to it and grounding all other electrodes. Due to the complicated geometry of any practical detector, the Laplace equation is also solved numerically. The fictitious electric field produced in this way is known as the *weighting field* $\mathbf{E}_w$ [65, 66] and the corresponding *weighting*

potential is called ψ_w. The induced current / charge is given by:

$$\begin{aligned} i(t) &= -\,q_m\,\mathbf{E}_w\left(\mathbf{r}(t)\right)\cdot\mathbf{v}(t) \\ q(t) &= -\,q_m\,\psi_w\left(\mathbf{r}(t)\right) \end{aligned} \tag{2.5}$$

Here, q_m is the moving charge and $\mathbf{v}(t)\,/\,\mathbf{r}(t)$ is its moving law as calculated from the actual electric field and charge mobility. In practice q_m is taken as unit (-1 and 1 for electrons and holes respectively) because the signal amplitude is normalised to the energy deposited in the interaction as a part of the standard calibration procedures. As the weighting field is calculated only once for each of the electrodes, the signals of an AGATA detector are determined by solving one Poisson and 37 (1 for the anode and one for each of the 36 segments of the cathode) Laplace equations. The final signal basis is then calculated by generating a unit negative (positive) charge on a predefined space grid (typically with a step of 1 mm in each dimension), by calculating on a fine time grid (typically every 1 ns) its motion until it is collected on the anode (one of the segments of the cathode). At each of the time steps the charge induced on each electrode is calculated and the two values are summed to obtain the final signal.

Many codes have been developed to calculate the signal shapes in segmented germanium detectors. An early example is reported in [47]. The code presently used by the AGATA collaboration is called MGS (Multi Geometry Simulation) [67] and it can calculate the signal shapes for interactions distributed over a regular cubic lattice having 1 mm step, at a sampling rate of 1 ns.

2.4 The AGATA project

The aim of the AGATA (Advanced GAmma Tracking Array) project is the development of an array of HPGe detectors based on the techniques of γ-ray tracking and PSA outlined in sections 2.2 and 2.3. Such an array will be suitable for Nuclear Structure studies at the planned radioactive ion beam and high-intensity stable beam facilities. The design goals for the array can be summarised as follows:

- efficiency larger than 40% for events with a photon multiplicity 1 and larger than 25% for events with a photon multiplicity 30;

- peak-to-total ratio around 60%;
- high granularity to minimise the probability of multiple hits even in case of high γ-multiplicity events;
- position resolution better than 5 mm FWHM for the single interaction point;
- capability to stand a counting rate up to 50 kHz for each germanium detector when used with high intensity stable beams;
- enough internal free space to host ancillaries detectors.

As a consequence of the tracking process, the AGATA array will have as well:

- high efficiency for high-energy γ-rays;
- capability to measure the polarisation of the detected photons.

The design values for the photopeak efficiency required to the AGATA array can be reached only by covering with germanium detectors a solid angle as close as possible to the 4π around the target position. In order to minimise the amount of passive materials, it was apparent from the beginning that the detectors should be grouped in clusters within the same cryostat, presumably into triple or quadruple clusters. As a matter of fact, clusters of more than four highly-segmented germanium detectors would almost be impossible to handle and operate, requiring too large a time for set-up and maintenance. Furthermore, it was decided to use encapsulated detectors, that is detectors hermetically sealed inside a thin walls aluminium can, similarly to the capsules of the cluster detectors developed for EUROBALL [46], to simplify the handling procedures for such complex objects.

In order to maximise the solid angle coverage using only few crystal shapes, an elegant possibility is to tile the spherical surface with the projection of the same simple pattern drawn on each of the faces of an enclosed regular polyhedron, namely one of the so-called “platonic” polyhedra. The maximum symmetry of the spherical tiling is obtained using the icosahedron, which, having 20 equilateral triangular faces, is the platonic solid with the largest number of faces. In the attempt to cover the sphere with

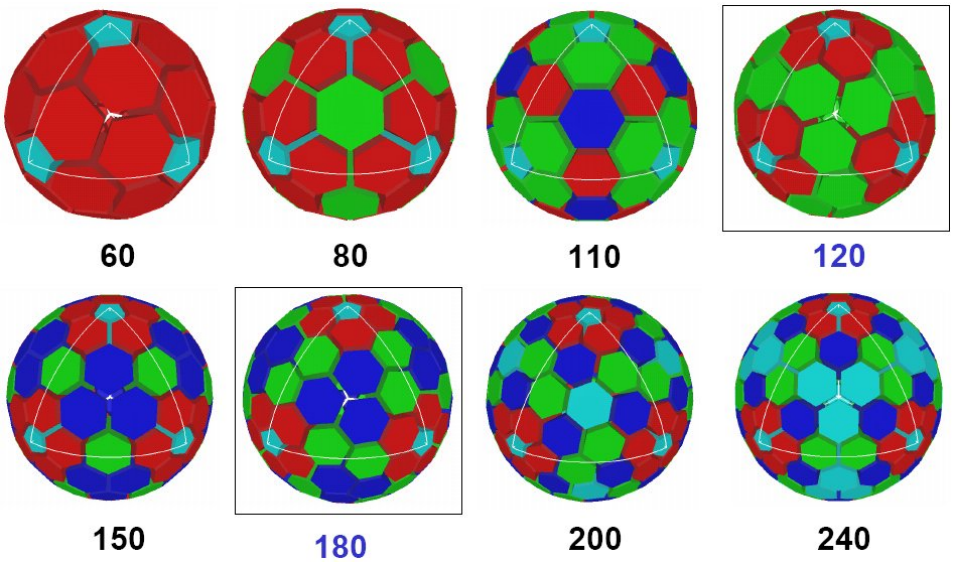

Figure 2.13: Geodesic tilings of the sphere obtained by decomposition of the regular icosahedron, labelled with the number of hexagons composing the array. For each configuration, the different colours correspond to a different crystal shape. The configurations investigated for AGATA, corresponding to $N_H = 120$ and $N_H = 180$, are highlighted with a square frame.

the best approximation of circular figures, the pattern on the faces of the icosahedron should have the shape of regular hexagons. Such tilings will always end up with $N_P = 12$ pentagons and with $N_H = 20 \cdot n$ hexagons, where $n = [i^2 + 3j^2 - 4]/8$, $i + j$ even, $2n$, i and j integers. Some of the resulting configurations are shown in figure 2.13.

Not all the possibilities are attractive for an array such as AGATA. Fixing the maximum size for the crystals, the configurations corresponding to small values of n result in a very small inner radius for the array, making it impossible to place inside any ancillary device. On the other hand, many of the configurations with larger n values, having a sufficient inner space, are not attractive because of the impossibility to group easily the detectors into triple or quadruple clusters. Here it should be noticed that the space for the cryostat is obtained from the cluster boundaries, resulting in irregular hexagons. Therefore, the shape of the detectors is obtained through the intersection of a cylinder with an irregular hexagonal prism. The resulting shape is similar to what is shown in in figure 2.14. On the other hand, the

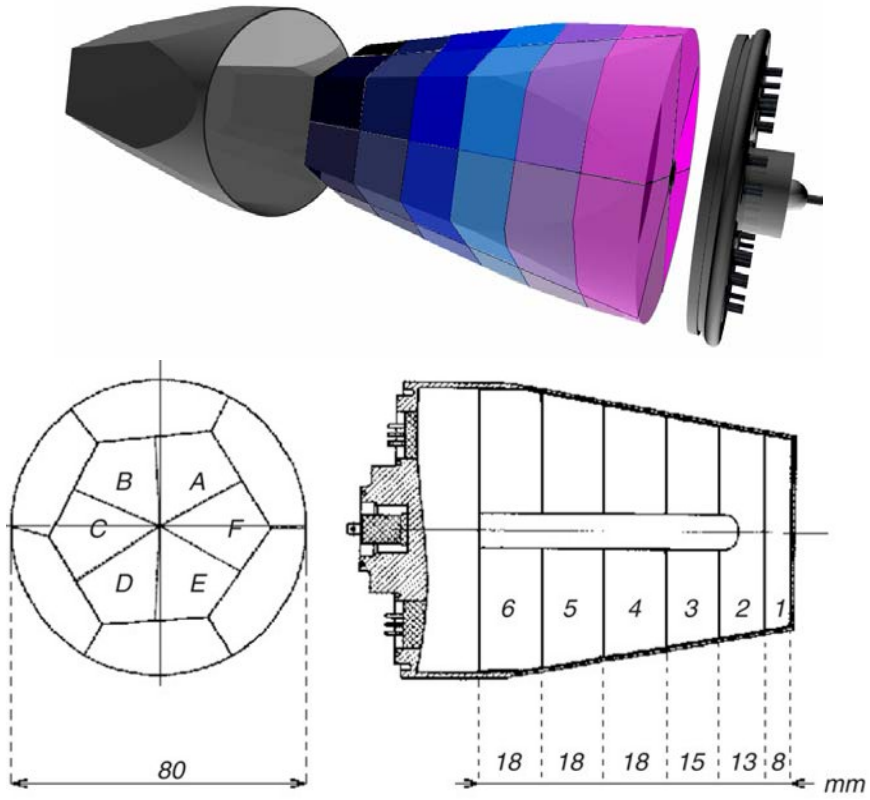

Figure 2.14: Geometrical configuration of a tapered asymmetric detector. The segmentation pattern is reported.

pentagons are always regular. Given the cost for their development and their contribution to the overall performance of the array, it was decided to minimise their volume and consider only arrangements of hexagonal (or *hexaconical*) crystals.

A specific code (called `marsview`) performing the solid angle decomposition into this kind of configurations was developed, providing as an output the elementary crystal shapes (namely, the coordinates of the vertexes), the transformations needed to build a cluster and the transformations needed to place the clusters into the array. The kind of transformations which have been considered are of the kind $T(x,\, y,\, z) \cdot R_z(\phi) \cdot R_y(\theta) \cdot R_z(\psi)$, where, e.g. $R_z(\psi)$ is a rotation of an angle ψ around the z axis and $T(x,\, y,\, z)$ is a rigid translation along the vector with Cartesian coordinates (x, y, z).

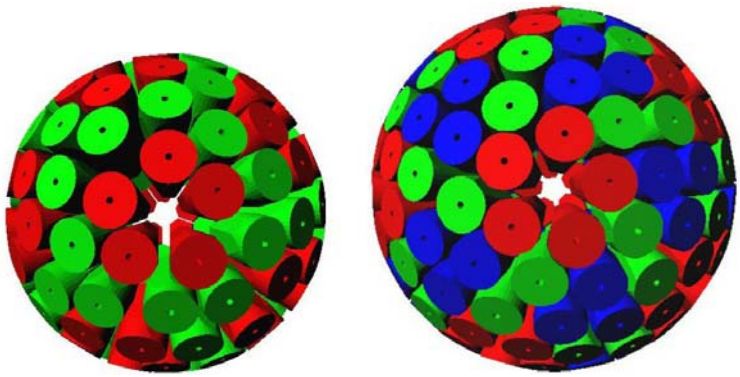

Figure 2.15: Possible geometrical configurations of the AGATA spectrometer. The array was designed to cover the maximum effective solid angle around the target using 120 or 180 detectors.

The configurations corresponding to $N_H = 120$ or $N_H = 180$ depicted in figure 2.15 have been soon identified as the most attractive for AGATA. In the case of $N_H = 180$, it is quite natural to form triple clusters out of three different crystal shapes as shown in figure 2.16; all of the clusters have the same composition. In the case of $N_H = 120$, the same solid angle as in the case of $N_H = 180$ can be covered using quadruple clusters (each containing two crystals for each shape), or using two types of triple clusters, corresponding to six different crystal shapes. In alternative, it is possible to form

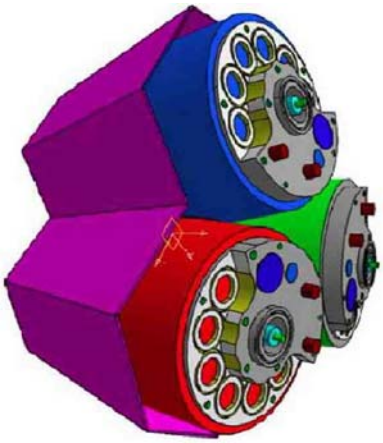

Figure 2.16: Three encapsulated crystals packed in the same cryostat.

	A120	A120F	A120C4	A180
Number of crystals	120	120	120	180
Number of crystal shapes	2	6	2	3
Number of cluster types	2	2	1	1
Covered solid angle (%)	70.97	77.79	78	78.36
Volume of Germanium (cm^3)	43590	42225	43160	70243
Mass of Germanium (kg)	232	225	230	374
Initial mass of Germanium (kg)	289	289	289	434
Fractional loss of Germanium (%)	19.7	22.1	20.4	13.8
Centre to Detector face distance (cm)	19.7	18	18.5	24.6

Table 2.1: Some of the relevant geometrical characteristics of the configurations.

two different cluster types out of two crystal shapes, with the disadvantage of a lower solid angle coverage.

The performance of the proposed configurations for AGATA (depicted in figure 2.15) was evaluated by means of a Monte Carlo simulation code based on the GEANT4 toolkit [68]. The code for AGATA [69] is suited to evaluate the performance of the array under a wide range of conditions, including "realistic" event generation, in-beam experiments and coupling to a range of ancillary devices. The actual construction of the geometry is performed by reading the files produced by `marsview` as explained above. The results of extensive comparisons [70] suggested that the configuration with 180 detectors has the best performance while still being economically feasible by the collaboration. Preliminary results for three different configurations with 120 detectors (labelled for brevity A120, A120F and A120C4) and the one with 180 detectors (A180) are reported in table 2.1 and in figure 2.17. It should be remarked that the key parameter in producing the photopeak efficiency is the solid angle coverage, which is similar for the A120F, A120C4 and A180 configurations; the better performance of the A180 arrangement is due to a larger target-detector distance, resulting in a better definition of the distance of photons and in a better performance of the tracking algorithm (in this case, the `mgt` algorithm). For all these reasons, the AGATA collaboration has decided to base the array on the A180 configuration. The GRETA collaboration has selected, mostly for econom-

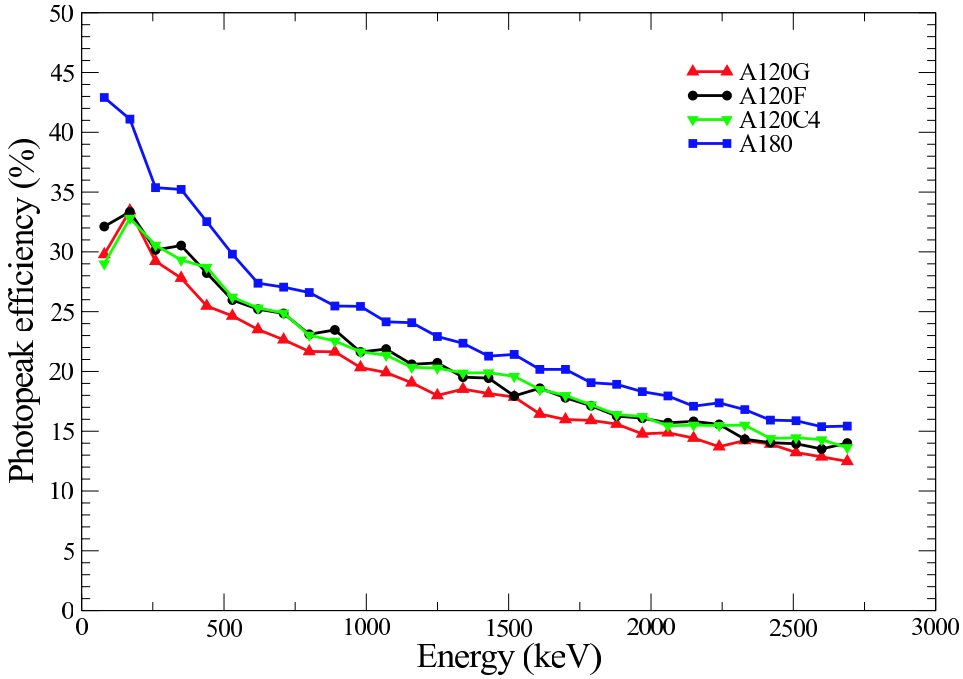

Figure 2.17: Photopeak efficiency for the proposed configurations for AGATA, calculated in the case of a point source at rest in the geometrical centre of the array emitting a rotational cascade of 30 photons in coincidence [69, 70].

ical reasons, the A120C4 configuration with the more complex 4-crystals cryostats.

The power of γ-ray tracking is apparent by the spectra shown in figure 2.18. These spectra refer to the same simulated data, considering a rotational cascade of 30 photons emitted by a recoiling nucleus with β=50%. The Doppler correction was performed respectively at a detector level, at a segment level or using the full information provided by the tracking algorithm. Only in the last case the peaks stand out of the background up to high energies.

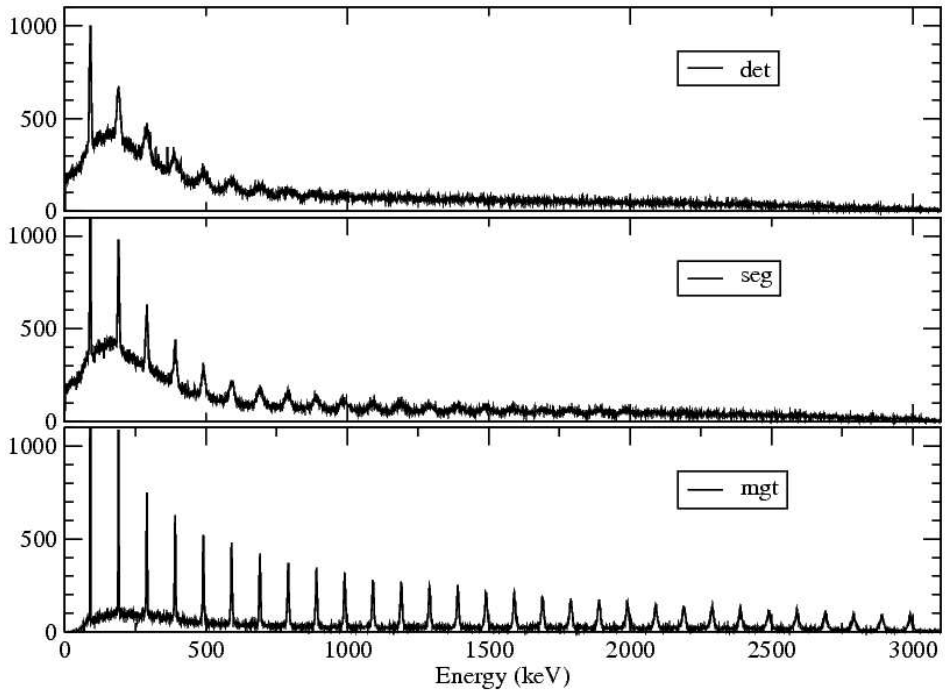

Figure 2.18: Simulated spectra obtained considering the emission of a rotational cascade of 30 photons from a source moving with velocity β = 50% along the z axis and performing the γ detection with the A180 configuration of AGATA. From top to bottom, the Doppler correction has been performed respectively at the detector, at the segment and at the interaction point level.

2.5 The AGATA detector

As discussed previously in section 2.4, the AGATA array will be based on a polyhedron composed of irregular hexagonal prisms. This results in so-called “hexaconical” detectors, having a tapered front face with hexagonal shape and a cylindrical backward part. This is a necessary compromise between the requirement to cover as large a fraction of the full solid angle as possible and the contrasting requirement to cut away as little a fraction as possible of the original cylindrical crystal. As mentioned previously, in order to be able to deal with such a big number of crystals, efforts were required to enhance the stability of performance and reliability of these detectors and to reduce to a minimum the maintenance time required. With this purpose, it was decided to rely on the encapsulation technology [71], devel-

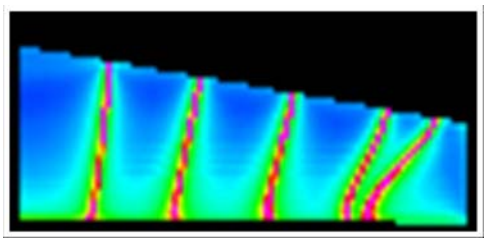

Figure 2.19: Effective segmentation of an AGATA detector. The colour scale represents in arbitrary units the position sensitivity of the AGATA prototype crystal [72]. The effective volume of the segments in the front part of the crystal is much larger than the value deduced from the segmentation scheme because of the distortion of the electric field.

oped within the framework of the EUROBALL collaboration. The AGATA crystals will be closed in an aluminium can 0.5 mm thick, with an internal distance between the Ge surface and the can of 0.5 mm, much smaller than the 5 mm distance in conventional Ge detectors. The capsule is hermetically sealed by electron welding of all feedthroughs and the lid. Thus, the detector vacuum is separated from the cryostat vacuum, and the capsules can be closely packed in a common cryostat. This has several advantages: the crystal remains sealed at all times, which avoids contamination of the Ge surfaces which can happen for example when annealing detectors; annealing is greatly simplified since one just needs to set the capsule in an ordinary oven; the cold FET is outside the capsule and can be easily repaired and also removed before annealing; a defective Ge detector in a cluster can be replaced with minimal effort.

In order to exploit pulse shape analysis techniques, the HPGe crystals should be segmented, as discussed previously. A 36-fold segmentation was chosen on the basis of extensive electric field calculations [41] as the reasonable compromise to identify the position of each interaction point with a precision of the order of a few millimetres, as needed by the tracking algorithms. The hexagonal shape of the crystals results naturally into a 6 sectors x 6 slices segmentation scheme. The size of the slices (along the crystal axis) was chosen trying to balance the “effective” volumes of the segments, which differs from the geometrical volume because of the distortion of the electric field in the front part of the detector as shown in figure 2.19.

Since the final geometry for AGATA was decided quite in a late stage

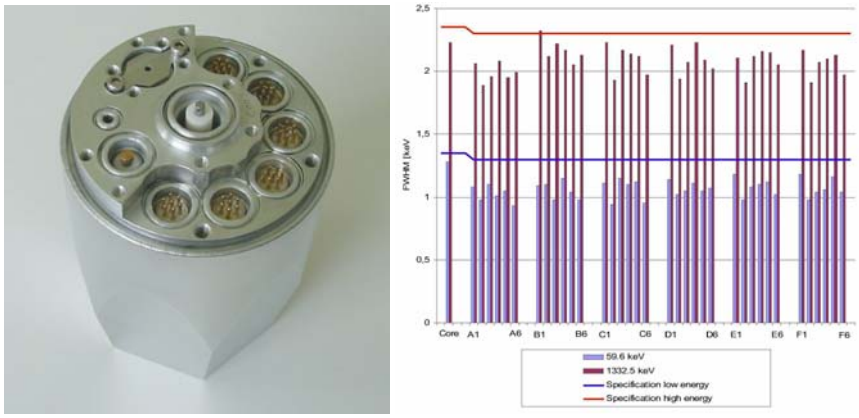

Figure 2.20: Photo of one of the prototype AGATA capsules and resolution values of its 37 channels for 60 and 1332 keV photons.

of the project, prototype detectors were bought from Canberra France in order to check the quality of such complex objects and to gain experience in handling them. Hence, the first three prototypes have a regular hexaconical shape. A picture of a prototype detector is shown in figure 2.20 together with the resolution values for all of the segments.

As discussed previously, the detectors of AGATA will be grouped into triple clusters in a common cryostat. Each cryostat will contain also the preamplifiers for 111 channels (36 segments + core for each crystal). A pic-

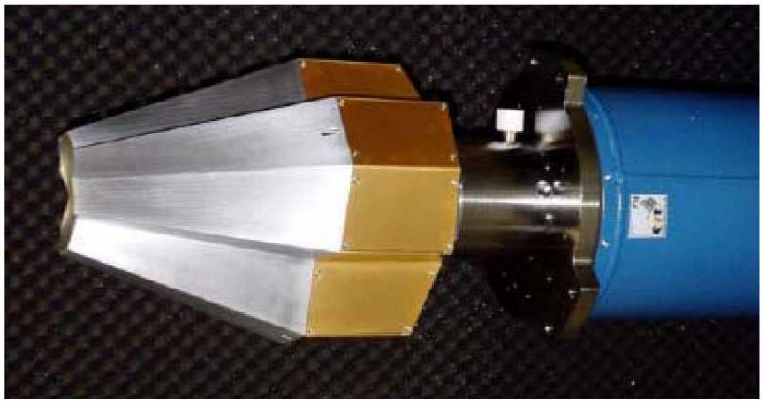

Figure 2.21: Photo of the prototype cryostat of the AGATA symmetric triple cluster.

ture of the prototype cryostat, built by the company CTT, is shown in figure 2.21. With its 111 high resolution channels (≈3 times more than GASP, ≈50% of the whole EUROBALL) this cryostat is an extremely complex object and its performance and reliability are critical for the success of the project. Its development has been carried out in close collaboration between the manufacturer and the AGATA-detector working group thanks to the know-how built at the Institute of Nuclear Physics of the Cologne University with the EUROBALL and MINIBALL projects.

2.6 The electronics for AGATA

As mentioned before, the detectors of AGATA will be operated in a "position-sensitive" mode, by digitising the signals from the preamplifiers and by using PSA algorithms to extract the information (energy and position) on the single interaction points. In order to keep the relevant position information, the signals should be digitised at a sampling frequency of at least 100 MHz, with a 14 bits ADC. Considering the expected number of crystals / segments for AGATA and a single rate of 50 kHz per crystal, this results in an extremely high data flux (6660 segments x 200 MB / s) which is too large to be stored and has therefore to be analysed in real time in order to extract the useful physical information. This is done as shown in figure 2.22, where the Data Acquisition System (DAQ) of AGATA is outlined in a schematic way.

All of the digitisers work synchronously by receiving their 100 MHz clock and a time stamp from a central clock generator (the *Global Trigger and Synchronisation*, GTS [73]). The continuous flux of samples from the digitisers is sent over optical fibres to the pre-processing digital electronics [73], which analyses each crystal as an independent entity in order to extract the useful information for each detected signal. To be able to perform the requested operation in real time, i.e. analyse a sample every 10 ns, the signal-processing algorithms are implemented into powerful highly-parallel FPGAs (Field Programmable Gate Array). The occurrence of signals in the crystals is detected by a digital trigger applied to the data stream of the anode (core). This *local trigger* forces the core and all 36 segments to generate an energy value (by means of the so-called Moving Window Deconvolution [74, 75]), and up to 128 samples ($\sim$1 μs) of the rise time of the pulse,

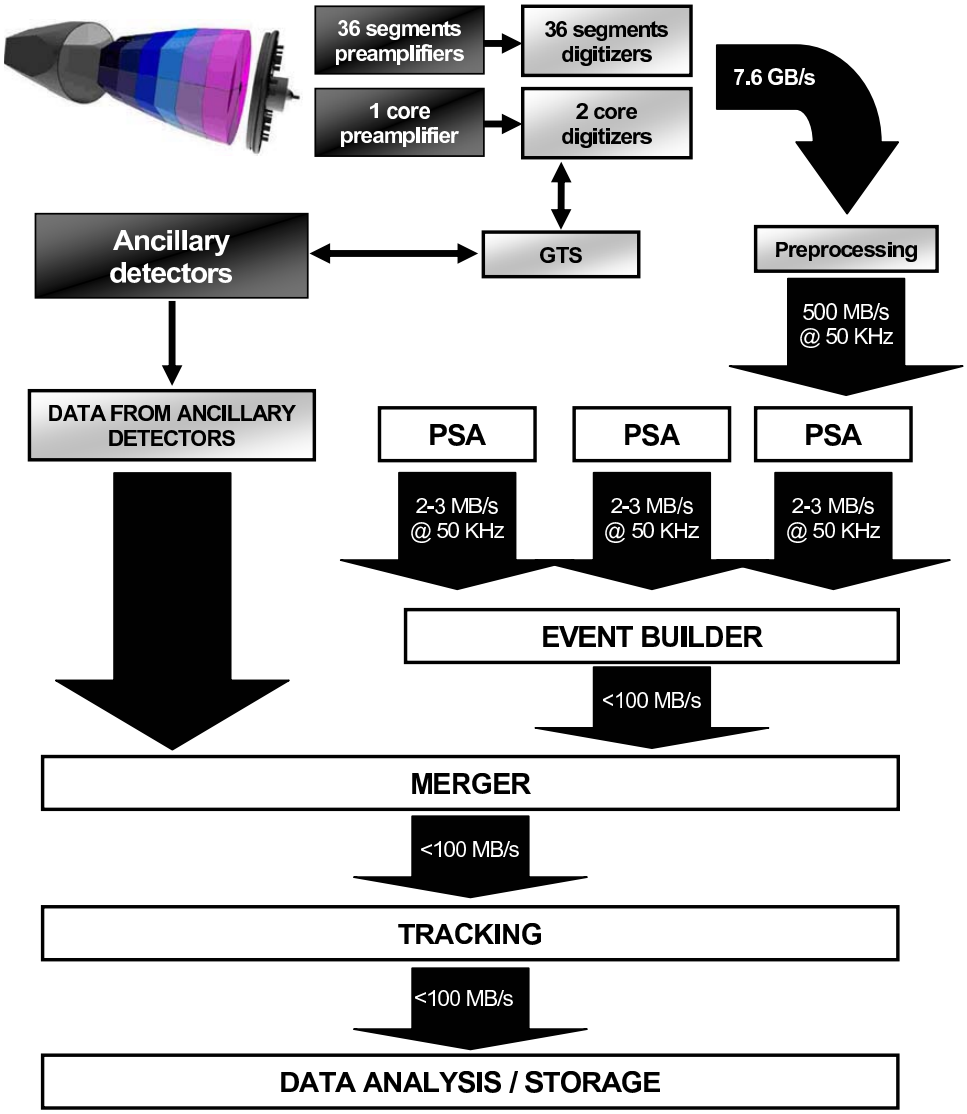

Figure 2.22: Schematic view the DAQ of AGATA.

discarding all the rest. Although in this way a data reduction of ∼95% is achieved, the throughput can still be as high as 500 MB/s/detector and it is almost mandatory to have a second-level trigger selecting the most useful events according to to user-defined, experiment-specific conditions. These conditions can be simply that a minimum number of germanium crystals fire simultaneously but can also (and usually do) request that other (ancillary) detectors participate in the event.

The time correlation among the detectors of AGATA is achieved by means of a time-stamping system where each clock pulse distributed by the GTS has an associated 48-bit clock counter which gives, in steps of 10 ns, the time elapsed since the beginning of the measurement run. Whenever the local triggers in the detectors fire, the clock number (time stamp) is recorded in a local memory buffer together with the energies and rise time slices of the 36 segments and the core. At the same time, the time stamp is sent back to the GTS system which uses it to generate a *global trigger* according to the specified conditions. The locally-recorded data is validated and passed over to the next processing stage only if the global trigger fires, otherwise it is discarded, thereby reducing the data throughput to whatever level is desired. To simplify the operation of the global event builder, the GTS generates an event number which is added as a tag to the validated data. Obviously the global level trigger can be defined in such a way that all local triggers are validated (e.g. in case of very low counting-rate experiments) achieving what in the AGATA specifications is called the *trigger-less mode*.

In the AGATA scheme, the ancillary detectors can use a similar digital electronics but can also use a classical VME-based analogue DAQ. In this case, the time correlation to the AGATA detectors is performed by a dedicated VME module, called AGAVA, which interfaces to the GTS system by reading its clock and time stamp and by sending local trigger requests and getting the corresponding validations.

After pre-processing, the validated local events are passed to the Pulse Shape Analysis stage. This is a farm of computers where the PSA algorithms are applied to extract the coordinates of the interaction points from the pulse rise-time samples. Once this is done, the traces can be discarded, thereby reducing the data throughput by an order of magnitude. This analysis is local to each of germanium crystal and the fastest PSA algorithms developed so far need a few milliseconds of a good level CPU to analyse an event. This is the bottleneck of the whole data-processing sequence and to achieve the 50 kHz singles rate of the AGATA specifications one should dedicate a farm of many ($\sim$100) computers to each crystal. For the initial phases of AGATA and until faster PSA algorithms will become available, the rate of accepted signals will be reduced by the global trigger to $\sim$1 kHz per detector, meaning that the PSA farm can be limited to a few CPU per crystal.

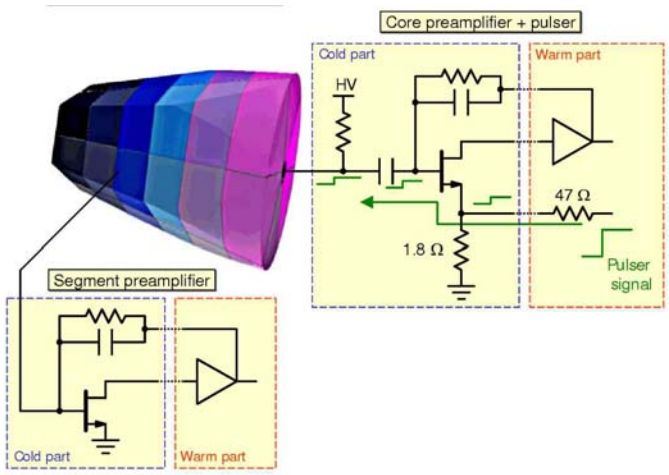

Figure 2.23: Schematic view of the preamplifiers designed for AGATA.

The PSA completes the data analysis at the detector level. After this, the global event has to be built collecting together, on the basis of the event number and / or time stamps, the information of all firing detectors. In the first implementation of the AGATA DAQ, this is done by first assembling the germanium detectors and then merging the data from the ancillaries. The global event contains all information (energies and positions of the interaction points of the firing germanium detectors) needed to perform the γ-ray tracking and any other experiment-specific on-line analysis. The events will of course be saved on permanent storage and will be made available to the experimental groups for the final off-line data analysis.

2.6.1 Preamplifiers

In the electronics of AGATA, the preamplifier is the only “electronic module” in a conventional sense. The preamplifiers for AGATA, developed in collaboration by INFN Milano, GANIL and IKP Cologne [76], play a vital role. Special care has been taken in keeping a sufficiently large bandwidth, so that the information on the position of the interaction, which is contained in the early part of the signal, is not lost.

Following the experience by using HPGe detectors in an environment having a background of very high energy ions, a fast-reset system was implemented. The problem observed in operating the RISING detectors at GSI

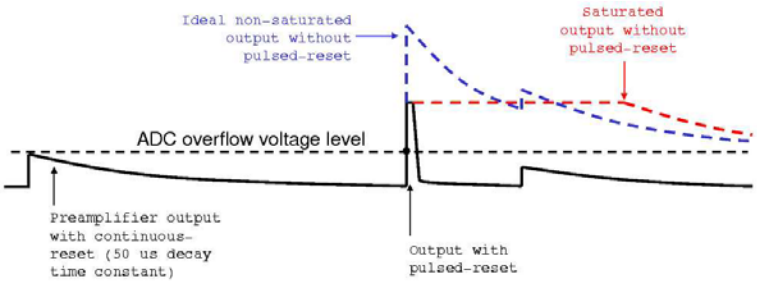

Figure 2.24: Schematic working principle of the “fast-reset” technique.

Darmstadt was that such energetic ions could interact directly with the germanium crystals, resulting in saturated signals which should be avoided since during saturation no useful information can be acquired. It was not considered appropriate to use a broader dynamic range for the preamplifier, which would limit the attainable resolution at lower energies. It was decided instead to apply a fast-reset technique (figure 2.24). The side effect of such technique is that the measurement of the time over threshold can be used to obtain an estimate of the amplitude of the saturated signal with good energy resolution [77].

The core preamplifier will include a built-in high-stability pulser, which will induce a signal on the segment preamplifiers as well through the capacitive coupling. The core preamplifier thus will provide a convenient signal to check the stability of all of the segment preamplifiers and digitisers. It should be remarked that a check of the stability of the segment preamplifiers with conventional techniques, that is using standard radioactive sources, will be not feasible in limited measurement times, and therefore the built-in pulser will be a reliable way to perform such checks.

2.7 The AGATA collaboration

So far 12 countries have joined the AGATA Collaboration: Bulgaria, Denmark, Finland, France, Germany, Hungary, Italy, Poland, Romania, Sweden, Turkey, UK. The present Memorandum of Understanding covers the period up to the end of 2008, by which time it is expected that a subset of five triple clusters (the AGATA Demonstrator Array) will be available in order to prove that the operation of a γ-ray tracking array, with on-line PSA

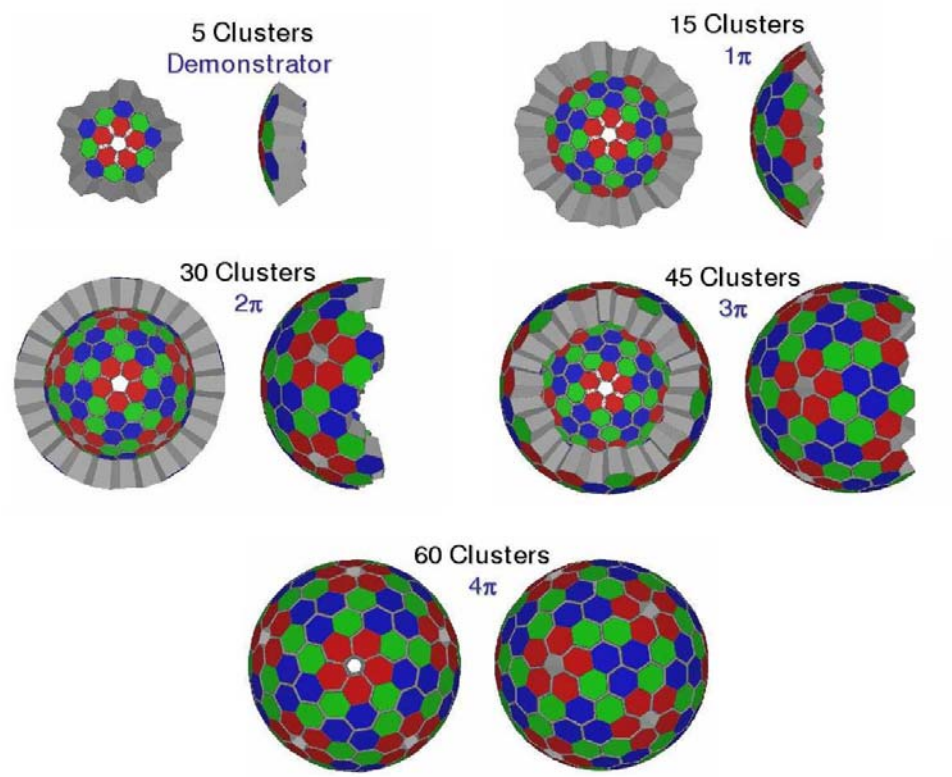

Figure 2.25: Evolution of the AGATA project from the demonstrator to the full 4π array.

and tracking, is actually feasible. The first installation site of the AGATA Demonstrator array will be the Laboratori Nazionali di Legnaro, where it will replace the CLARA [22] array in coupled operation with the PRISMA spectrometer. The collaboration is presently discussing a further MoU. It is foreseen that several campaigns will be run with partial subsets of the array as shown in figure 2.25, up to its final completion which could happen around 2018.

Chapter 3

In-beam experiment with the first AGATA triple cluster

In this chapter we will present the experimental results of the first in-beam test of the AGATA prototype triple cluster which were obtained during this work. It will be shown that with the application of PSA algorithms it is possible to improve the effective energy resolution of the detectors from 35 keV to 4.8 keV FWHM for the 1382 keV ground-state transition of ^{49}Ti. This result corresponds to a position resolution of approximately 5 mm, fully consistent with the specifications of the AGATA project. The procedures followed in the data analysis will be described in detail.

3.1 Motivation

As discussed thoroughly in section 2.2, the performance of a γ-ray tracking array like AGATA depends critically on the precision achieved in the measure of the individual photon interaction points. Therefore, once the prototype triple cluster of AGATA was available, it was soon decided to determine experimentally such value through an in-beam measurement which was performed in Summer 2005 at the Institute of Nuclear Physics (IKP) of Cologne, Germany. A very preliminary in-beam test with a cryostat mounting only a single crystal was actually performed previously by the Cologne group [78]. However, the experimental conditions were sub-optimal (no particle detector to define the kinematics) and the data were analysed following a simplified MINIBALL approach [79] which is hardly comparable with what reported in this thesis and will not be discussed further.

The main goal of this experiment was to compare the performance of different pulse shape analysis algorithms under realistic experimental conditions. At this stage of the project, the speed of the PSA algorithm was not considered as an essential parameter for the comparison, and therefore the available algorithms were benchmarked essentially on the basis of the attainable position resolution. However, in the final implementation of AGATA, the algorithms will have to be fast enough to perform an on-line processing, as remarked in section 2.6.

Incidentally, being the technology of encapsulated segmented HPGe detectors quite new, the in-beam test made it possible to gain experience in handling such complex devices under "realistic" experimental conditions. Inside the AGATA community, previous experience was present on the use of segmented HPGe detectors, namely with the 25-fold segmented MARS detector [47] and with the encapsulated 6- and 12-fold segmented MINIBALL detectors [48]. The new detectors of AGATA are however much more challenging from the technological point of view, given the high degree of segmentation combined with the process of encapsulation. It was therefore important to verify the behaviour of these detectors so that potential problems could be fixed in the subsequent production.

Another goal of this experiment was to check whether tracking of γ-rays is already feasible with just three germanium crystals. The practical result is that tracking is quite problematic in such a closely packed configuration and therefore such a point will not be discussed further in this thesis.

3.2 Measurement of the position resolution

In order to have a "direct" estimation of the position resolution which can be obtained with the AGATA detectors, a dataset of collected signals is needed, corresponding to events in which a photon interacted in a single point of known position. With such a dataset, the result of a PSA algorithm applied to the data can be compared event-by-event with the known position of the interaction.

In order to collect such datasets, the signals from the detector must be recorded under controlled conditions, so that the position of the interaction point can be determined. The techniques outlined in section 2.3 provide a basis of reference signals allowing to evaluate the position resolution of the

PSA algorithms. A major limitation of such methods is that the position of the interaction is defined with a precision of the order of the size of the collimator. In order to collect enough statistics in reasonably short times, the holes of the collimator cannot be too narrow and as a consequence a PSA algorithm will give a distribution of points for each position of the collimator, the dispersion depending both on the PSA resolution and on the hole dimension. With the collimators used presently, the distribution will depend practically only on the collimation precision. Another limitation of this method is that only single interaction points are sampled, which is not the typical case in γ-spectroscopy experiments, being multiple Compton scattering a highly probable process for γ-rays interacting with a germanium crystal in the energy range 500-1500 keV.

A possible solution is the one of an indirect measurement, as done in the past for the MARS [80, 81] and GRETA [82] detectors. The basic idea is that, when the γ-rays are emitted in-flight by a recoiling nucleus, the width of peaks in the Doppler-corrected spectra will depend on three factors, namely the intrinsic detector energy resolution, the error on the velocity vector of the emitting nucleus and the uncertainty on the photon direction. The last factor depends on the position resolution of the PSA algorithm used. If the other causes of Doppler broadening are known, the position resolution of the detector can be inferred from the observed energy resolution. This is not an easy task because all the direct and indirect sources of Doppler broadening have to be tracked down and, when not negligible, accurately quantified. Contrary to the scanning table events which are selected to correspond to a single photon interaction, in an in-beam measurement the conditions are the same as in the future use of the AGATA detectors.

The broadening of the peaks in this work has been predicted using a Monte Carlo simulation but, as a first approximation, it can also be calculated using the propagation of errors and some schematic assumptions. The importance of this approach is to make the results intuitive. The Doppler-shift formula is the following:

$$E_{\gamma}^{cm} = E_{\gamma}\frac{1-\beta\cos\theta}{\sqrt{1-\beta^2}} \tag{3.1}$$

where E_{γ}^{cm} is the intrinsic energy of the γ-ray, E_{γ} is the energy of the photon in the laboratory (in other words the energy seen by the detector), β is the velocity of the emitting nucleus in fractions of c and θ is the angle be-

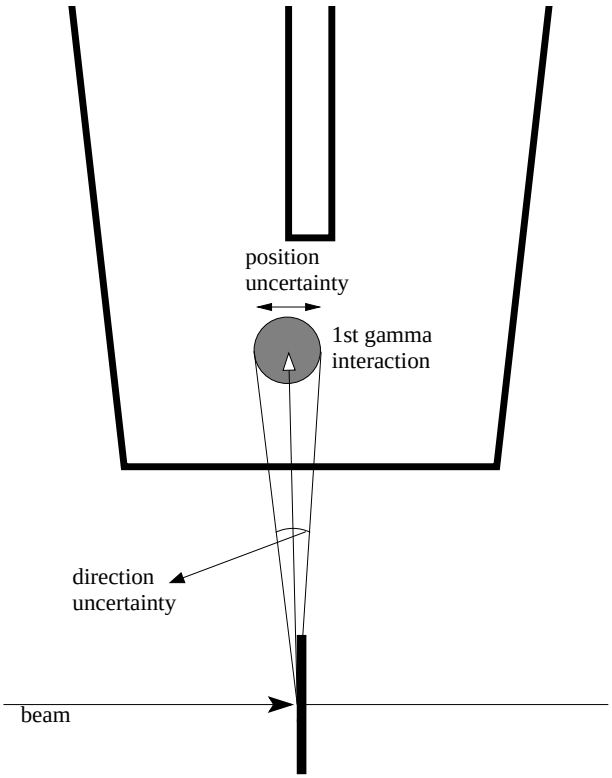

Figure 3.1: The finite position resolution attained from the AGATA detector is reflected in an uncertainty in the angle between the direction of the photon and the direction of the emitting recoil, resulting in a broadened peak in the Doppler-corrected spectra.

tween the direction of the recoil and the direction of the photon again in the laboratory.

Each of the parameters entering the formula contributes to the final uncertainty. For instance, the θ angle is determined experimentally from the position of the first interaction of the photon and the target position. Thus, an error in the position is translated to an error in the direction of the γ-ray, giving an imperfect Doppler correction as schematised in figure 3.1. Quantitatively, the contribution of each parameter to the final position resolution

is evaluated through the propagation of errors on E_γ^{cm}, giving:

$$\begin{aligned}\left(\Delta E_\gamma^{cm}\right)^2 &= \left(\frac{\partial E_\gamma^{cm}}{\partial \theta}\right)^2 (\Delta\theta)^2 + \\ &+ \left(\frac{\partial E_\gamma^{cm}}{\partial \beta}\right)^2 (\Delta\beta)^2 + \\ &+ \left(\frac{\partial E_\gamma^{cm}}{\partial E_\gamma}\right)^2 (\Delta E_\gamma)^2 \end{aligned} \tag{3.2}$$

In this calculation, the different broadening sources are considered as statistically independent contributions, neglecting for simplicity any correlation between them. In equation 3.2, $\Delta\beta$ and $\Delta\theta$ are respectively the uncertainty on the velocity module and on the direction of the nucleus emitting the radiation. Even if the recoil velocity vector can be measured on an event-by-event basis, $\Delta\beta$ and $\Delta\theta$ will be generally non-zero given the finite resolution of the detectors. The term ΔE_γ in equation 3.2 describes the contribution of the intrinsic energy resolution of the detector.

The partial derivatives are:

$$\begin{aligned}\frac{\partial E_\gamma^{cm}}{\partial \theta} &= E_\gamma \frac{\beta \sin\theta}{\sqrt{1-\beta^2}} \\ \frac{\partial E_\gamma^{cm}}{\partial \beta} &= E_\gamma \frac{\beta - \cos\theta}{(1-\beta^2)^{3/2}} \\ \frac{\partial E_\gamma^{cm}}{\partial E_\gamma} &= \frac{1-\beta\cos\theta}{\sqrt{1-\beta^2}} \end{aligned} \tag{3.3}$$

The angular error is propagated to the error in the determination of the intrinsic energy of the γ-ray by the coefficient given in the first of equations 3.3. As an example, the contributions of the three sources of Doppler broadening are sketched in figure 3.2, for the case of photons of 1 MeV emitted from a nucleus in motion with $\beta = 20.0\%$ and detected with an uncertainty $\Delta\theta = 1^\circ$ on its direction.

Besides the finite resolution on the position of the interaction, in an indirect measurement the other relevant sources of error in the determination of the intrinsic energy of the photon are the energy resolution of the detector and the uncertainty on the velocity vector of the emitting recoil. To simplify the experimental setup, it is possible to measure indirectly the velocity vector of the emitting nucleus through a kinematic calculation based on the measurement of the velocity vector of the other reaction products. This

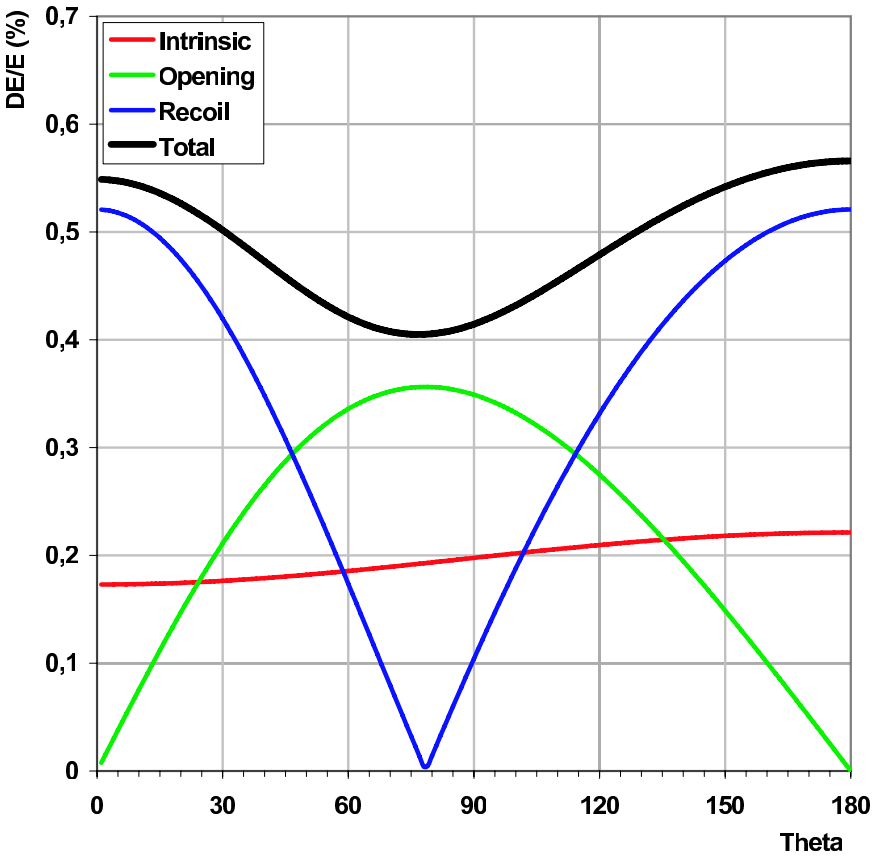

Figure 3.2: The contributions of the different Doppler broadening sources as a function of the azimuthal angle of the detector with respect to the direction of the recoil emitting the radiation. A photon energy of 1 MeV is assumed, with a typical energy resolution for a germanium detector, producing the "Intrinsic" contribution (in red); a source velocity of $\beta = 20.0\%$ with an error of 0.5%, giving the "Recoil" contribution (in blue); an uncertainty $\Delta\theta = 1^\circ$ in the source direction, obtaining the "Opening" contribution (in green).

is actually the case for the experiment we performed. As a consequence, some other contributions have to be considered to explain the experimental broadening, namely:

- straggling of the beam inside the target;
- angular and energy dispersion of beam due to the accelerator and the transport;

- straggling of the other products of the reaction inside the target and absorbers.

All of these broadening sources have been quantified through a Monte Carlo simulation using SRIM [83] as it will be discussed in more detail in section 3.6.

3.3 The experiment: choice of the reaction and setup

3.3.1 Optimisation of the experimental conditions

In planning an experiment aiming to estimate the position resolution of the AGATA detector, one has to maximise the contribution to the error on the intrinsic energy coming from the position uncertainty of the first photon interaction, thus maximising the first term in the sum of equation 3.2. From the physical point of view this means:

- to maximise the velocity module of the emitting nucleus. In this respect, the possibility to use an inverse kinematic reaction is a clear advantage;
- to place the detector at an angle of 90° with respect to the beam axis in order to have an angle between the recoil and the photon close to $\theta = 90^\circ$;
- to place the detector as close as possible to the target. In fact a given position uncertainty translates into an angular uncertainty which is inversely proportional to the distance between the target and the interaction point.

It should be remarked that, in order to have the best estimate on the position resolution, all of the contributions to the intrinsic photon energy uncertainty which cannot be precisely estimated should be minimised. Once the decision was taken to perform an in-beam test with the prototype AGATA triple cluster, it was soon decided to run the test at the IKP of Cologne where the detector was assembled and where it was being tested. In fact, it was considered too risky to transport it to other laboratories, being the detector not fully debugged at the time. In Cologne it would have been possible to rely on the constant support of the local group, which at the time was the most experienced group within the collaboration in handling these new

detectors. Unfortunately, the available beams at the FN-Tandem accelerator of IKP Cologne are limited to mid-mass nuclei, somewhat limiting the possible reactions of interest.

After evaluating the possibilities given by the available beams, it was decided to perform a ^{47}Ti + d reaction at 85 MeV beam energy, using a deuterated titanium target. Since the beam energy was far below the Coulomb barrier for a ^{48}Ti target nucleus (which in the laboratory reference frame is of the order of 125 MeV), no contaminant ^{47}Ti+^{48}Ti reaction was expected. In this way it was possible to avoid the use of a gaseous target, which would have implied major technical challenges.

The choice of performing the experiment at 85 MeV beam energy was actually motivated with the attempt to enhance the cross section for direct reaction mechanisms with respect to the cross section for fusion-evaporation reaction, dominating at higher beam energies. This would somewhat simplify the required experimental setup, as discussed below. The Q-value for the planned reaction ^{47}Ti(d,p)^{48}Ti is 9.4 MeV.

As discussed in section 3.2, for this experiment the full information on the recoiling nuclei was needed for an accurate Doppler correction. The velocity vector of the emitting nucleus was measured indirectly on an event-by-event basis by using a segmented silicon detector to detect the light charged particles emitted in coincidence with the γ-rays. This implies that the only useful events for this experiment are those in which a photon was detected by the AGATA detectors and a charged particle interacts with the silicon detector, allowing for a selection of the reaction channel as well. In the case of direct reactions, the velocity vector of the reaction partner can be extracted from the information on the position of the firing segment, by exploiting the two-body kinematics. Thus, there was no requirement to fully stop the particles inside the silicon detector, which would be needed in case the full particle energy had to be measured; the light charged particles were detected with a compact-disc shaped, 300 μm thick double-sided silicon strip detector (in the following DSSSD) segmented in 64 radial sectors on one side and 32 annular rings on the other side, placed at 35 mm from the target position. With this detector, the uncertainty on the reconstructed direction of the recoiling ^{47}Ti nucleus ranges from 0.01° to 0.06° depending on which ring of the silicon detector is hit. Such value is negligible with respect to the uncertainty of the photon direction. A 16 μm thick aluminium absorber was placed in front of the silicon detector to avoid the elastically

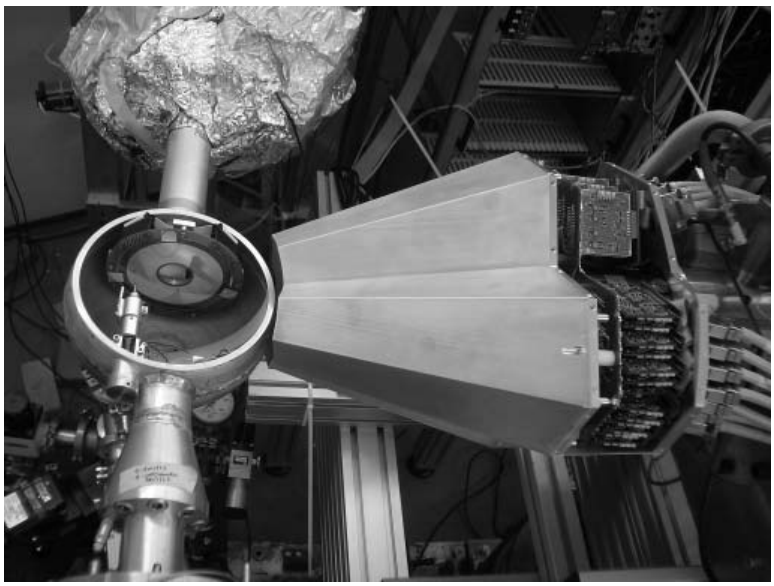

Figure 3.3: Photo of the experimental setup: the AGATA prototype triple cluster placed at 90° with respect to the beam axis and the DSSSD inside the open chamber.

scattered titanium nuclei to reach the silicon detector.

In order to maximise the Doppler broadening, the minimum chamber size to fit the silicon detector was used in the experiment and the AGATA triple cluster was placed at a nominal distance of ∼10 cm from the target, i.e. as close as possible to the chamber, at 90° with respect to the beam axis. A photo of the setup is shown in figure 3.3.

The γ spectrum recorded by the AGATA cluster in coincidence with the DSSSD is shown in figure 3.4, where no Doppler correction was performed. A broad 984 keV peak corresponding to the $2^+ \rightarrow 0^+$ transition of ^{48}Ti is clearly visible, but there is also an unexpected strong 1382 keV peak which corresponds to the ground-state transition in ^{49}Ti. Actually it turned out that it was not possible with the accelerator magnet to separate in the beam ^{47}Ti from ^{48}Ti, which has a natural abundance roughly ten times larger. Therefore, it was decided to increase the beam energy and run instead the much stronger fusion-evaporation reaction d(^{48}Ti,^{49}Ti)p at 100 MeV beam energy. The problem with this reaction mechanism is that, since the centre-of-mass spectrum of the evaporated protons has a broad distribution, the direction of the proton is not sufficient to deduce the direction and the ve-

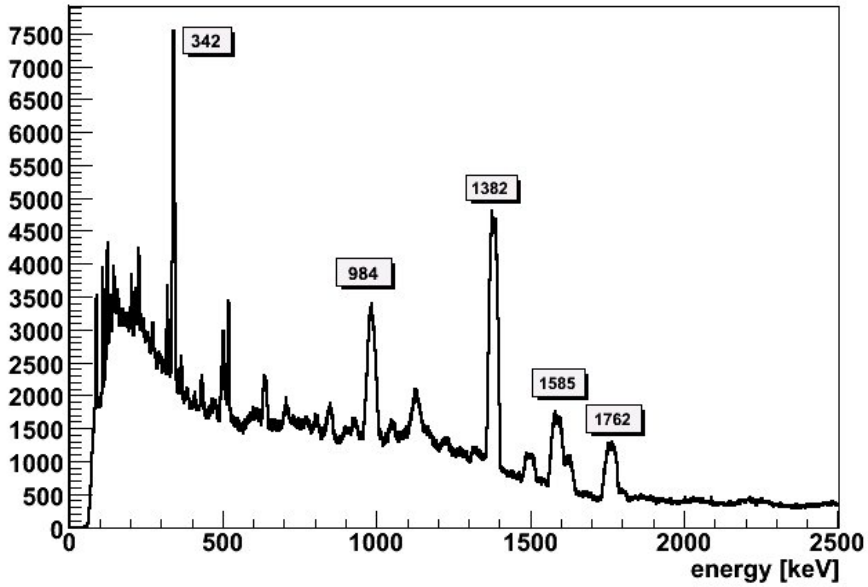

Figure 3.4: Raw γ-ray spectrum recorded by the AGATA triple cluster in coincidence with the DSSSD. Some peaks are labelled with their energies.

locity of the ^{49}Ti recoil on an event-by-event basis and a measurement of the full proton energy is needed. Unfortunately, as mentioned above, the DSSSD in use was 300 μm thick, not enough to provide such information. This problem was taken into account by performing the simulations consistently with the experimental situation, i.e. ignoring the information on the proton energy. This procedure increases the uncertainty on the estimate of the position resolution.

3.3.2 Electronics, DAQ and trigger

The layout of the electronics and data acquisition system, based on the Multi Branch System developed at GSI [84], is shown in figure 3.5. The signals from the core contacts of the AGATA crystals were split in order to generate the trigger information through conventional constant-fraction discriminators and at the same time be digitised. No signal splitting was necessary for the segment signals as they do not participate in the trigger. Both the core and the segment signals were digitised using XIA-DGF

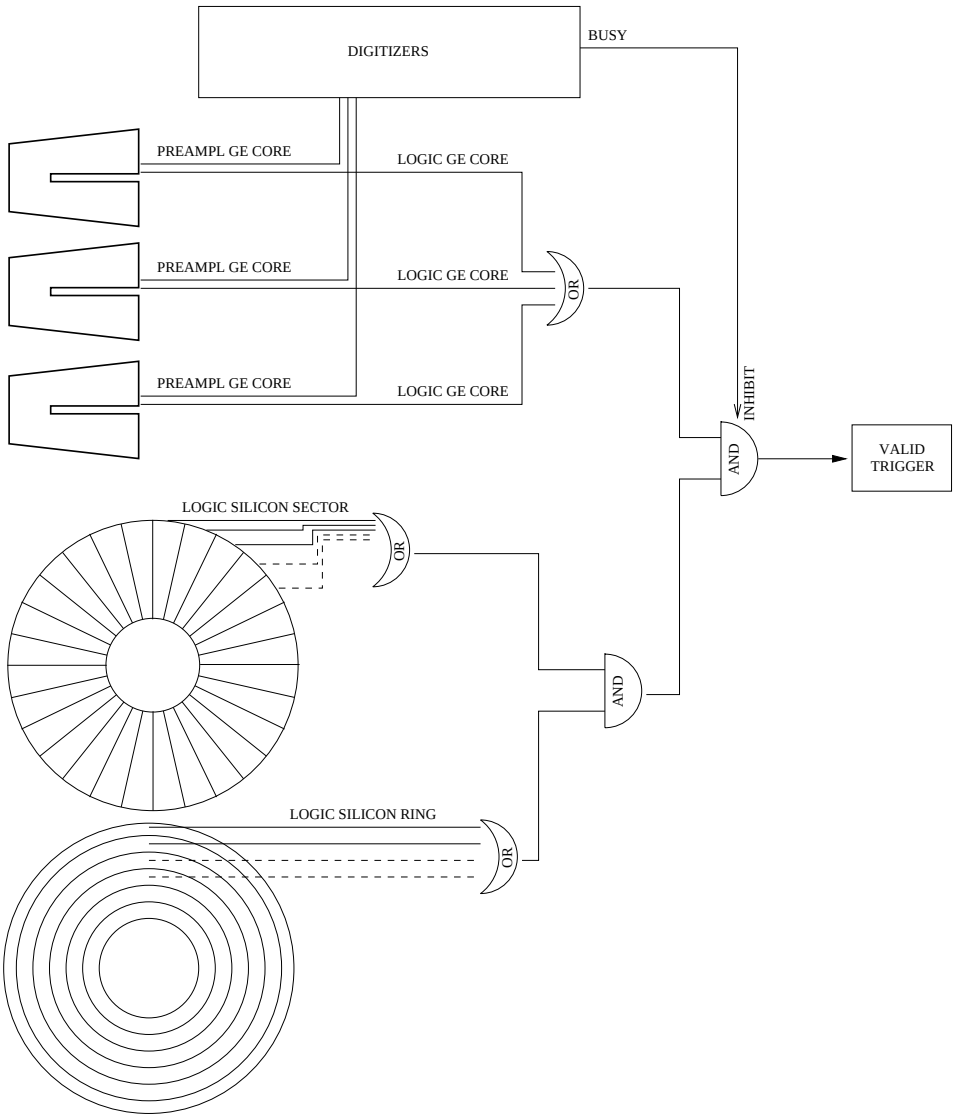

Figure 3.5: Layout of the electronics and of the trigger used in the experiment.

cards [85] with 14-bit FADCs and 40 MHz sampling frequency. The FPGAs mounted in these cards performed a digital trapezoidal shaping of the acquired signals to retrieve the information on the amplitude of the signal, which is proportional to the energy deposited inside each segment (figure 3.6; see [86]). With this configuration, the output for each channel of the DGF card consisted of 80 samples of digitised signal (i.e. a time slice of

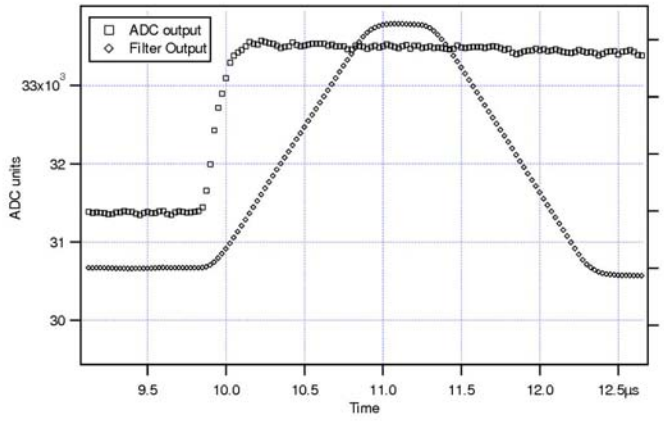

Figure 3.6: Trapezoidal shaping of the waves internal to the DGF cards.

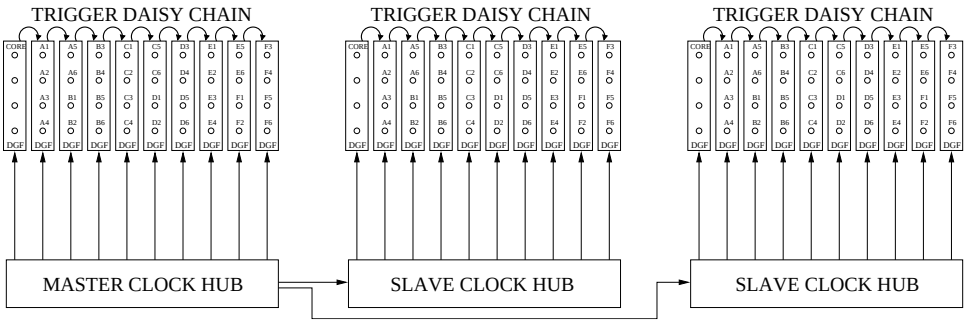

Figure 3.7: Layout of the trigger and clock distribution between the DGF modules. See text for details.

$2\,\mu$s), the value of the amplitude of the digitised signal and a timestamp. When a valid trigger was received by the digitisers, the signals from the core preamplifier and from all the segments of the detector were read-out and recorded. The synchronisation of the cards was performed by distributing a common clock through a star connection. This, together with the common trigger distributed by a daisy chain (as shown in figure 3.7), was expected to guarantee a constant time difference between the signals digitised from different segments.

The signals coming from each of the 96 channels of the silicon detector were sent to a shaping and timing filter amplifier (STM 16 manufactured by

Mesytec) and then digitally converted and readout by a VME Peak Sensing ADC (V785 manufactured by Caen) and a VME TDC (V775 manufactured by Caen). Since the scattered beam was stopped inside the absorber foil, the expected particle multiplicity was one particle per event, and therefore by combining the information from the rings and from the sectors it was possible to know without ambiguity the radial and azimuthal position of the interaction.

The trigger conditions required the coincidence between one of the three AGATA detectors AND one segment AND one ring of the silicon detector. In order to accept the events only when the digitisers were ready to process the signals, the ”busy” signal from the digitisers has been used as a veto.

Since the data transfer of the DAQ was slow and the size of the event was of the order of 6 - 18 kByte (depending on the number of AGATA detectors firing), the trigger rate was dominated by the readout dead time, i.e. for most of the time the trigger was vetoed by the busy signal of the digitisers.

3.3.3 Naming conventions and reference frames

To identify uniquely each segment within the detector, the reference frame and numbering depicted in figure 3.8 has been adopted. For each crystal, letters (from A to F) are used to label a sector, numbers (from 1 to 6) to identify a slice. The reference frame of each crystal is right-handed, having the z-axis positioned along the crystal axis and pointing from the front face to the back side, that is towards increasing slice numbers. The front face has z = 0; the x axis points to the centre of sector A; sectors increase counter-

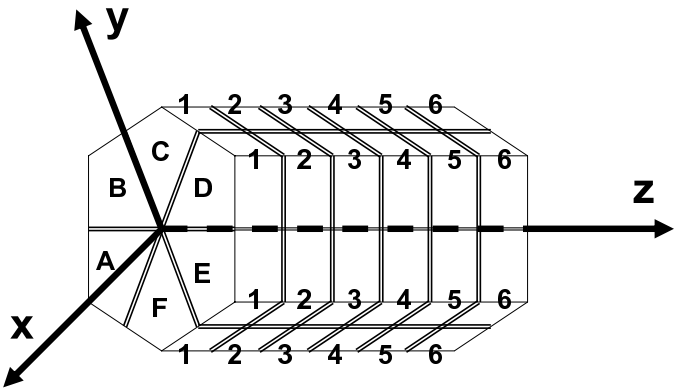

Figure 3.8: Labelling and reference frame for a single detector.

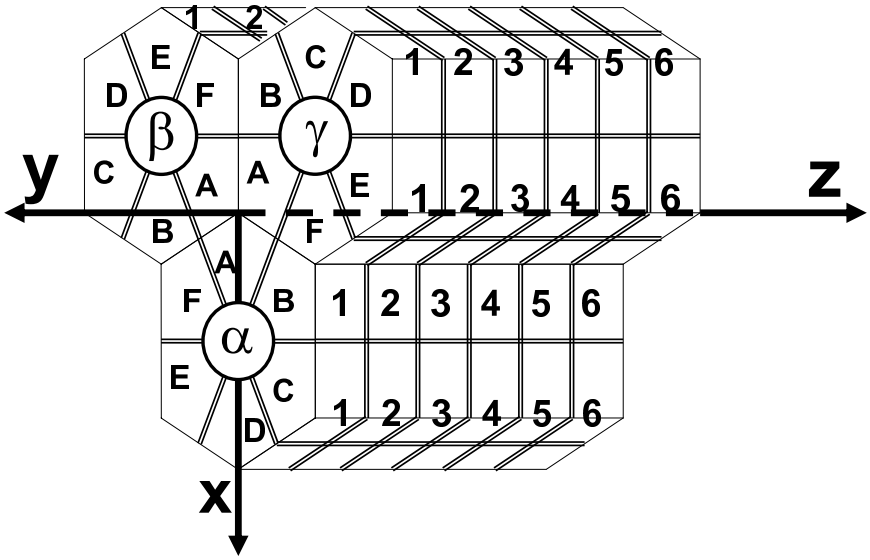

Figure 3.9: Labelling and reference frame for a cluster detector.

clockwise in the crystal reference frame.

The three crystals composing a cluster are identified by Greek letters (α, β and γ). As schematised in figure 3.9, the crystals are oriented so that the "A" sectors share a side (and a vertex); such side coincides with the z axis in the cluster reference frame, while such vertex has z = 0. The z axis of the cluster is oriented towards the back side of the crystals; the x axis of the cluster points to the α crystal axis; crystal names increase counter-clockwise in the cluster reference frame.

3.4 Presort

In order to be able to perform the pulse shape analysis of the collected data a particular treatment has to be done on the recorded digitised signals. The event belonging to the channels of interest have to be selected. The fact that this experiment was performed coupling a thin DSSSD to the AGATA prototype triple cluster generated some difficulties in understanding the reaction channels and the mechanisms involved.

In this section, the preliminary treatment of the experimental data will be described in detail.

3.4.1 Quality and integrity of the data

Germanium detector: calibrations

Before and after the measurement, the germanium detectors were energy calibrated using a standard ^{60}Co source. This operation is particularly critical with these detectors. In fact, differently from the standard non-segmented detectors, extremely long measurement times are required to gather enough peak statistics for the segments positioned in the back part of the crystal. Moreover, high statistics is needed to evaluate the crosstalk correction as first explained by Venturelli et al. [87]. This effect is expected to affect the resolution of the detector as a consequence of a variation of the gain depending on the pattern of firing segments. The signal amplitude of a segment has to be corrected according to a linear combination of the signal amplitudes of the other segments. This effect is known to be due to capacitive coupling between the high-impedance input and the low-impedance output of the FETs of two different preamplifiers [88]. Bruyneel in his PhD thesis [89] proposed an interpretation of this phenomenon based on an AC equivalent scheme of the detector which is shown in figure 3.10.

Predictions based on this model can be made for the coupling of the electrodes and their electronics. The core is AC coupled to its preamplifier using a large capacitance. Being less effectively coupled to ground than the segments, the core contributes more to the crosstalk. Experimentally, two kinds of crosstalk have been observed, namely a crosstalk which is proportional to the net-charge signal and one which is proportional to its derivative. Measurements of both kinds of crosstalk are reported in [89] and it is shown that a proper combination of them can account for the observed deviation of the shape of the signals from the expectations from the Shockley-Ramo theorem. The comparison of the predictions of this model with the experimental results is presently under evaluation. Bruyneel showed that this model accounts for most of the crosstalk but that probably it has to be refined to formulate a correction to the experimental data with such a good quality that the resolution of the detectors is not affected even at high energy. Presently studies on this subject are being carried out in Cologne [90] and Padova [91].

Using the data of the calibration runs, it is possible to estimate the effect of proportional crosstalk for the coupling of the core with a particular segment, by constructing a dataset with the request that only one segment

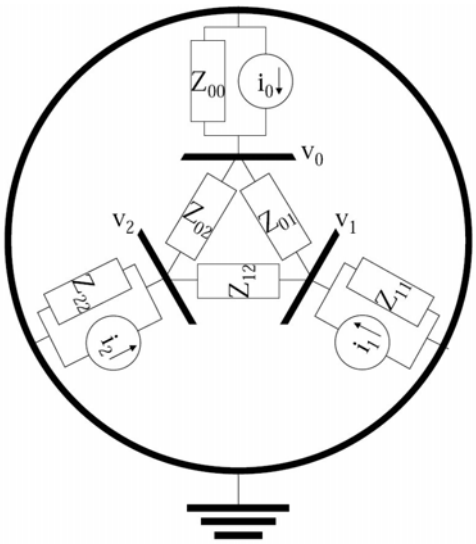

Figure 3.10: Detector equivalent AC scheme. Only 2 segments are drawn (labelled 1 and 2); the core central contact is labelled 0. The couplings between the different contacts and between them and the ground are shown.

is firing (i.e. at segment multiplicity 1) and, for each detector, by incrementing 36 spectra of the core contact, each spectrum corresponding to the coincidence with a particular segment. In this way, the proper recalibration coefficients have been estimated. Due to the lack of statistics in the calibration data it was not possible to determine the recalibration coefficients to correct the crosstalk for higher multiplicities. As a first approximation the coefficients found at multiplicity 1 have been applied also at higher segment multiplicities. Although the results are not perfect, the approximation seems to be reasonable since the crosstalk is expected to be more effective from the core to a segment, while the cross talk from a segment to the core is of the order of 0.05%–0.2%. Since we are missing part of the cross-talk coefficients, during the subsequent analysis the energy measured by the core contact will always be used.

The energy measured by the core central contact as a function of the firing segment is shown in figure 3.11. The 6-segment period shows that the segment-central-contact crosstalk is similar for segments belonging to the same slice, or, in other words, having similar extension along the crystal axis.

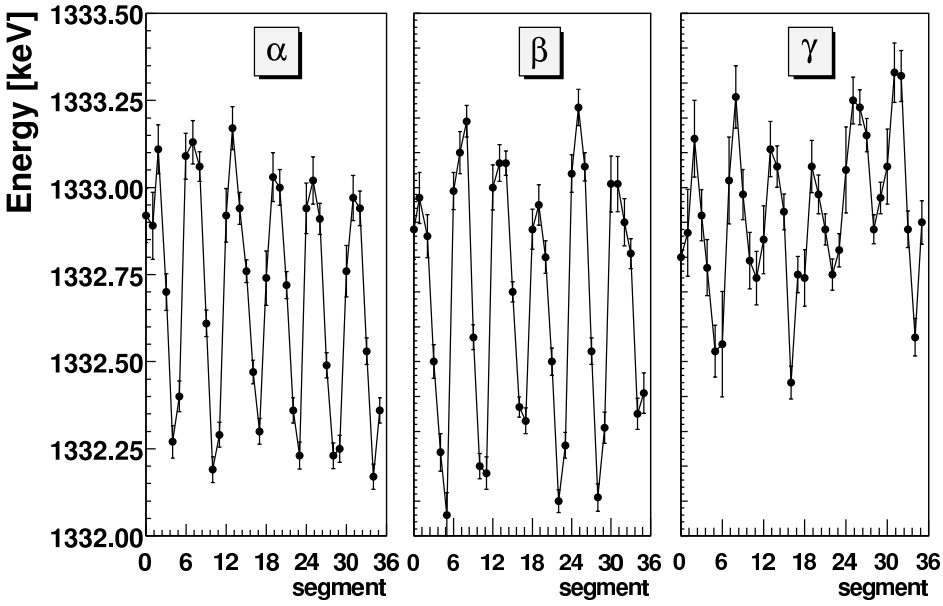

Figure 3.11: Energy measured by the core central contact as a function of the segment that is firing.

Germanium detector: gain stability

Since the electronics was not temperature-stabilised, variations of the gain with time were expected. This effect can be corrected for by looking, in the experimental data, at the position of narrow peaks of known energy emitted from nuclei at rest (for instance, photons coming from the activation of the beam dump or similar sources of background radiation). The only convenient line with such characteristics found in our dataset was the 511 keV annihilation line, since the statistics for the other peaks was poor.

In figure 3.12 the electronic gain drift for one of the AGATA detectors is evident. What is drifting is the energy calculated internally by the DGF module connected to the core preamplifier of the α-detector. Alignment coefficients are calculated from the fit of the position of the peak in these spectra. The statistics for the 511 keV peak in the spectra of the individual segments is not good enough to perform the same correction. In any case, as discussed previously, since part of the cross-talk coefficients is missing, during the subsequent analysis the energy measured by the core contact

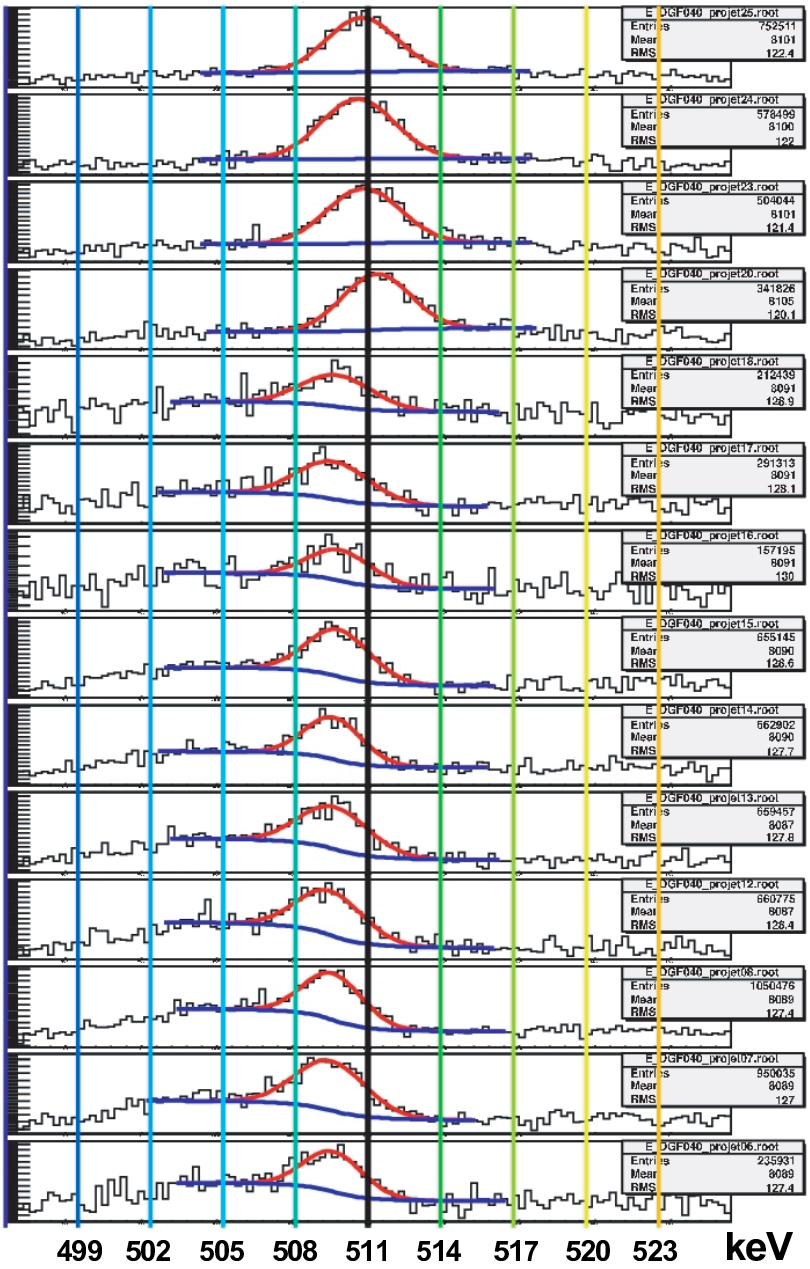

Figure 3.12: Gain drift of the core energy of the α detector. The fitted peak correspond to 511 keV and the vertical lines are spaced by 3 keV. Different spectra correspond to different acquired tapes.

will always be used. Therefore, the (possible) instability of the electronics processing the segment signals will not affect our results. As mentioned in section 2.6.1, in the future a high-stability pulser will inject periodically a signal into the core preamplifier, which will also induce signals in the segments. With this method, there will be a constant reference to correct for the drifts of the electronics.

Germanium detector: synchronisation of DGF cards

The synchronisation of the digitisers is a relevant aspect of this kind of measurements. The digitised signals have to be processed with a pulse shape analysis algorithm, consisting in a comparison between the experimental data and the calculated signals stored in a database. A systematic delay of the signal from a particular segment will cause a mistake in the identification of the correspondence between the recorded and the basis signal. An even more complicated situation would arise if the the delay of one channel with respect to another is changing event-by-event.

The trigger was sent via a daisy chain to each digitiser card and, as we will see, it turns out that the different distribution methods generated some inconsistency on the data. The use of a common clock, distributed via a star connection, in this configuration should ensure a constant delay between channels which can be measured and corrected for.

In order to perform the alignment needed by PSA, the digitised data have been processed with an algorithm to extract the timing information. The process is illustrated in fig 3.13 for a signal digitised from a net-charge segment, namely a segment where an interaction occurred inside. After the ”raw” signal is baseline restored, it is differentiated and summed with a delayed, inverted and amplified copy of itself. The time is then given by the zero crossing of the obtained bipolar shape. As a final refinement, the subsampling time is extracted by interpolation of the value of the samples before and after the zero-crossing. This algorithm gives a value for the timing which is independent of the amplitude of the signal. Since this technique is essentially the same signal treatment as performed in an analogical constant-fraction discriminator [92, 93], we refer to the timing algorithm used in this analysis as *digital constant-fraction discriminator* (dCFD).

The differences in time between two detectors (in this case β and γ) calculated with respect to the beginning of the trace are shown in figure 3.14.

Due to the fact that the timestamp is not accounted for, it is not possible to see just one coincidence peak, but rather many peaks are visible, each of them corresponding to a different timestamp between the signals digitised from the central contact of the two detectors. In this case, each peak has approximately a FWHM of 12 ns.

If the timestamp information is taken into account, it is possible to obtain a proper timing as shown in figure 3.15, where the difference of the times obtained applying the dCFD to the two signals of the central contact of the detectors is summed to the difference of their timestamps. Again the β and γ detectors are considered. The FWHM of the resulting time peak is 15 ns. As the sampling rate was 40 MHz, this result proves that subsampling precision is obtainable.

For the events in which only one segment is firing, the same good resolution has been obtained for most of the channels by performing the timing between a net-charge segment and the corresponding central contact. A different situation arises when the timing is performed on a transient signal. The algorithm used to get timing information from the transient signals differs from the original one according to the relevant characteristics

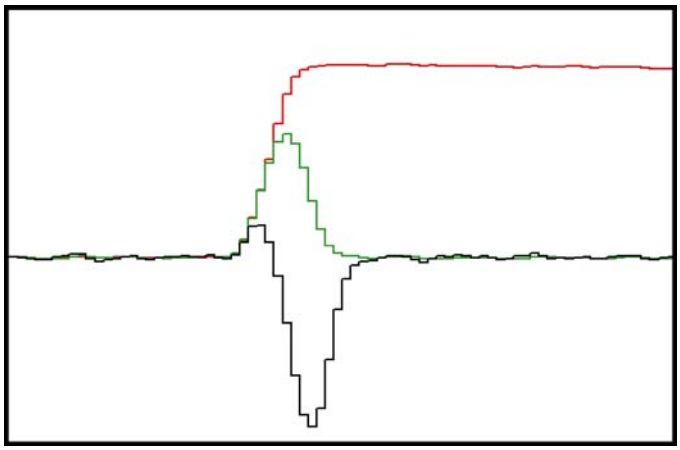

Figure 3.13: Illustration of the algorithm used to extract the timing information from the digitised signals. A baseline-restored digitised signal is shown in red; the green line corresponds to the signal shape after a differentiation. The black line indicates the final result of shaping: the differentiated signal (green) is summed with a delayed, inverted and amplified copy of itself.

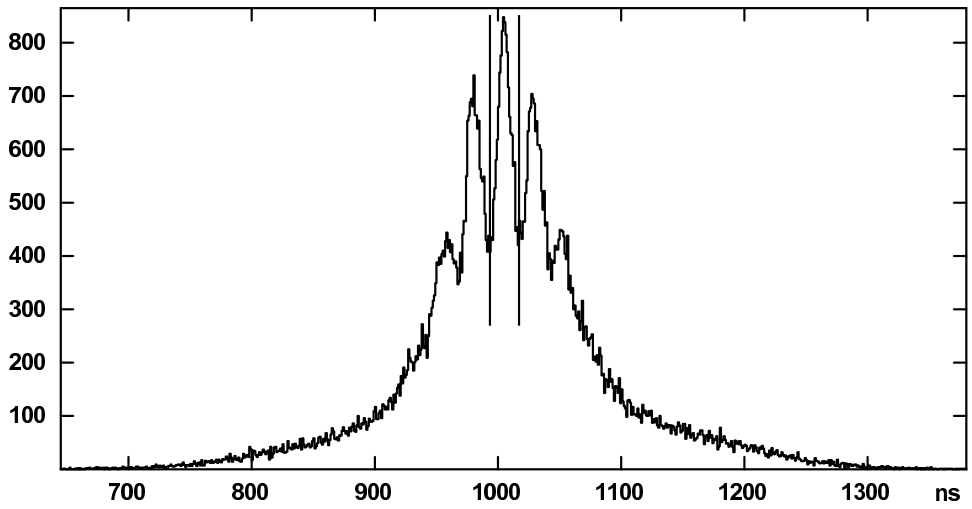

Figure 3.14: Time difference between the β and γ detectors for events in which both detectors fired. A dCFD algorithm was used. The FWHM of the highlighted peak is 12 ns.

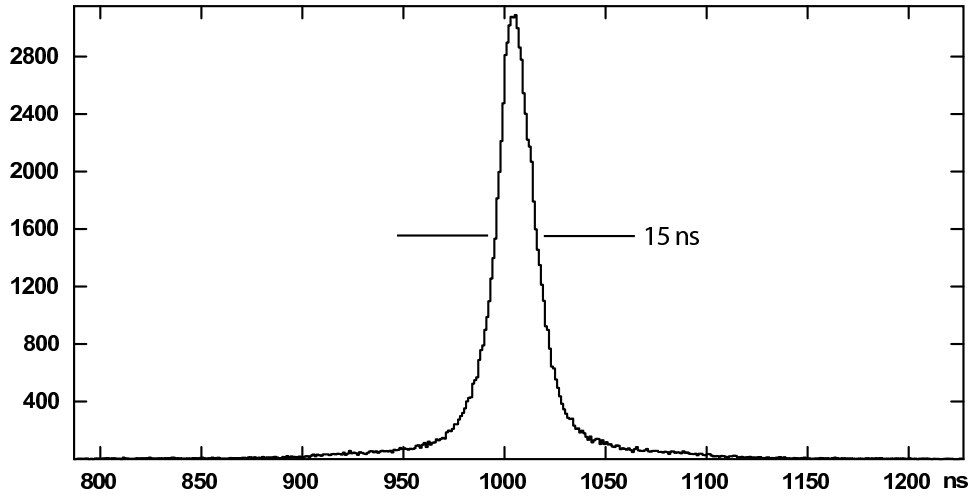

Figure 3.15: Time difference between the β and γ detectors for events in which both detectors fired. In this case a dCFD algorithm was used and the timestamp information was taken into account. The FWHM of the peak is 15 ns.

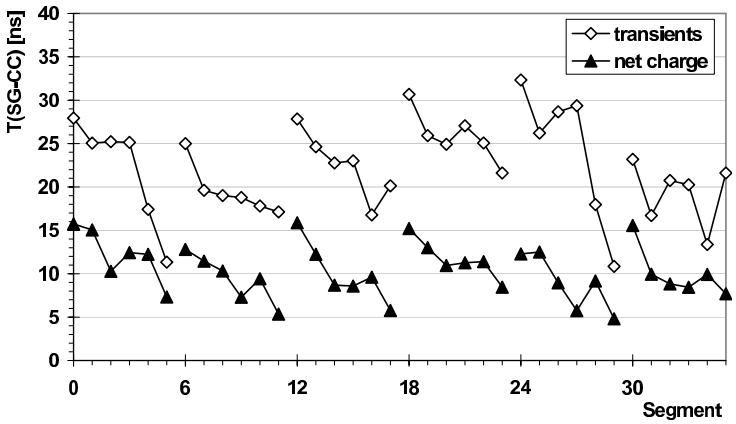

Figure 3.16: Comparison between the timing resolution obtained on transient and on net-charge segments. A threshold of 10 keV of equivalent amplitude is set on the transient signals.

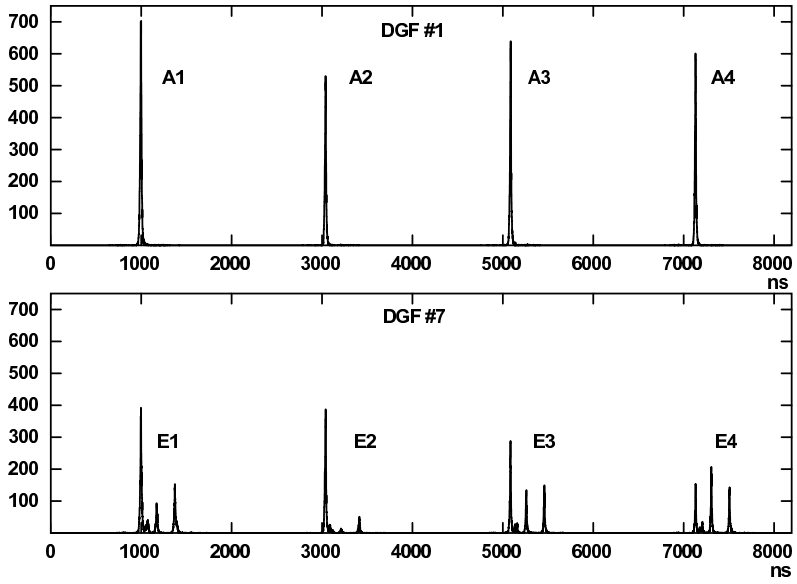

Figure 3.17: Comparison between the timing spectra obtained with signal from the first (upper part) and the seventh (lower part) DGF module in the clock distribution chain. The multiple peaks are caused by a misalignment in time.

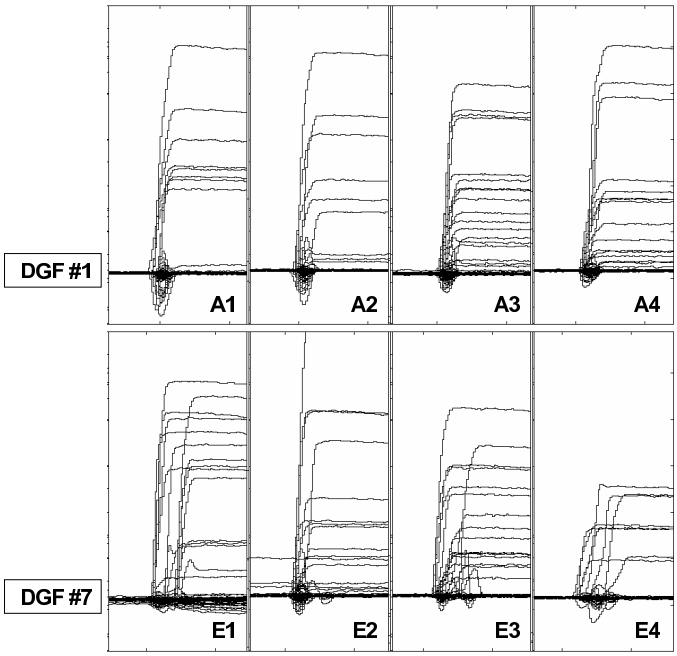

Figure 3.18: Signals from the first (upper part) and the seventh (lower part) DGF module in the clock distribution chain. Shifts in time are visible in the signals from DGF#7, particularly for segments E3 and E4.

of these signals. Since the transient signal has a null integrated current, it is possible to skip the differentiation step. In addition, the transient signal can start with alternatively a positive or a negative slope, implying that the algorithm finding the zero-crossing should be sensitive to both the positive-to-negative and negative-to-positive transitions. With these modifications to the timing algorithm, it was possible to have a good time resolution also for the transient signals. This resolution depends strongly on the signal amplitude. The timing resolution for the different transient segments is presented in figure 3.16, compared to the resolution for the net-charge signal. Only transient signals with equivalent amplitude of at least 10 keV have been considered.

Unfortunately, not all the segments resulted properly time aligned, as shown for instance in figure 3.17, where the timing spectra obtained from the segments processed by the first and the seventh DGF card in the trigger distribution daisy chain are compared for detector α. The misalignment is so macroscopic that it is possible to observe it just by looking at the digi-

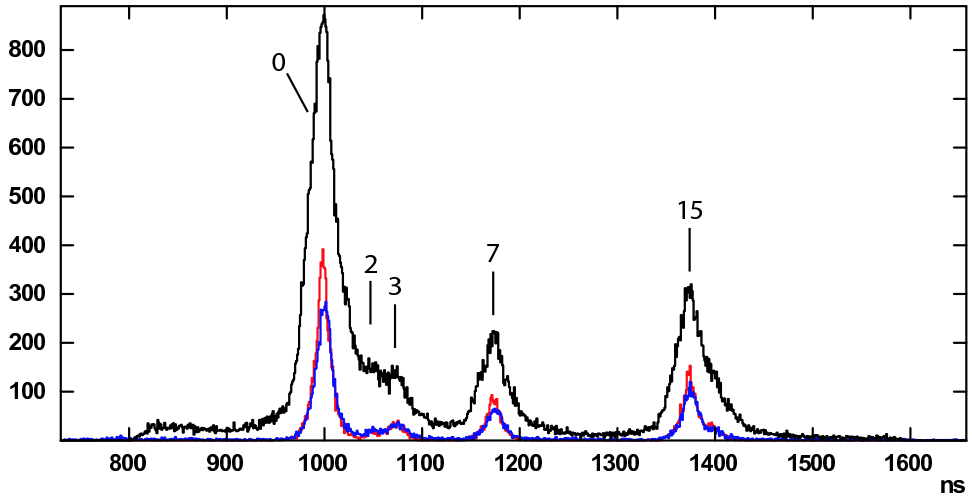

Figure 3.19: Discrete time shifts observed for segment E1 of detector α. The blue line corresponds to net-charge signals, the black line to transient signals, while the red line corresponds to the superposition of net-charge and transient signals.

tised "raw" signals, shown for instance in figure 3.18. This misalignment lead us to consider the opportunity of an event-by-event time alignment rather than a constant time shift alignment depending on the segment, as it was planned before the problem arose. A similar procedure for time alignment, considering the limited time resolution that is possible to obtain on the transient signals is very harmful for the position resolution attainable from PSA.

The timing spectrum for segment E1 of the first detector (α) is shown in figure 3.19. It is possible to see that the distribution of time differences is not a continuum, but rather five peaks are visible. All of the segments behave similarly. These time shifts can be considered as jumps of a discrete number of samples. In the case of figure 3.19, peaks corresponding to shifts of 0, 2, 3, 7 and 15 samples are visible. As a consequence, in the limit of our timing resolution, we can identify which of these peaks an event belongs to and apply a second-order correction factor depending on the number of samples corresponding to the peak. Exemplifying the procedure for segment E1 of detector α, if in an event the peak corresponding to 3 samples is incremented, the time shift for such such event will be $\Delta t_3 = \Delta t_0 + 3 \cdot 25\,\mathrm{ns}$, Δt_0 being the reference time shift corresponding to the leftmost peak.

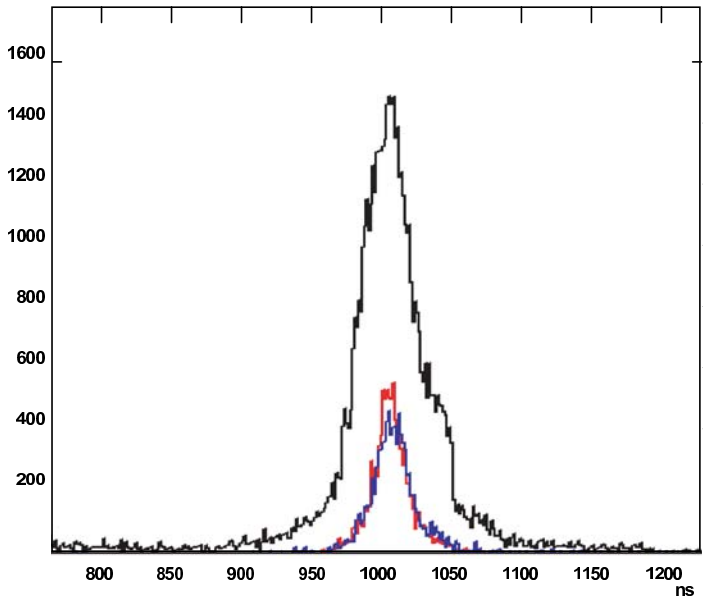

Figure 3.20: Same as figure 3.19, in which the correction for the discrete time shifts has been applied. See text for details.

Following the application of this alignment method, it was possible to obtain a good timing resolution also for the transient signals. Some ambiguity anyway still remains, as this method is based on the capability of the timing algorithm to identify the sub-peak in time spectra which the event belongs to. If for example a transient signal has a very small amplitude, it is not possible to clearly identify the peak, thus some alignment errors can arise. The spectrum shown in figure 3.20 is obtained by applying this correction to the same data shown in figure 3.19, proving that the good timing resolution was restored for the net-charge as well as for the transient signals. In this case the overall timing resolution was 10 ns for the net-charge and about 25 ns for the transient signals.

Silicon detector: cleaning the data

In order to proceed with the analysis of the germanium detectors, some operations are required to extract the information needed for the Doppler correction from the silicon detector data.

For the kind of reactions expected to take place in this experiment, only one particle per event should be detected by the silicon detector, thus only

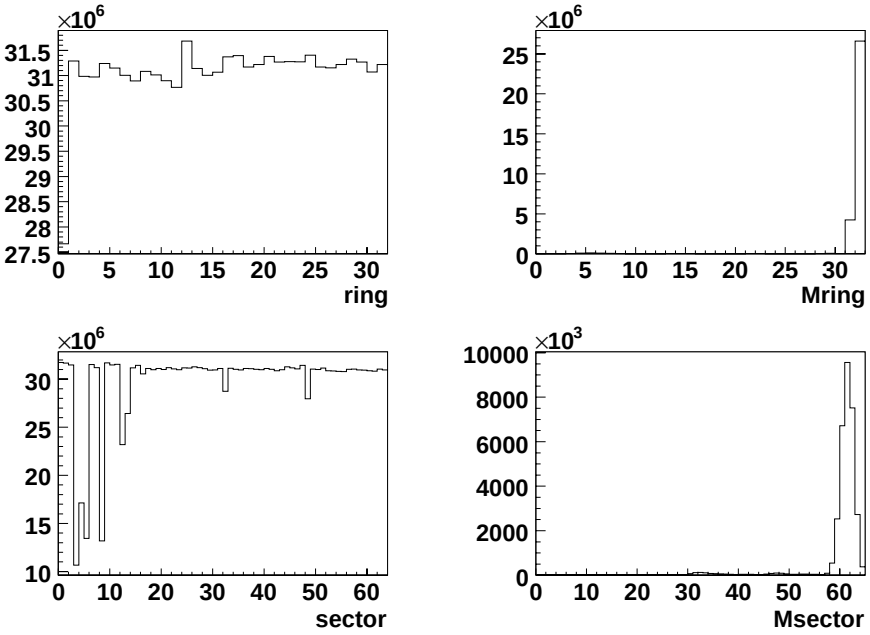

Figure 3.21: Statistics on the rings of the silicon detector (top left), multiplicity of rings firing (top right), statistics on the sectors (bottom left) and multiplicity of sectors firing (bottom right), all without conditions on the energy deposition. The fold distributions are peaked at high values.

one ring and one sector are expected to fire at a time. In fact, since the beam-like nucleus is stopped by an absorber placed after the target, only light particles can reach the silicon detector, and only one particle per event is emitted. The DAQ was designed in a way that sectors or rings with no energy deposition were not read out. However, it turned out that, probably because of noisy signals and low energy thresholds, the silicon detector was firing with almost all its channels as shown in the multiplicity plots of figure 3.21, which refer to the firing rings and segments.

In the case of the rings, the situation improves considerably by requesting a condition on the detected energy. As shown in figure 3.22, the multiplicity distribution for the firing rings with a condition on the detected energy is peaked at low values, with a maximum at fold 1 as expected. However the situation is not perfect, since higher folds are present in quite a high fraction of events.

The equivalent energy-gated plots for the sectors are in figure 3.22. The

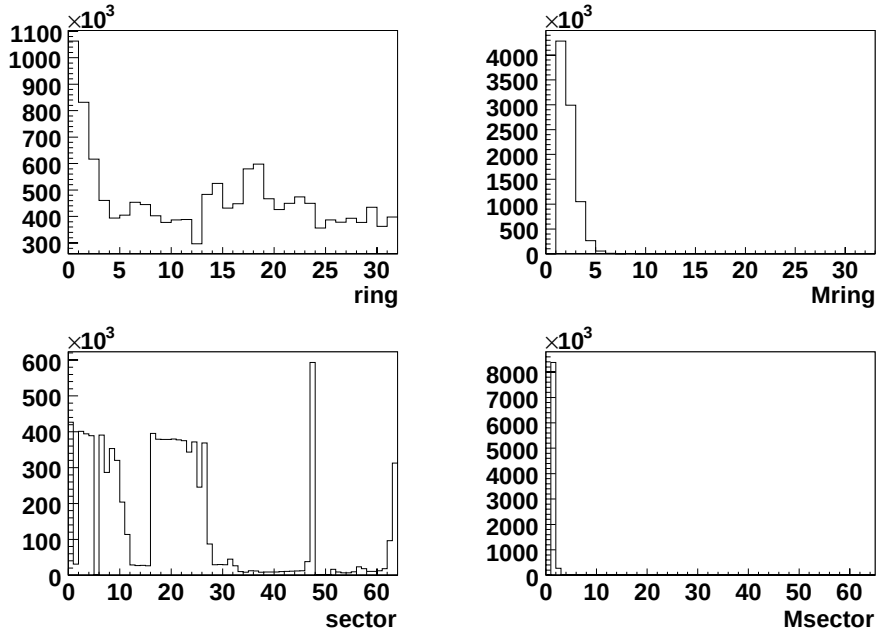

Figure 3.22: Energy-gated statistics on the rings of the silicon detector (top left), multiplicity of rings firing (top right), energy-gated statistics on the sectors (bottom left) and multiplicity of sectors firing (bottom right). The fold distributions are peaked at low values, however folds larger than 1 are observed, which is unphysical for this experiment.

distribution of figure 3.22 is different from what is expected from the symmetry of the reaction around the beam axis. Actually, in about half of the events no sector have a net energy deposition, which is not physically possible, since the same energy seen by the rings must be seen by the sectors as well. This is a clear symptom of an electronic malfunctioning, which would make it impossible to understand in which sector the particle interacted, hence losing the information on the recoil direction.

The information on the detected particle could be recovered by exploiting the timing information from the silicon detector segments. For each channel (sector or ring), the timing information was digitised using a TDC channel. The time range of the TDC was 100 ns. This part of the acquisition system turned out to be fundamental for the identification of the firing segment. In fact for all but one of the firing sectors and all but one of the firing rings this time was missing (i.e. the TDC was in overflow). The real firing

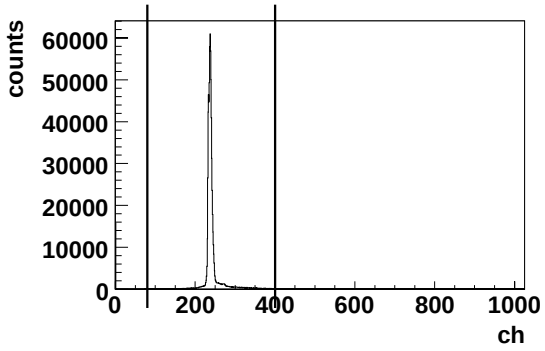

Figure 3.23: Time spectrum of the auto-coincidence of a sector of the silicon detector. The gate, set between channels 80 and 400, is shown. This gate is only a validation to identify whether the sector is actually firing.

sector as well as the real firing ring could therefore be selected through the proper condition on the timing signals as shown in figure 3.23. The multiplicity of firing segments in most of the events is 1 as expected and the distribution of statistics over the sector number, shown in figure 3.24, is flat except for a few malfunctioning channels. Some segments are not firing as expected (number 1, 27, 28, 31, 32, 35, 36, 53, 54, 56 and 57) and some other appear to be in short-circuit (47, 48 and 49 seen all as channel 47; 50 and 51 seen both as channel 51). The resulting matrix of statistics of rings versus sectors is presented in figure 3.25. It is possible to see that all of the rings are properly working, differently from the sectors where the above mentioned problems are evident.

Silicon detector: numbering and positioning

In order to perform a proper Doppler correction, it is necessary to know the position of each segment of the silicon detector. In practice, the correspondence between ring / segment number and its position must be found, in particular:

- the polar angle (θ) corresponding to each ring;
- the azimuthal angle (ϕ) corresponding to each segments.

The relative position of the rings of the silicon detector can be deduced by looking at the calibration run where an alpha source was put in the target

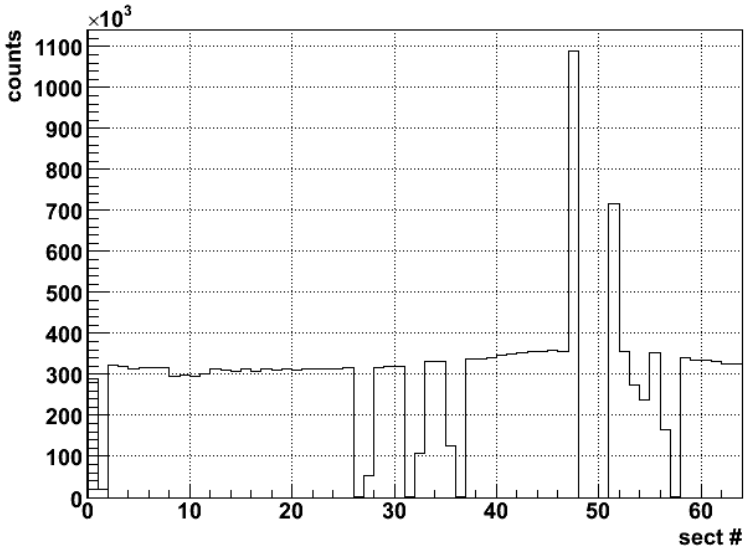

Figure 3.24: Distribution of firing sectors identified from the auto-coincidence in time.

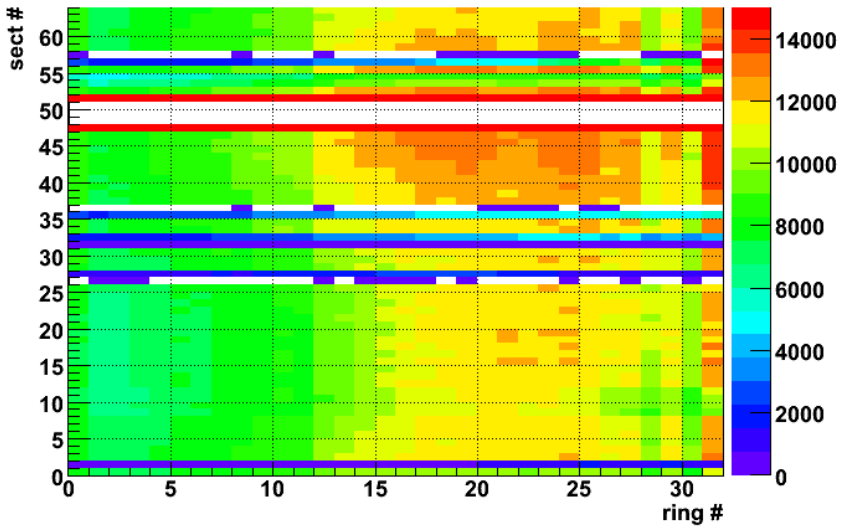

Figure 3.25: Firing segment versus firing ring. The distribution is in agreement with what can be expected from the kinematics of the reaction.

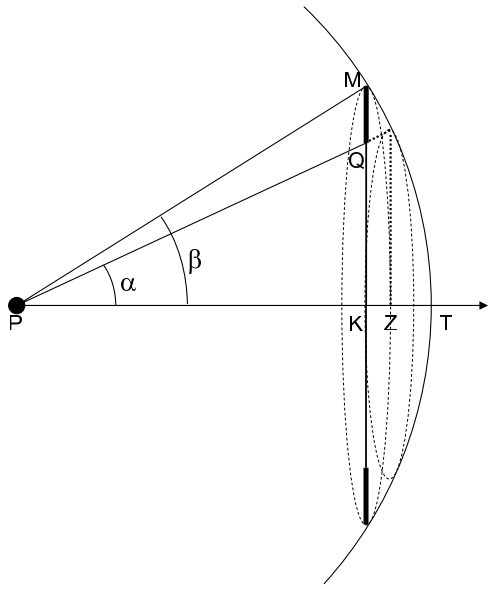

Figure 3.26: Side view of the silicon detector. PK is the distance (D) between the alpha source and the silicon detector, QK is the internal radius (R_{int}) and QM is the segmentation step (S) of the silicon detector.

position. The distribution of the hits over the sectors can be predicted analytically from the geometry of the setup. The parameters on which the analytical formula depends can be extracted through a fit of the experimental data.

The predicted hit distribution depends on the solid angle subtended by each ring with respect to the alpha source. We start for instance by calculating the solid angle subtended by the most external ring. Looking at figure 3.26 it is clear that such value can be obtained by subtraction of the solid angle subtended by the spherical cap of half-opening angle $K\widehat{P}Q$ (α from now on) from the solid angle subtended by the spherical cap of half-opening angle $K\widehat{P}M$ (β from now on):

$$\begin{aligned} \Omega &= \frac{2\pi \mathbf{PM}\cdot\mathbf{KT} - 2\pi \mathbf{PM}\cdot\mathbf{ZT}}{|\mathbf{PM}|^2} \\ &= 2\pi\left(\cos\alpha - \cos\beta\right) \end{aligned} \tag{3.4}$$

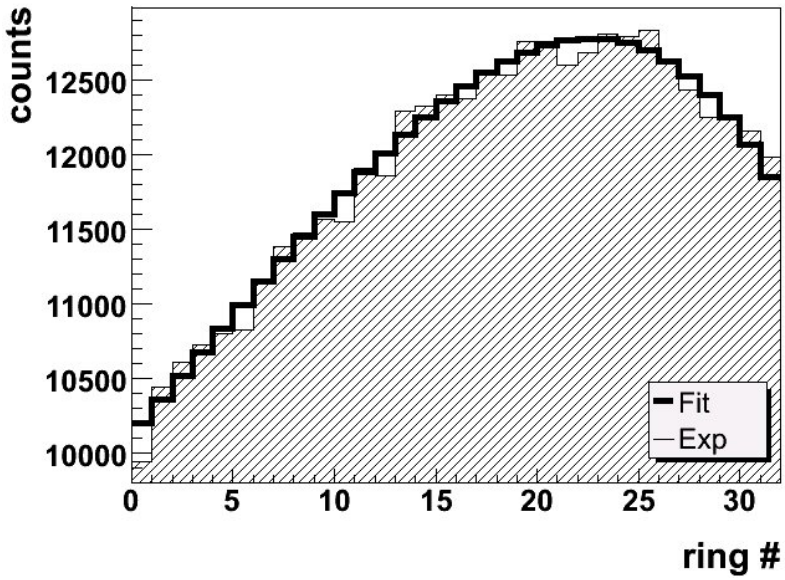

Figure 3.27: Experimental distribution over the different rings of the alpha particle detected in a calibration run. The fitting function is in equation 3.5c.

This can be generalised to calculate the solid angle Ω_i subtended by the i-th ring:

$$\begin{aligned}
\alpha_i &= \arctan\frac{R_{int}+s\cdot i}{D} \\
\beta_i &= \arctan\frac{R_{int}+s\cdot(i+1)}{D} \\
\Omega_i &= 2\pi\cdot\cos\left(\arctan\frac{R_{int}+s\cdot i}{D}\right)+ \\
&\quad -2\pi\cdot\cos\left(\arctan\frac{R_{int}+s\cdot(i+1)}{D}\right)
\end{aligned} \tag{3.5}$$

Since the internal radius and the segmentation step of the silicon detector are known, the only free parameter in the last of equations 3.5 is the distance D of the silicon detector from the source. The optimal value of this parameter can be extracted through a fit of the experimental data as shown in figure 3.27. The optimal value turned out to be $D = 34$ mm, in good agreement with the known 35 mm target-detector distance. As a byproduct, the correct numbering of the rings of the silicon detector was determined, choosing between the two alternatives (ring #0 could correspond either to

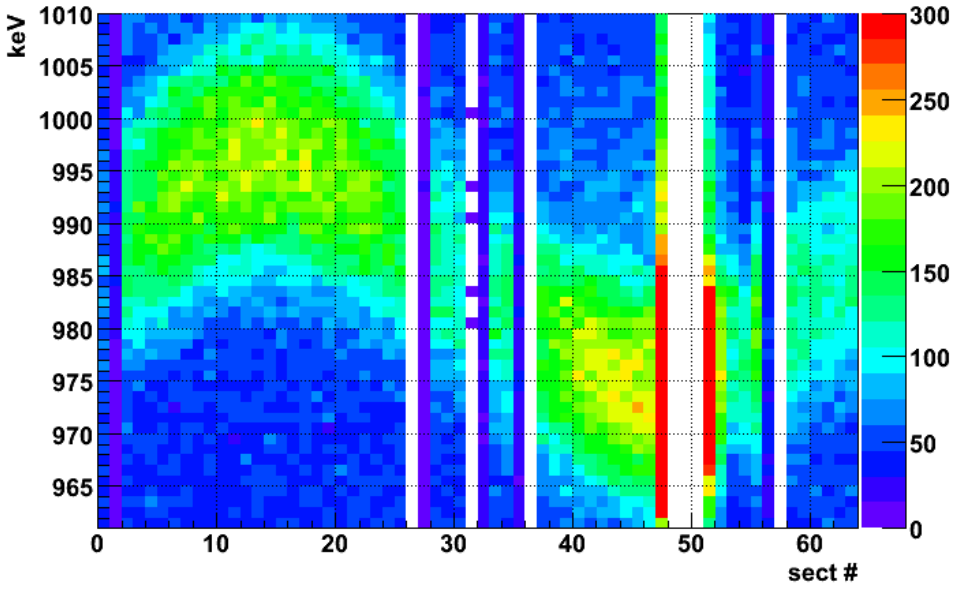

Figure 3.28: Photon energy versus firing sector.

the inner or to the outer ring; in our case the correct solution was the latter).

In order to identify the correct numbering of the sectors and the ϕ rotation around the beam axis, the Doppler correction was employed. The Doppler-shift formula contains the dependence on the sector firing through the angle θ between the photon and the recoil directions and also through the recoil velocity module β. The uncorrected energy of a strong peak will depend on the firing sector as shown for instance in figure 3.28 for the 984 keV line. Knowing the reaction kinematics, as it will be discussed in the next section, it is possible to extract the value of the rotation angle around the beam axis which best reproduces the energy oscillation through a fit to the experimental data. The best fit curve shown in figure 3.29 corresponds to an angular position ϕ_0=12.3° for sector #0. The fitting formula for this calculation was derived numerically. The resulting detector arrangement is sketched in figure 3.30.

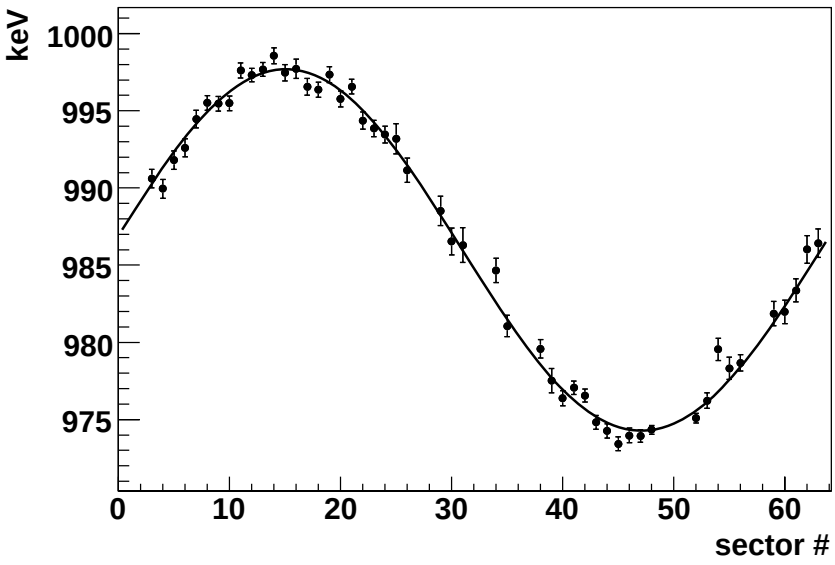

Figure 3.29: Peak position versus firing segment. The best fit curve shown as a continuous line was calculated numerically.

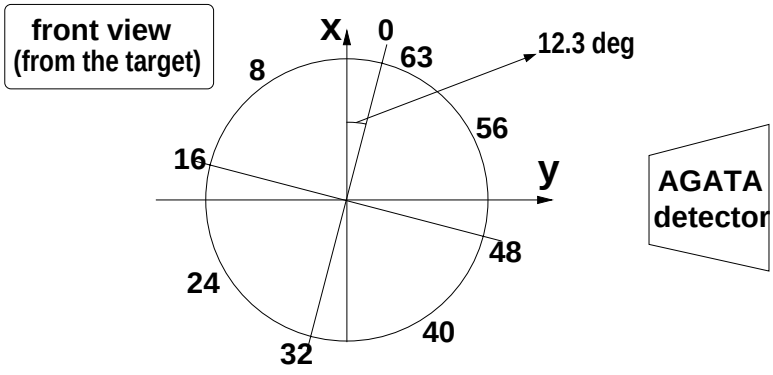

Figure 3.30: Position and numbering of the sectors of the silicon detector.

Silicon detector: positioning

When looking carefully at figure 3.25, it is possible to notice the presence of a small anisotropy in the statistics depending on the firing sector. This was not expected and therefore it was investigated in detail.

Since the symmetry with respect to the rotation around the beam axis has to be strictly satisfied by the reaction kinematics, the only way to create such anisotropy is a misalignment of the silicon detector with respect to the beam axis. Two are the possible reasons:

- the plane in which the silicon detector lays is not orthogonal to the beam;
- the beam is not passing through the centre of the silicon detector.

It should be remarked that it is not possible on the basis of the experimental data alone to discern between the two alternatives because, with an appropriate choice of the parameters, they produce exactly the same effects. As a consequence, there will be no difference in assuming either of them for the Doppler correction. Therefore, in this section a quantitative estimate for each case is provided.

In order to have a more quantitative feeling of the mispositioning, the problem should be simplified. The particular kinematics of a direct reaction implies that for a fixed angle between the detected particle and the beam axis, two energies at most are allowed for that particle. In the case of a fusion-evaporation reaction, this is not true since the centre-of-mass spectrum of the evaporated particles is a continuum. A matrix of the distribution of counts in rings versus the counts in sectors was produced, selecting only events with a particular range of energy deposited in silicon detector, corresponding to the direct reaction channel (as will be discussed in more detail in the next section). This matrix is shown in figure 3.31. In the case of a direct reaction, the kinematical problem has only one solution so that there is a univocal correspondence between energy and angle.

If the silicon detector were aligned with the beam, we would expect the stripe in figure 3.31 to be a horizontal line. The shift from linearity of the stripe of figure 3.31 can be parameterised and the optimal values of the parameters can be extracted through a fit to the experimental data, producing the plot shown in figure 3.32.

In the former assumption of mispositioning, the fit gives an angle between the plane orthogonal to the DSSSD and the beam $\theta = 4.5°$ in the direction of sector number 19. In the latter assumption, the optimal value of the distance between the centre of the DSSSD and the beam is 2.7 mm, again with a displacement towards sector number 19.

The alternative situations are depicted in figure 3.33. The observed effect could actually be due to a combination of the two causes of mispositioning.

Germanium detectors: a posteriori positioning

In order to perform properly the Doppler correction, the position of the germanium detector with respect to the target should be measured with a precision of the order of a millimetre. In practice, such value could not be reached with the actual mechanical setup and the position of the detectors had to be inferred from the experimental data. More precisely we considered as the detector position the value giving optimal Doppler shift. The accuracy of this "a posteriori" positioning will depend critically on the precision with which the position of the interactions inside the detectors are known. In principle, the positions provided by a PSA algorithm could be

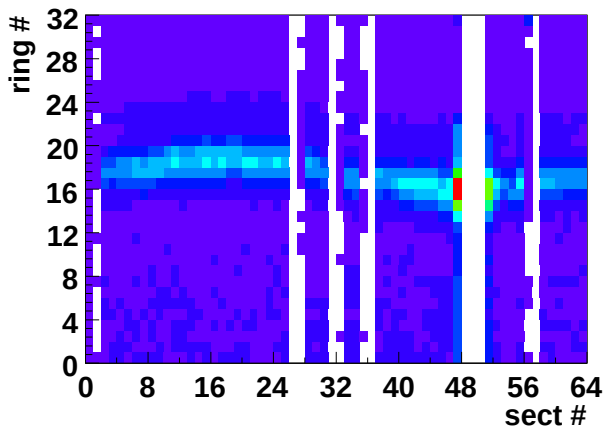

Figure 3.31: Counts in ring versus counts in sectors for events with an energy deposited inside the silicon detector between 8 and 12 MeV.

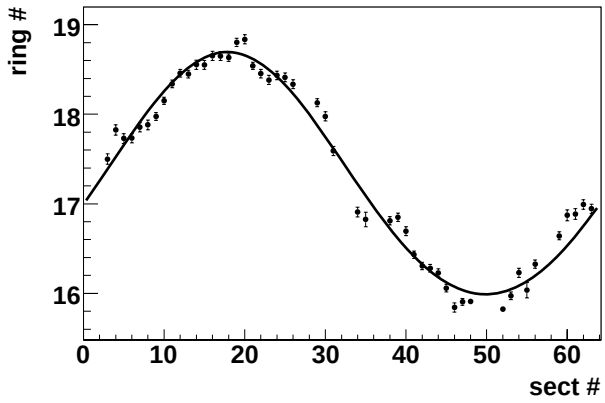

Figure 3.32: Misalignment of the silicon detector. If the silicon detector were aligned with the beam we would expect the points to lie on a horizontal line.

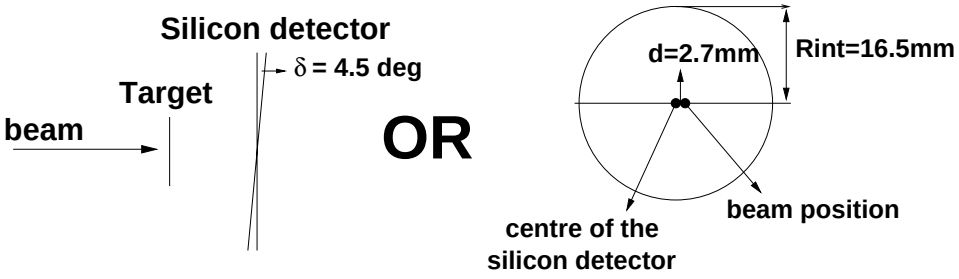

Figure 3.33: Two possible causes for the misalignment of the silicon detector.

used, but in this case this procedure could lead to meaningless results. As a matter of fact, both the PSA algorithm parameters and the position of the detector are varied trying to minimise the width of the Doppler-corrected peaks. It is possible that the two concurring optimisation processes simply cancel mutually obtaining a good Doppler correction as a result of two biased procedures. For example, if the PSA algorithm systematically estimates in a wrong way the position of the interactions moving them towards the front face of the detector, the “a posteriori” positioning algorithm will correct for this effect by moving the whole detector in the backward direction. For this reason, it was decided to rely on a more robust method,

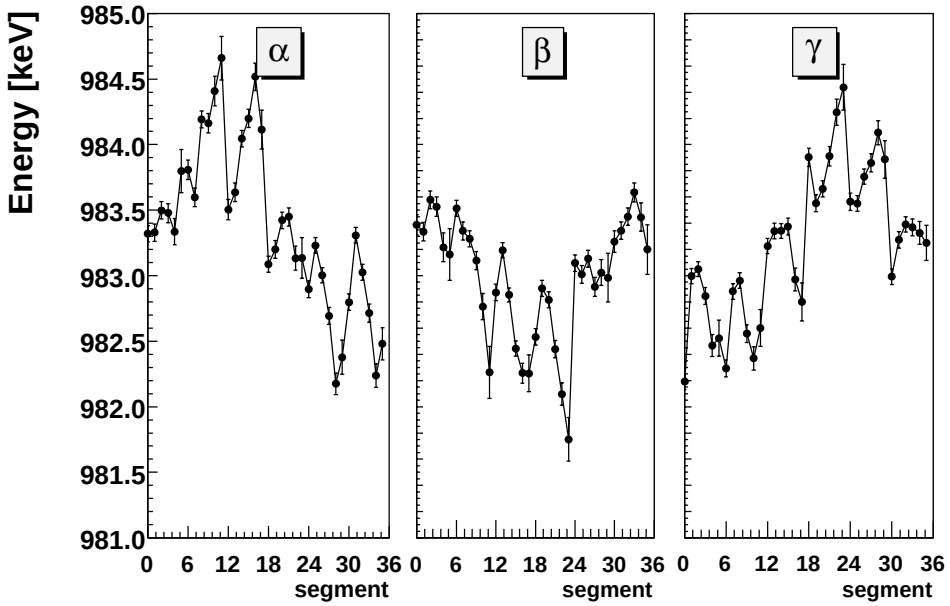

Figure 3.34: Position of the peak at 983.5 keV as a function of the segment firing. In case of perfect alignment all the points should be at 983.5 keV.

although less sensitive, during the "a posteriori" positioning of the detector, by assuming that each interaction takes place in the centre of the firing segment, rather than using the more precise position provided by a PSA algorithm.

The position of a solid in a 3-dimensional space is uniquely identified by 6 parameters, for example by 3 coordinates and 3 Euler angles. In order to extract these parameters from the experimental data, our algorithm looks for the optimal Doppler correction using an "inverse strategy", namely by transforming the known intrinsic energy of the photon to the laboratory reference frame. The transformation function will depend on the six parameters mentioned above, which can be extracted from the experimental data through a multidimensional fit for which the Minuit fitter from the ROOT suite [94] was used.

In principle, one would like to perform the multidimensional fit on a cube having on the three axes respectively:

1. germanium segment firing [36x3 = 108 bins];

2. silicon pixel firing grouped in 4x4 squares [64*32 / (4x4) = 128 bins];

3. energy of the γ-ray as measured by the central contact, without applying Doppler correction; a broad gate around 1382 keV was set [16384 bins];

The resulting cube has too large a size (108x128x16384) for a direct fit to be feasible, hence we had to reduce the problem to a fit of smaller bidimensional matrices. The matrix which was actually fitted is a 2D matrix "A" having on the two axes:

1. germanium segment firing [36x3 = 108 bins];

2. silicon pixel firing grouped in 4x4 squares [64*32 / (4x4) = 128 bins];

The content of this matrix "A" at channel $(\mathrm{ge}_i, \mathrm{si}_j)$ was a weighted average of the energy spectrum seen by germanium segment ge_i in coincidence with silicon pixel si_j:

$$\langle E_\gamma \rangle_{ij} = \frac{\int_{E_\gamma} E_\gamma \cdot n(E_\gamma) \cdot \mathrm{d}E_\gamma}{\int_{E_\gamma} n(E_\gamma) \cdot \mathrm{d}E_\gamma} \tag{3.6}$$

where in our case the integrals were transformed into discrete sums running on the channel number. The uncertainty associated to channel $(\mathrm{ge}_i, \mathrm{si}_j)$ was taken as the content of the 2D matrix "B" obtained by projecting the original cube on the third axis, that is the number of times that germanium segment ge_i was firing in coincidence with silicon pixel si_j.

The function used to fit matrix "A" takes the position of the particle interaction on the silicon detector to calculate the direction of the recoil; the direction of the photon, depending on the six parameters mentioned above, is used to transform the intrinsic photon energy from the centre-of-mass to the laboratory reference frame.

Using the 6 parameters (3 coordinates and 3 Euler angles) extracted from the experimental data as discussed above, Doppler correction was performed by deducing the direction of the photon from the centre of each segment. Unfortunately, the position of the peaks turned out to be slightly dependent on the specific segment, implying that our "a posteriori" positioning is affected by an unknown systematic error. For instance, the distribution of the positions of the 984 keV peak as a function of the firing segment is reported in figure 3.34. A dispersion of the points around the "true" value is apparent, with a FWHM$\approx$1 keV. It should be remarked that

further attempts were performed in order to improve the “a posteriori” positioning, both based on automated or on manual procedures, however the alignment value could not be improved.

3.5 Channel selection and reaction mechanism

Several matrices were constructed in order to understand which reaction channels were populated from both fusion-evaporation and direct mechanisms. It should be remarked that, according to the theoretical estimates, the probability to populate channels via fusion-evaporation was larger than the probability to populate the same channels with direct reactions.

The plot shown in figure 3.35 is a ring-energy correlation matrix for the charged particles detected by the silicon detector, requesting a coincidence with the 1382 keV line of ^{49}Ti. Given the univocal correspondence between ring and angle, this matrix and the ones presented in the rest of the section are actually equivalent to angle-energy correlation matrices. The theoreti-

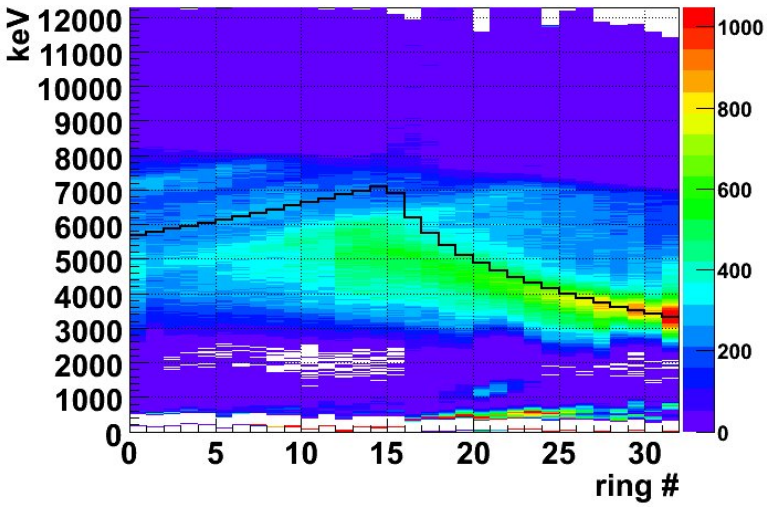

Figure 3.35: Distribution of energy versus ring number for the silicon detector. A coincidence with photon energy around 1382 keV is required. The amount of energy deposited in the silicon detector by the protons coming from the (d,p) direct reaction channel was calculated fitting the parametric calculation to the experimental distribution.

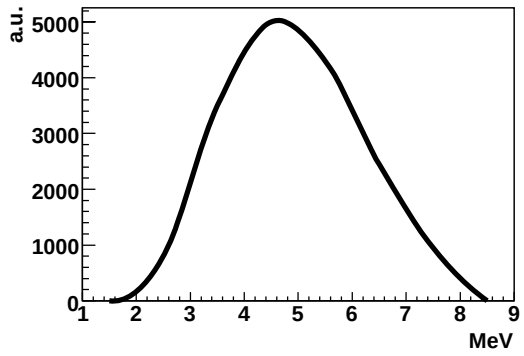

Figure 3.36: Centre-of-mass energy distribution for the evaporated protons from the d(^{48}Ti,^{49}Ti)p reaction.

cal value for the energy deposited by the particles in the silicon detector at different angles assuming a direct reaction mechanism is shown as a dark overlapping line. The prediction on the energy deposition inside the silicon detector is obtained by using a parametric stopping power calculation program and taking into account the target thickness, the aluminium absorber and the silicon detector thickness after the centre-of-mass energy has been transformed to the laboratory reference frame.

Concerning the fusion-evaporation reaction mechanism, a calculation using PACE [95] was performed, obtaining the centre-of-mass energy spectrum for the evaporated protons that is sketched in figure 3.36. Given the continuum distribution of this spectrum, we had to calculate the energy deposition inside the silicon detector corresponding to several centre-of-mass energies as shown in figure 3.37.

The comparison of figures 3.35 and 3.37 is consistent with the calculations performed with PACE [95] and CASCADE [96], suggesting that the cross section for the fusion-evaporation is much larger than the cross section for the direct reaction channel. By requesting the coincidence with the 984 keV peak of ^{48}Ti, we obtain instead the ring-energy correlation matrix shown in figure 3.38. The ^{48}Ti excited nuclei could be produced either via fusion-evaporation ^{48}Ti+d $\rightarrow ^{50}$V* $\rightarrow ^{48}$Ti + p + n or through a Coulomb excitation ^{48}Ti(X,X')^{48}Ti* on the nucleus X. The former population mode is expected to produce counts in the highlighted region in figure 3.38. Actually, since background was not subtracted in producing the matrix in

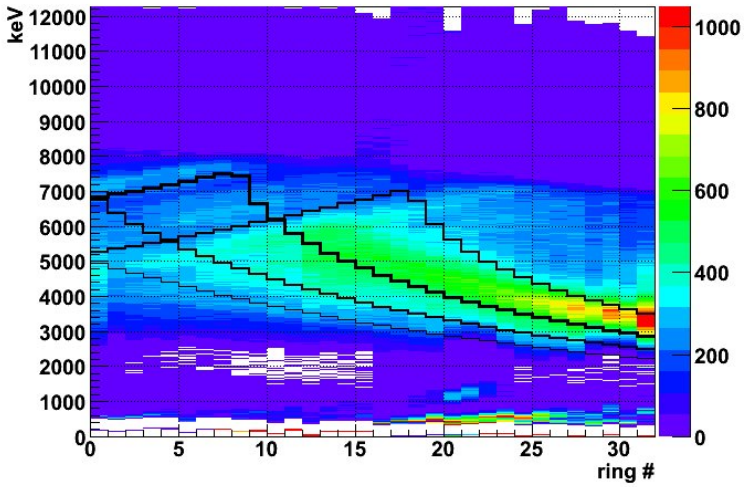

Figure 3.37: Distribution of energy versus ring number for the silicon detector. A coincidence with photon energy around 1382 keV is required. The amount of energy deposited in silicon detector by the protons coming from the (d,p) fusion-evaporation reaction channel was calculated using the centre-of-mass energy spectrum given by PACE [95]. The different lines correspond to different energies of the protons in the centre-of-mass. From bottom to top, 6.5, 5.5, 4.5 and 3.5 MeV are considered respectively. The thickest line corresponds to 4.5 MeV.

figure 3.38, part of the counts on this region could be originated from a spurious reaction, producing a higher-energy photon undergoing Compton escape. Assuming instead a ^{48}Ti Coulomb excitation on deuterium, the overlapping line of figure 3.39 is obtained, for which a correspondence is found on experimental data.

The interpretation for the structures observed in the matrix and highlighted in figure 3.40 is less immediate. The possible reaction channels causing such energy depositions in the silicon detector can be guessed by investigating the Doppler correction coefficients that should be used for the photons in coincidence with such areas. This can be performed by looking at the energy deposited in germanium detectors as a function of the silicon sector firing and requesting the coincidence with the particular regions highlighted in figure 3.40. This produces the plot shown in figure 3.41.

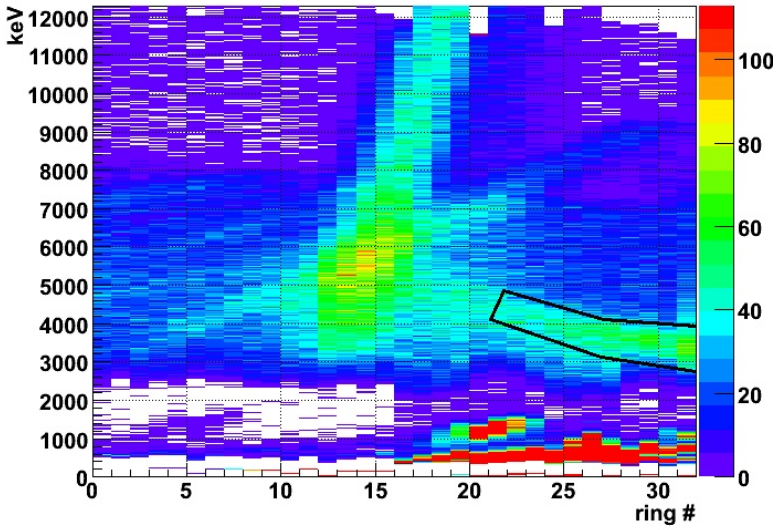

Figure 3.38: Distribution of energy versus ring number for the silicon detector. The matrix is incremented requesting the coincidence with the 984 keV line detected with the AGATA detectors. The highlighted region corresponds to the expectation for a (d,pn) reaction.

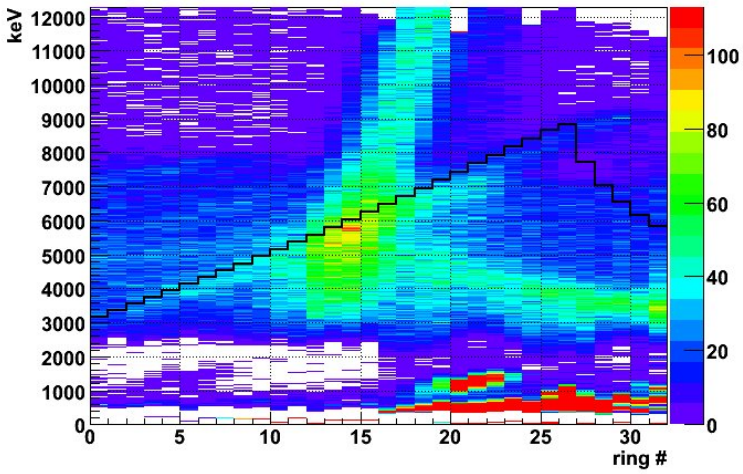

Figure 3.39: Same matrix as figure 3.38. The overlapped line corresponds to the expectations for the (d,d') channel.

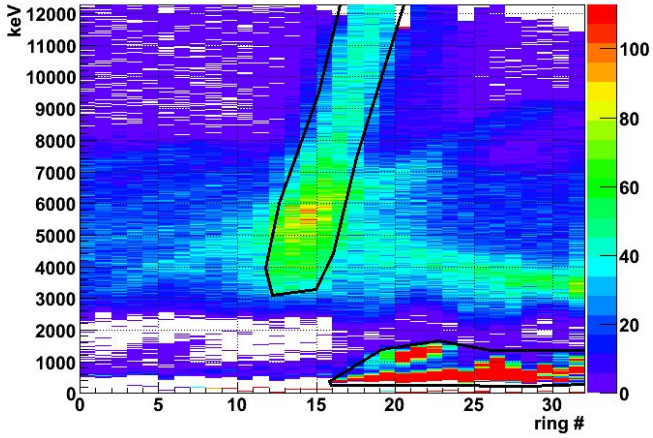

Figure 3.40: Same matrix as figure 3.38. The highlighted regions correspond to reaction on contaminants. See text for details.

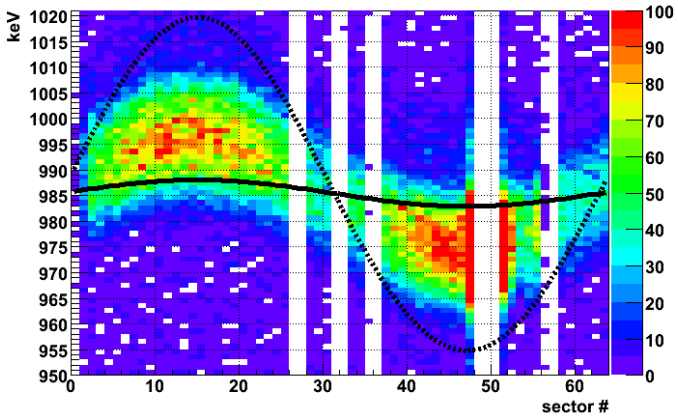

Figure 3.41: Correlation matrix of energy deposited in the AGATA detectors versus DSSSD sector firing. The overlapped line correspond to scattering on deuteron (continuous line) or ^{48}Ti (dotted line).

The overlapped curves show the expected behaviour for two Coulex reactions, namely d(^{48}Ti, ^{48}Ti*)d' and ^{48}Ti(^{48}Ti, ^{48}Ti*)^{48}Ti. It is clear from figure 3.41 that the experimental data are not reproduced by assuming such reactions. As a consequence, a suitable reaction on an intermediate mass element which could be present as a contaminant should be looked for.

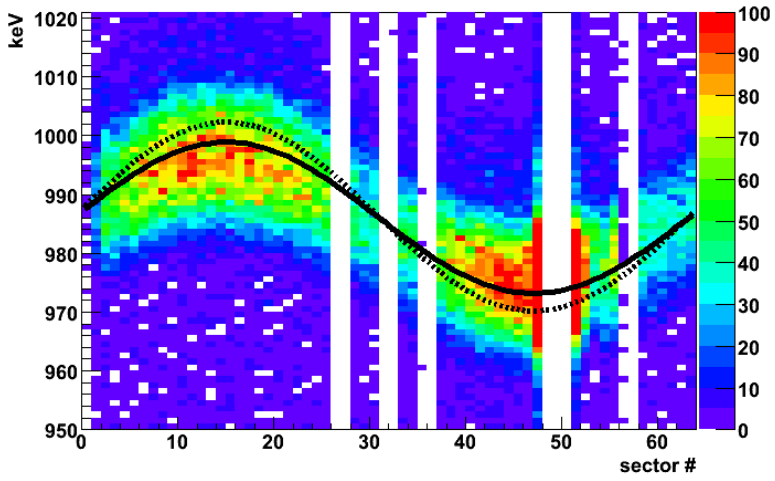

Figure 3.42: Same matrix as figure 3.41. The overlapped lines correspond to scattering on ^{12}C (continuous line) or ^{16}O (dotted line).

Typical contaminants are for instance ^{12}C or ^{16}O, and, in effect, the distribution corresponding to these scatterer nuclei is in good agreement with the experimental data.

A further check on the origin of the highlighted regions in figure 3.40 was performed through a parametric calculation of the energy deposition inside the silicon detector for the case of Coulex scattering of ^{48}Ti on carbon, nitrogen and oxygen, as presented in the plot of figure 3.43. The results of this calculation should be interpreted only qualitatively since the thickness of the absorber placed in front of the silicon detector was relevant for this calculation and it is not known with sufficient accuracy.

We conclude that the high-energy highlighted region seems consistent with the elastic scattering of ^{48}Ti on a contaminant. The same explanation holds for the low-energy highlighted region, although in this case the model should be refined. Very high-energy signals are not recorded by the DAQ, which was programmed to suppress the channels in overflow, but at the same time they can induce crosstalk signals in the neighbouring segments, which are those actually recorded. This is supported by the matrix in figure 3.44 which was constructed by putting a gate in the low-energy highlighted region of figure 3.40. Since the matrix of figure 3.44 looks quite similar to that of figure 3.42, again the model seems consistent with the

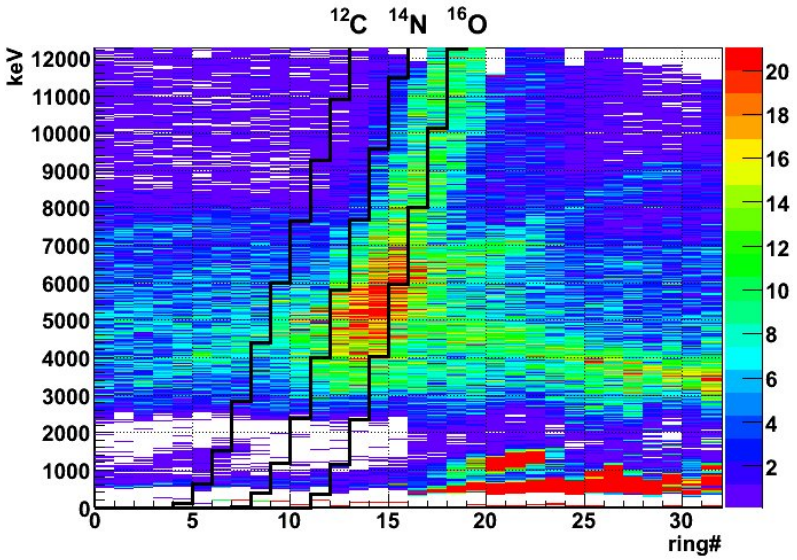

Figure 3.43: Same matrix as figure 3.38. The overlapped lines correspond to scattering on ^{12}C, ^{14}N and ^{16}O.

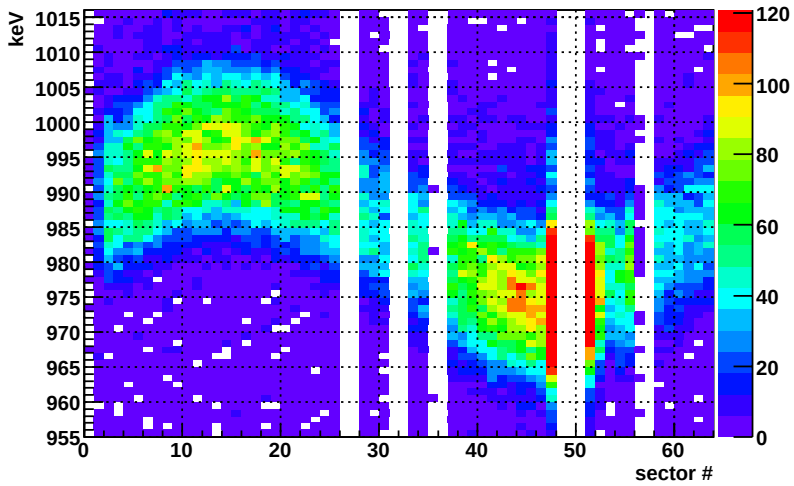

Figure 3.44: Correlation matrix of energy deposited in the AGATA detectors versus DSSSD ring firing requesting the coincidence with the low-energy highlighted region of figure 3.40.

scatterer nucleus	resolution [keV]
^{10}B	9.4
^{12}C	6.8
^{14}N	8.8
^{16}O	10.5

Table 3.1: Peak FWHM of the Doppler-corrected 984 keV line assuming various scatterer nuclei. The position of the first interaction in the AGATA detectors is assumed to lie in the centre of the segment firing with the largest amount of deposited energy.

experimental data.

Since the germanium detectors were placed as close as possible to the target to enhance the Doppler broadening, the energy resolution is not sufficient to decide whether the contaminant is ^{12}C or ^{16}O. A Doppler-corrected spectrum was constructed, assuming that the first interaction occurred in the centre-of-gravity of the segment having the largest energy deposition. The results assuming several contaminant nuclei are reported in table 3.1. We conclude that the most likely contaminant is the one producing the narrowest peak, which in our case is ^{12}C. This is also the most natural contaminant to expect in the vacuum chamber which is accumulated in the target as a consequence of beam-induced sputtering processes.

3.6 Monte Carlo simulation

As anticipated earlier in this chapter, the main goal of the measurement was to estimate experimentally the position resolution attainable with the available PSA algorithms. As explained in section 3.2 such estimate is obtained from the quality of the Doppler-corrected spectra, namely from the broadening of the peaks. Actually, the resulting peak width originates from several independent contributions, many of which cannot be evaluated consistently. Therefore, it is not possible to construct a parametric model and the expected peak width should be obtained with a Monte Carlo simulation taking into account all of the relevant effects.

In this work, the Monte Carlo code developed for the optimisation of the geometry of AGATA, described briefly in section 2.4, was used [97].

The description of the DSSSD (including the aluminium absorber) and of the symmetric triple cluster were implemented. A pictorial view of the simulated setup is shown in figure 3.45.

In order to reproduce the experimental conditions, it is important to include a "realistic" treatment of the reaction kinematics. For this reason the AGATA Monte Carlo code allows the user to provide an input file containing an event-by-event description of the particles that have to be fired. An event generator program has been written in order to produce such input for the simulation. This program takes the cross sections from a calculation made with the parametric fusion-evaporation code CASCADE [96] and chooses a residual nucleus accordingly for each event. The particles needed to populate the residual nucleus are evaporated by the compound nucleus assuming the centre-of-mass spectra calculated by CASCADE. The photon cascade corresponding to the residual nucleus is generated using the GAMMAWARE package [98] in accord to the known discrete level spectrum and branching ratios. As explained in section 3.5, the most probable reaction mechanism for the production of ^{49}Ti in our experiment is fusion-evaporation, hence the event generator based on CASCADE fits the experimental case. The angular and energy dispersion of the beam, resulting from the beam emittance and the straggling inside the target, were evaluated through a Monte Carlo calculation performed with the SRIM code [83]. Since such values are relevant for the final peak width evaluation, they were fed to the AGATA code.

The Monte Carlo code gives an output similar to the data recorded in a real experiment. The single interaction points inside the AGATA detector

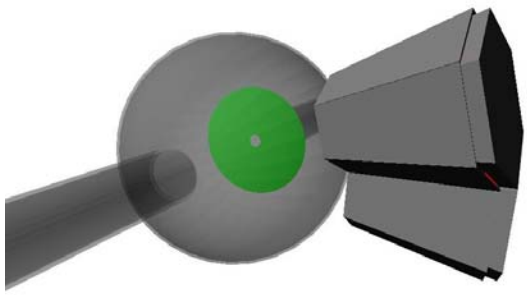

Figure 3.45: Pictorial view of the setup used for the GEANT4 simulation of the present experiment.

are provided together with the energy deposited in the DSSSD detector. All of these values are given with arbitrary precision, i.e. the finite resolution of the detectors is not taken into account. For this reason the simulated data have been further processed by applying a smearing in the energy of the interactions, i.e. the exact values given by the Monte Carlo simulation have been changed according to the energy resolutions of the detectors measured during the calibration runs. It should be remarked that these values depend on the specific crystal.

A smearing was applied to the positions of the interaction points as well. First, to mimic the behaviour of the PSA algorithm used to analyse the data (see the following section) the interaction points within a same segment were packed into a single point corresponding to their centre-of-gravity. An energy corresponding to the sum of the individual energies was assigned to such point. An energy-dependent position smearing was then applied, using a 3-dimensional gaussian distribution having FWHM:

$$FWHM = FWHM_0\sqrt{\frac{E_0}{E_\gamma}} \tag{3.7}$$

where $E_0 = 1382$ keV and E_γ is the energy of the interaction point. This expression could result in very small values of FWHM which are not likely, therefore a minimum value FWHM$_{min}$ = 2 mm was considered.

The simulated data were Doppler-corrected by deducing the recoil vector velocity from the DSSSD information in a way consistent with what was done for the experimental data, namely by deducing the vector velocity of the recoiling nucleus from the direction of the firing ring / sector of the silicon detector. The resulting FWHM for the 1382 keV of ^{49}Ti is shown in figures 3.46, 3.47 as a function of the smearing FWHM$_0$. In the plot of figure 3.46, all segment multiplicities are considered, while in figure 3.47 only segment multiplicity 1 is taken into account. It should be remarked that the resulting peak width is slightly larger at multiplicity 1 than at higher multiplicities. Actually, at this photon energy, it is unlikely that the photon undergoes direct photoelectric absorption and the most probable sequence is (multiple) Compton scattering followed by photoelectric absorption. Assuming that the whole scattering sequence takes place in the same segment, the centre of gravity of the interaction point could differ considerably from the first interaction point, resulting in a worsening of the Doppler correction.

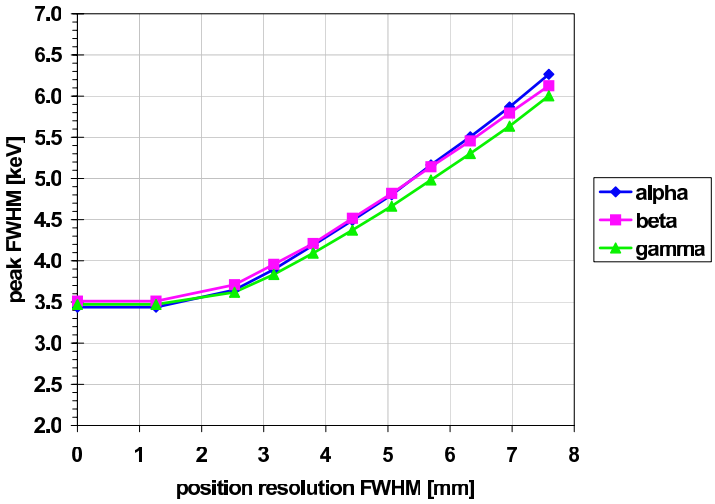

Figure 3.46: Simulated width for the 1382 keV peak of ^{49}Ti as a function of the positional smearing, $FWHM_0$, without conditions on the segment multiplicity. See text for details.

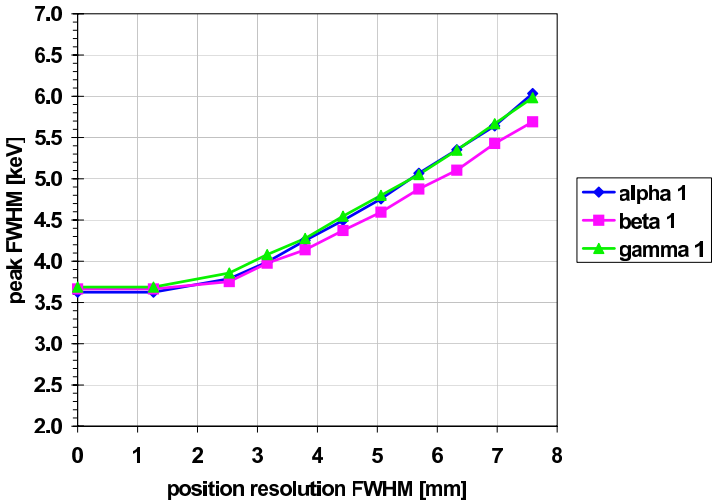

Figure 3.47: Simulated width for the 1382 keV peak of ^{49}Ti as a function of the positional smearing, $FWHM_0$. Only the events with 1 segment firing have been considered. See text for details.

3.7 The grid search PSA algorithm

As discussed in section 2.3, several PSA algorithms have been developed and tested so far within the AGATA collaboration. In the present work, the grid search method [99] by Roberto Venturelli was used, which was originally developed and tested on the experimental data from the MARS in-beam experiment. The original implementation was modified to cope with the new data format and it was further optimised as well.

The algorithm is based on the comparison between measured net and transient signals of the segments and calculated signals from a fine grid of points in the crystal. Although it can assume one or two interaction points per segment, in its simpler implementation the method searches for just one interaction point per firing segment. Using simulated signals, it was proven that, in case of multiple interactions within one segment, the result of this algorithm is indeed a fictitious single interaction point positioned at the centre of gravity of the real interactions. An energy equal to the sum of the individual energy depositions is assigned to such fictitious interaction point. This justifies the approximation considered with the simulated data, namely packing the interaction points within the same segment. The signal comparison is done by evaluating the following figure of merit (F.O.M.):

$$F.O.M. = \sum_{j \in NS} \sum_{i=T_0}^{T_{end}} \mid V_{ij}^{m} - V_{ij}^{c} \mid^{p} \tag{3.8}$$

where V_{ij}^{m} and V_{ij}^{c} are respectively the measured and the calculated signals; the indexes i, j stand respectively for the sampled times and segment index. The first sum runs over the segment surrounding the firing one, the second sum runs over all the sampled points for a particular channel. The exponent p is a positive number. It can be proven that this F.O.M. is a metric for positive values of p. For instance $p = 2$ corresponds to the Euclidean metric. In the present work, $p = 0.3$ was used, as it will be discussed in subsection 3.7.1.

This parameter, as well as other parameters entering the algorithm, has been adjusted in order to minimise the peak FWHM following Doppler correction, using the point position to infer the photon direction, or in other words to produce the best effective energy resolution. For the events where more than one segment was firing, a hit pattern (“neighbouring pattern” in the following) was chosen to avoid the use for a given interaction of the

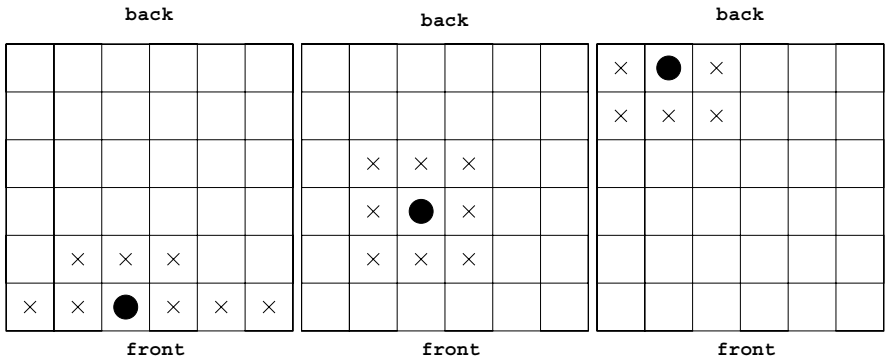

Figure 3.48: Pattern used to define the set of neighbouring segments for events with more than one segment firing. The closed-end shape of the detector is reflected in an extended neighbouring pattern when a frontal segment is hit.

transient signals due mainly to another one. A possible neighbouring segment pattern for multiple interactions is depicted in figure 3.48. This segment pattern is deduced from simple geometrical considerations, however in some cases it is possible to improve the performance by modifying it, as will be discussed later.

In order to deduce the position of an interaction, its full set of neighbouring segments is used, except the segments where another net-charge signal is present. The best performance is obtained using for the F.O.M. calculation also the segments where the transients of two interactions are overlapping, i.e. a further reduction of the set of neighbouring segments worsens the peak width. Anyway, the algorithm allows to search for the interaction points in decreasing order, subtracting at each step the resulting basis signal from the experimental data, in an iterative way. The signal registered from the central contact and from the net-charge segment are not used since it turns out that their inclusion in the F.O.M. calculation results in a worsening of the energy resolution obtained using the hit pattern in figure 3.48. Therefore, 8 transient signals are used on the average.

The comparison of a signal with the basis is done independently of the position of the tested point inside the detector and the result for the matching of a certain point does not depend on the matching of the neighbouring points. Hence the algorithm has no particular requirements about the geometry of the grid of calculated signals, allowing the use of irregularly-

spaced signal basis which can be constructed with a density distribution matching the position sensitivity of the detector [72].

Different versions of the algorithm were developed in order to meet various experimental situations. For example, if enough computing power is available during the analysis, it is possible to allow a time adjustment using as F.O.M.:

$$F.O.M. = \sum_{j \in NS} \sum_{i=T_0}^{T_{end}} \mid V_{i,j}^{m} - V_{i+\Delta i,j}^{c} \mid^{p} \tag{3.9}$$

and searching for the best Δi in some subsampling steps.

Another possibility, if enough computing power is available, is to search for two interactions within the same firing segment. When two points are searched, V_{ij}^{c} is a linear combination of signals for two possible points in the real segment while their amplitudes represent the energy partition between the two deposits. While searching for the position of a single interaction inside a segment is a 3-dimensional problem, the search for two interactions is a 7-dimensional problem: x_1, y_1, z_1, x_2, y_2, z_2 and the energy partition $k = E_1/E_2$ between the two interactions should be estimated. Thus, the algorithm turned out to be significantly slower than the version searching for single interaction points. On the other hand, it turned out that its performance in terms of the resulting Doppler correction is not better than the case where only a single interaction point is searched. Therefore, our results were produced assuming only one interaction per segment.

Finally, it should be pointed out that variants of the algorithm have been implemented in order to speed up the search in case the computing time is an issue, such as in the future on-line implementation. Such variants rely on adaptive methods based on a first rough search, which can be a parametric one or a grid search on a coarsely-spaced grid, followed by a fine search in the region identified by the rough search.

3.7.1 Optimisation of the performance of the algorithm.

In order to optimise the attainable performance, some variants of the algorithm have been taken in consideration and tested on the experimental data. In view of the timing problems presented above and of the low sampling rate (40 MHz) of the digitiser cards, the results obtained have intrinsic

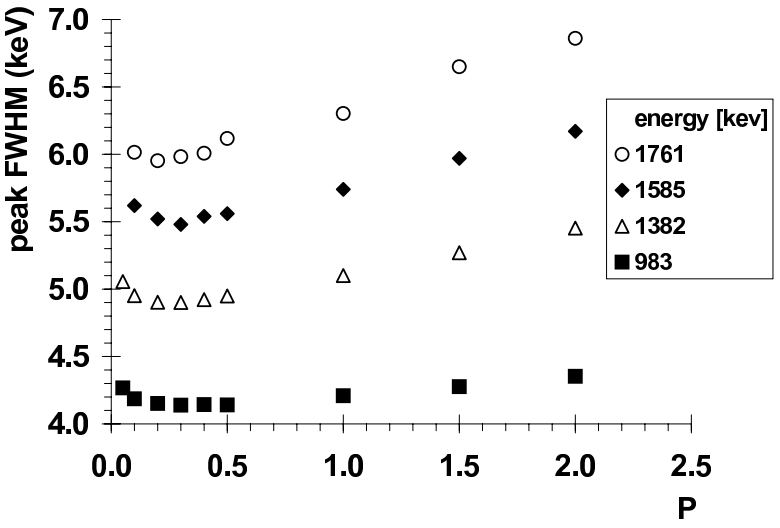

Figure 3.49: Width of 983, 1382 1585 and 1781 keV peaks as a function of the p exponent used in F.O.M. of equation 3.8 [100].

limitations. Hence all the optimisations presented below need to be revised on future datasets with a superior quality.

The basis signals used here and for the rest of the analysis were calculated with the MGS code [67] in points belonging to a cubic lattice having 2 mm step. The used sampling rate of the basis was 5 ns, i.e. the basis had 5 samples for each sampling period of the experimental digitised signal.

The variation of the final peak FWHM as a function of the parameter p of equation 3.8 is shown in figure 3.49 for several intense transitions. It is apparent that the behaviour of the curves does not depend on the energy of the photons. All of the curves show an absolute minimum around $p = 0.3$ which was therefore used in the subsequent analysis.

Another degree of freedom of the algorithm is the choice of the set of neighbouring segments. A systematic study was performed on this subject by using a dataset with selected events where only one segment was firing. The PSA was performed using a number N of segments varying from 1 to 35 (the maximum), choosing on an event-by-event basis the N segments having the largest amplitude of transient signals. The result shown in figure 3.50 suggests that the best performance is obtained when 18-20 neighbouring segments are used. In order to make a comparison with figure 3.48, the found pattern for the neighbouring segments approximately

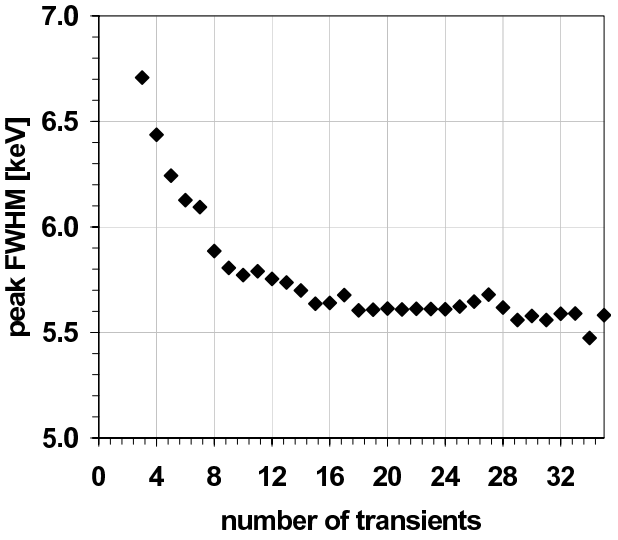

Figure 3.50: Width of the 1586 keV peak in the Doppler-corrected spectrum as a function of the number of segments used by the PSA [100].

corresponds to the map depicted in figure 3.51 where the first and second nearest neighbours are used.

The result of the PSA algorithm is very sensitive to a proper time alignment of the measured signals with respect to the calculated basis. This was proven by changing the time alignment of the experimental data by coher-

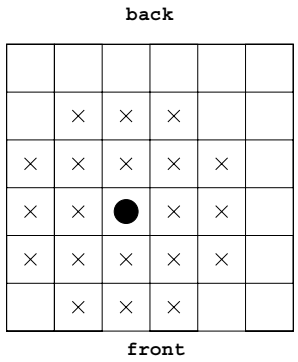

Figure 3.51: Neighbouring segment pattern optimising the results of the grid search algorithm for event with only one segment firing.

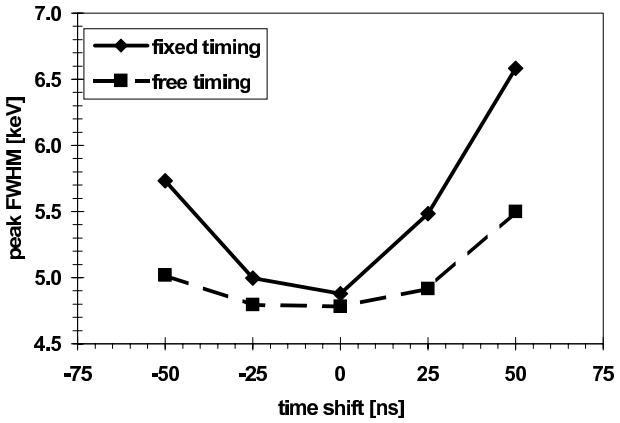

Figure 3.52: Width of the 1382 keV peak as a function of the time-shift of the registered signals with respect to the correct alignment to the signal basis. The 25 ns step corresponds to the sampling period [100]. The continuous line was calculated using the F.O.M. in equation 3.8, while for the dashed line the F.O.M. in equation 3.9 was used. See text for details.

ent shift in time of all the signals in steps of 1 sample point (25 ns). The resulting FWHM for the 1382 keV peak, depicted in figure 3.52 as a function of the shift in time (multiple of the sampling period), is minimum for a zero value of shift and increases rapidly if non-zero shifts are taken into account.

A further test of stability of the algorithm was performed using the more complex F.O.M. of equation 3.9. The experimental data were shifted in time in multiple steps of the sampling period, while the algorithm was allowed to shift the basis in time by sub-sampling steps. It should be reminded that the basis was calculated at 5 ns interval, thus each sampling period corresponds to 5 calculated steps of the basis. For this test, the range of allowed time shifts for the basis was restricted to ± 1 sampling step, corresponding to ± 5 calculated points. The result, reported in the same figure 3.52 as a dashed line, shows that the algorithm is quite robust. In fact, we see that the time shift is always in the correct direction and actually takes up the maximum allowed value. For instance, the resulting peak FWHM in case of +25 ns (free basis) is the same as the value for zero time shift (fixed basis); the peak FWHM for -50 ns time shift (free basis) is the same as -25 ns time

shift (fixed basis).

In order to speed up the search of the position of the interactions, a cleverer algorithm can be implemented. Actually two independent methods have been tested.

The first of these methods uses a search on a coarser grid to find the approximate region of the segment where the interaction happened, followed by another search on a finer grid. While this method is faster, a loss in resolution was experienced since it might happen that the position of the interaction zone (result of the coarse grid search) is mistaken and the further optimisation step leads only to a local minimum.

Another method was developed for the first step of the PSA. The search on the coarse grid can be substituted with an even faster parametric search. A sensitive parameter which was identified is the absolute area of the transients. This parameter can be estimated for the registered waveform and the subsequent grid search can be restricted to the basis point having an absolute area of transients close to the experimental one. This method, applied only for events with multiplicity 1 of segments firing, allowed for a faster search (a factor 4 compared to the previous method) and showed a slight improvement of the resolution of PSA. This result, although at the limit of the statistics, suggests that the chosen parameter has a physical meaning.

3.8 Results

As explained in the previous sections, the position resolution provided by the PSA algorithm can be deduced from the quality of the Doppler correction. The pre-sorted data, corresponding to events with the AGATA triple cluster firing in coincidence with the DSSSD detector, were processed with the grid-search PSA algorithm in order to extract the individual interaction points within the crystal. As mentioned in section 3.7.1, the basis of signals considered for the pulse shape analysis was calculated with the MGS code [67] over a cubic lattice having 2 mm step and 5 ns sampling rate. As discussed in section 3.7, only one interaction point per segment was considered. In case of more segments firing in coincidence, the first interaction point of the photon was assumed to lie within the segment having the largest energy deposition. Doppler correction was performed by inferring the photon direction from the first interaction point and by deducing on an

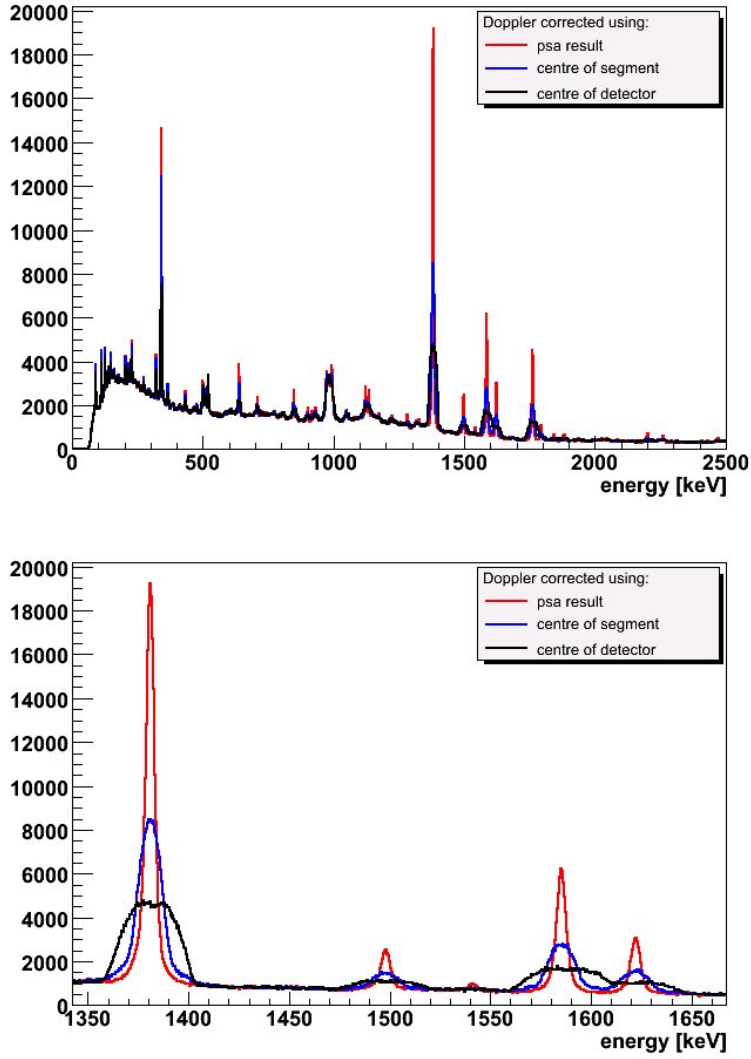

Figure 3.53: Doppler-corrected spectra for the full cluster, deducing the direction of the photon respectively from the centre of the detector, centre of the segment and from the PSA information. All of the segment multiplicities have been considered. The bottom spectrum is obtained by expanding the top spectrum around the energy region of interest.

event-by-event basis the velocity vector of the recoiling nuclei as discussed in section 3.4.

The results of this procedure are shown in figure 3.53, together with the

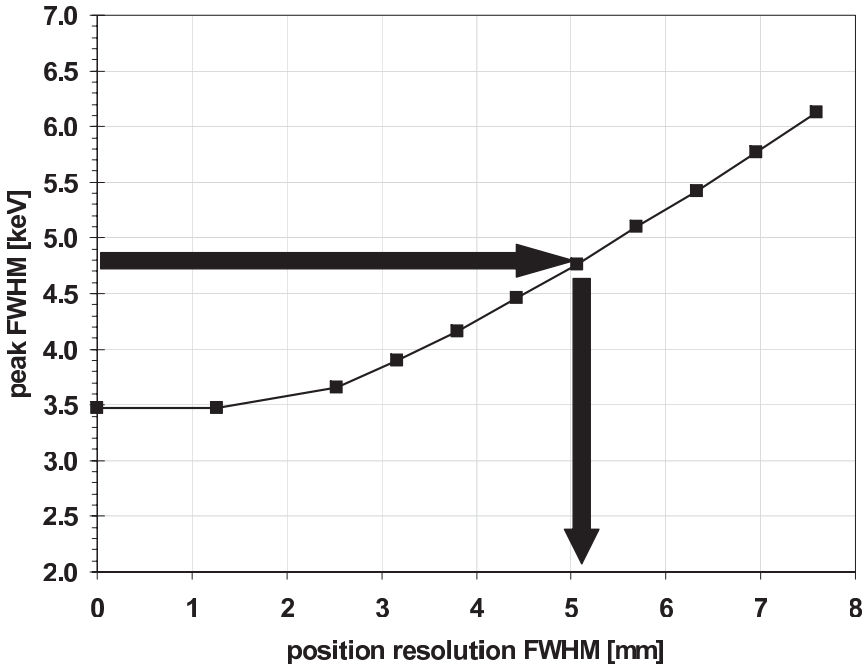

Figure 3.54: Width of the simulated 1382 keV peak as a function of the position smearing for the full triple cluster. Individual crystal energy resolution have been considered. All of the segment multiplicities are taken into account. The horizontal arrow indicates the experimental width.

spectra obtained by Doppler correcting at detector or segment level (equivalently to what was shown with simulated data in figure 2.18). The improvement in quality of the spectra is apparent. For the 1382 keV peak of ^{49}Ti, FWHM=4.8 keV is obtained following the PSA algorithm, which should be compared to 14 keV and 35 keV at segment and detector level respectively.

The resulting position resolution is extracted quantitatively by comparing the experimental peak width to the simulated value using the curves shown in figures 3.46 and 3.47. In this case the simulated data from the three individual crystals were summed up, obtaining the curve plotted in figure 3.54. A contribution of 1 keV was summed quadratically to the simulated peak width in order to cope with the systematic error originating from the imperfect positioning of the triple cluster, discussed in section 3.4.1. The observed peak FWHM=4.8 keV corresponds to a smear-

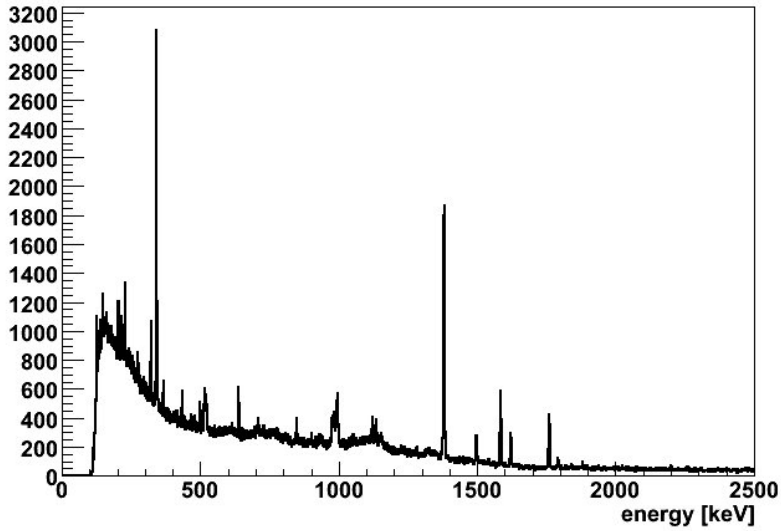

Figure 3.55: Doppler-corrected spectrum for the third detector "γ", deducing the photon direction from the PSA information and considering only segment multiplicity 1.

ing $FWHM_0$=5.1 mm, or equivalently the observed position resolution at 1382 keV is 5.1 mm.

It should be observed that the value deduced in this way is actually an average of position resolution values measured at different energies, since the detected 1382 keV could correspond to a single segment in which 1382 keV are released or to more segments in which the same energy is partitioned, each of them thus having lower energy deposition and worse position resolution. This originates ultimately from signal-to-noise considerations which affect especially the transient signals. Thus, from this point of view, events in which a single segment is firing with a net-charge signal should produce narrower peaks. Furthermore, at segment multiplicity 1 there are no segments in which net-charge and transient signals superimpose, thus resulting in an overall better performance of the PSA algorithm. On the other hand, as discussed in section 2.2, multiple Compton scattering is the most probable interaction process for photon energies around 1 MeV and in this case the PSA algorithm will only provide the centre of gravity of the actual interaction points, which could lie at large distances (of the or-

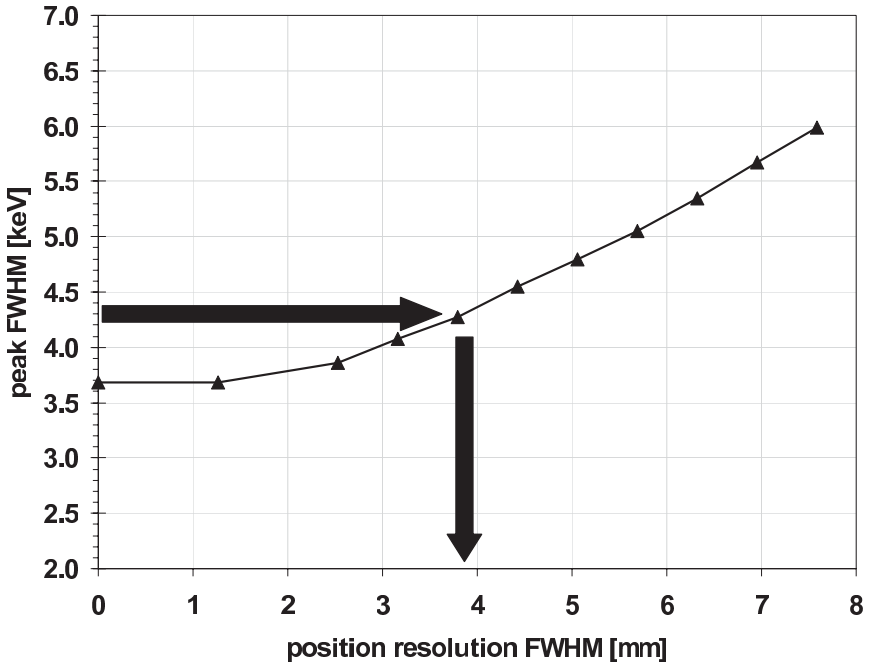

Figure 3.56: Width of the simulated 1382 keV peak as a function of the position smearing for the third detector "γ". Only segment multiplicity 1 is considered. The horizontal arrow indicates the experimental width.

der of 1 cm) from the first interaction point. This added uncertainty in the direction of the photon results in a broadening of the peaks which could partially compensate the improvement in position resolution.

The experimental data have been further analysed by selecting only events with segment multiplicity 1. For instance, the Doppler-corrected spectrum for the third detector "γ" is shown in figure 3.55, where the photon direction was provided by the PSA algorithm. In this case the width for the 1382 keV peak of ^{49}Ti was FWHM=4.3 keV, slightly better than the value obtained for the full cluster without conditions on the segment multiplicity. The comparison of the peak FWHM with the simulated data, shown in figure 3.56, suggests that in this case the position resolution correspond to a smearing $FWHM_0$=3.8 mm, hence better than the value obtained for the full cluster.

It is not easy to attribute an uncertainty to the present estimates of position resolution. Considering the approximations made with the Monte

Carlo simulation, where part of the parameters can only be extracted in a rough way, and the statistical errors, we estimate that the uncertainty on the present measurement of position resolution is of the order of 1 mm.

Other groups within the AGATA collaboration have analysed the same data using different PSA algorithms, which can therefore be compared on the basis of the quality of the resulting Doppler correction. Applying the Matrix method [101] and the MINIBALL algorithm [79] the peak width of the 1382 keV transition is respectively 6.2 and 6.4 keV [102], therefore in both cases the position resolution is poorer than that obtained using the grid search method. The peak width obtained with the Recursive Subtraction method [103] is instead 7.3 keV [104]. In this last case the result should be considered quite a preliminary one since the present version of the algorithm only considers the net-charge signals. A revised version of the algorithm is under development.

3.9 Future outlook

The experience gained with the present work suggests that further in-beam experiments would help to better measure the position resolution and to optimise the PSA algorithms. The main part of the uncertainty on the estimate of the position resolution comes from the difficulty in taking into proper account within the simulation all of the sources of Doppler broadening. Part of the parameters of the simulation has only been roughly estimated and without the possibility of a cross-check.

A different strategy is proposed here for a new in-beam experiment. The goal would be to extract the position resolution directly from the experimental data in a model-independent way. This is possible if the data are acquired with the detector in two positions, the former being the same position used during the test analysed in this work, with the detector at 90° with respect to the beam line and as close as possible to the target, and the latter having the detector placed always at 90° but farther from the target.

In the proposed experiment, the estimate of the position resolution is simple, since the difference in energy resolution between the Doppler-corrected spectra gathered in the two positions is due to only two contributions:

- the solid angle subtended by the PSA voxel (i.e. the angular spread

on the initial direction of the photon corresponding to the position resolution);

- the different counting rate.

The higher counting rate in the detector when it is positioned closer to the target gives a contribution to the peak broadening which can be estimated from a measurement performed with a standard calibration source at different distances from the detector. Once this contribution is subtracted, the remaining difference is due only to the position resolution p, weighted inversely to the distance from the target:

$$\begin{aligned} \Delta E^2_{closer} &= a^2 + k^2 \cdot \left(\frac{p}{d_{closer}}\right)^2 \\ \Delta E^2_{farther} &= a^2 + k^2 \cdot \left(\frac{p}{d_{farther}}\right)^2 \end{aligned} \tag{3.10}$$

As a consequence it is possible to estimate the position resolution:

$$p^2 = \frac{1}{k^2} \cdot (\Delta E^2_{closer} - \Delta E^2_{farther}) \cdot \left(\frac{1}{d^2_{closer}} - \frac{1}{d^2_{farther}}\right)^{-1} \tag{3.11}$$

where $k = E_\gamma \frac{\beta \sin\theta}{\sqrt{1-\beta^2}}$ is a constant accounting for the Doppler broadening formula and a is the width one would have in the case of infinite position resolution.

The strength of the proposed method, relying only on experimentally measured values, should make it possible to perform this test in experimental situations where not all the contribution to the Doppler broadening can be estimated with the required precision, hence removing the need for ancillary detectors to measure the recoil vector velocity. In principle the detector could be placed at only a few centimetres from the target, using the smallest possible reaction chamber (for example just a vacuum tube). This is the best setup to estimate the position resolution. To demonstrate it we calculate the error on the estimation of the position resolution:

$$\begin{aligned} \sigma^2_p &= \frac{1}{k^2} \cdot \left(\frac{2 \cdot \Delta E_{closer}}{\frac{1}{d^2_{closer}} - \frac{1}{d^2_{farther}}}\right)^2 \sigma^2_{\Delta E_{closer}} \\ &+ \frac{1}{k^2} \cdot \left(\frac{2 \cdot \Delta E_{farther}}{\frac{1}{d^2_{closer}} - \frac{1}{d^2_{farther}}}\right)^2 \sigma^2_{\Delta E_{farther}} \end{aligned} \tag{3.12}$$

For $d_{farther}$ big enough we have that $\frac{1}{d^2_{closer}} - \frac{1}{d^2_{farther}} \approx \frac{1}{d^2_{closer}}$, therefore:

$$\sigma_p \approx \frac{2 \cdot d^2_{closer}}{k} \sqrt{\Delta E^2_{closer} \cdot \sigma^2_{\Delta E_{closer}} + \Delta E^2_{farther} \cdot \sigma^2_{\Delta E_{farther}}} \tag{3.13}$$

In the proposed experiment the Doppler broadening is maximum and as a consequence the estimate of the position resolution is the best for the chosen reaction. From equation 3.13 it is possible to formulate a figure of merit useful in optimising an in-beam experiment aiming to measure the position resolution of a photon detector:

$$\begin{aligned} FOM &= \frac{E_\gamma \cdot \beta \sin\theta}{\sqrt{1-\beta^2}} \cdot \\ &\cdot \frac{1}{d^2_{closer} \sqrt{\Delta E^2_{closer} \cdot \sigma^2_{\Delta E_{closer}} + \Delta E^2_{farther} \cdot \sigma^2_{\Delta E_{farther}}}} \end{aligned} \tag{3.14}$$

where an average value for β over the possible scattering angles should be used. The angle between the direction over which the centre of the detector is seen from the target and the direction of the beam-line should be used for θ. The inverse quadratic dependence of the figure of merit on the closer distance where the detector is put is remarkable.

In order to minimise the importance for the Doppler correction of the unknown velocity vector of the recoil emitting the radiation, the preferred reaction mechanism is a fusion reaction with the evaporation of neutron(s). With this mechanism, it is possible to get large cross sections. Since the evaporation of neutrons happens, on the average, at smaller energy with respect to the evaporation of light charged particles (as a consequence of the Coulomb barrier), this causes a smaller dispersion of the recoils in velocity module and direction.

The choice of the reaction channel is very important since no ancillary detectors are planned to be used. For example, there will be no possibility to request conditions on the particle spectra to identify and select a particular reaction channel as it was done for the experiment analysed in this work. By choosing a light neutron-rich target such as ^{7}Li or ^{9}Be and a beam energy slightly above the Coulomb barrier for such targets, the beam energy will be below barrier for the possible (heavier) contaminants, e.g. ^{12}C or ^{16}O, thus strongly hindering any contaminant reaction. Unfortunately, metallic lithium is highly reactive with oxygen, while beryllium oxide is toxic, posing severe health hazard problems for the production of the target. For

these reasons, ^{7}Li of ^{9}Be are seldom used as a target material. Since in the proposed experiment it will be important to have "simple" experimental conditions, it is preferable to evaluate reactions on other light nuclei. A good choice could be a ^{12}C target, which does not need any passive backing, which would bring angular dispersion in the produced recoils, and, given its chemical nature, it is not exposed to contamination. The reactions on ^{7}Li or ^{9}Be will anyway be evaluated as a reference.

Since the F.O.M. in equation 3.14 depends on the energy of the detected photon, another requirement to optimise the reaction is to have a transition to the ground state through a high-energy γ-ray. The cross sections for the population of nuclei with a first excited state above 1 MeV, which can be produced in fusion-evaporation with neutron evaporation on ^{7}Li, ^{9}Be or ^{12}C targets, have been calculated using the PACE code [95]. Some of the resulting reactions are:

- ^{82}Se @ 220 MeV + ^{9}Be $\rightarrow$ ^{88}Sr (350 mb)
- ^{86}Sr @ 250 MeV + ^{9}Be $\rightarrow$ ^{92}Mo (200 mb)
- ^{104}Pd@ 350 MeV + ^{9}Be $\rightarrow$ ^{110}Sn (160 mb)
- ^{106}Pd@ 350 MeV + ^{9}Be $\rightarrow$ ^{112}Sn (210 mb)
- ^{85}Rb @ 240 MeV + ^{7}Li $\rightarrow$ ^{90}Zr (90 mb)
- ^{107}Ag@ 360 MeV + ^{7}Li $\rightarrow$ ^{112}Sn (120 mb)
- ^{104}Ru@ 450 MeV + ^{12}C $\rightarrow$ ^{112}Sn (300 mb)
- ^{134}Xe@ 600 MeV + ^{12}C $\rightarrow$ ^{142}Nd (390 mb)
- ^{135}Ba@ 560 MeV + ^{12}C $\rightarrow$ ^{144}Sm (180 mb)

According to PACE, all of these reactions have a cross section for the nucleus of interest, reported in the list above, between 100 and 400 mbarn, with a branching ratio larger than 30% of the total cross section.

A key parameter in evaluating such reactions is the angular dispersion of the recoils, which depends on the number and energy spectrum of the evaporated neutrons. The smallest angular dispersion for the reactions on ^{12}C is reached by producing ^{142}Nd and ^{112}Sn, with values of 0.5° and 0.6° respectively.

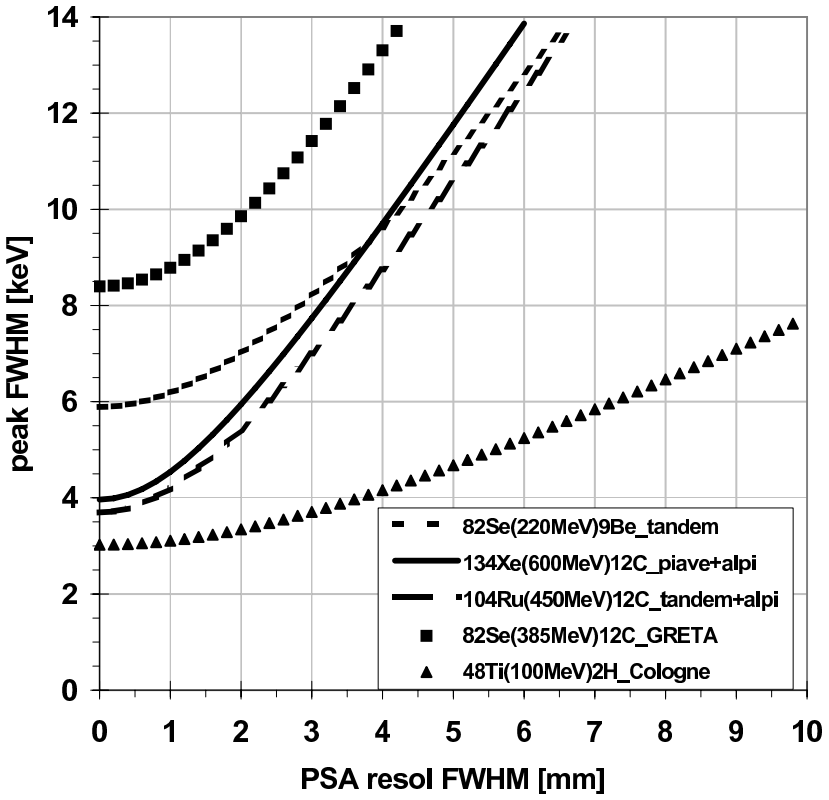

Figure 3.57: Expected peak width as a function of the position resolution for three possible reactions. For comparison the equivalent curves for the in-beam tests performed by the AGATA and the GRETA collaboration are also reported.

The plot of figure 3.57 compares the expected peak widths, calculated through schematic arguments such as those presented in section 3.2, for the three reactions with the best sensitivity to position resolution that are presently feasible using the accelerators available at the Laboratori Nazionali di Legnaro. The curves corresponding to the in-beam tests performed with the AGATA (present work) and GRETA [82] detectors are shown for reference. The expected gain in sensitivity with respect to the Cologne experiment as a consequence of the bigger slope of the curve is evident. On the other hand, with the reactions proposed in the present section the situation will be more favourable than the experiment performed by the GRETA collaboration, where the the energy resolution is poor even in case of perfect position resolution [105].

Chapter 4

Estimation of the position resolution through Compton imaging techniques

In several fields, ranging from X- and γ-ray astronomy to medical applications, it is fundamental to form images using high-energy electromagnetic radiation. Unfortunately, given the extremely short wavelength of the radiation, it is not possible to create a γ-ray image using "conventional" optics (based on reflection or refraction) and new techniques had to be developed to this purpose.

In most medical imaging applications, a conventional gamma camera (Anger camera) [106] or a Single-Photon Emission Computerized Tomography (SPECT) [107] are used. These devices rely on multi-hole collimators which allow only photons from a well-defined direction to enter the detection system. The drawback of these methods is the limited efficiency, due both to the collimator and to self-absorption inside the object under study (patient). As a matter of fact, the typical isotopes used for medical applications have short lifetimes and emit low-energy γ-rays. This ultimately results in high doses for the patient, which could be reduced by removing the collimation system.

An alternative solution is the Compton imaging [108, 109]. Thanks to the use of position-sensitive photon detectors, the collimator can be removed and the physical properties of the interactions between γ-rays and matter are used to reconstruct the path of individual photons from the

source. This procedure is similar to the problem of γ-ray tracking outlined in chapter 2 and actually it represents kind of an "inverse problem". With γ-ray tracking techniques, clusters of interaction points are validated and re-ordered according to their scattering sequence, assuming a given origin for the photons. The result of such a procedure is the photon energy. In Compton imaging, the energy of the photons is assumed to be known and the location of the source is gathered from clusters of interaction points through knowledge of the Compton scattering mechanism.

As discussed in section 2.2, the efficiency of a tracking algorithm depends critically on the measured precision of the individual photon interaction points, i.e. on the position resolution. Hence, it is reasonable to assume that the quality of the image reconstruction through Compton scattering can provide valuable information on the position resolution. For this reason, we have decided to perform some experimental tests with a prototype detector of AGATA in order to evaluate the attained position resolution from the quality of the image reconstruction. Although segmented coaxial germanium detectors are not typically used in imaging applications [107], this could open up interesting technological and interdisciplinary developments.

In this chapter, the principles of Compton imaging will be briefly reviewed and the preliminary tests performed with the AGATA detector will be described.

4.1 Principles of Compton imaging

If photon detectors sensitive to the position of the individual interactions are available, some information on the position of the source emitting the radiation can be gathered by selecting the events in which the first interaction point corresponds to a Compton scattering. The scattering angle can be estimated from the Compton formula 2.4, obtaining:

$$\cos\theta = 1 - \frac{m_e c^2 \cdot E_C}{E_\gamma \cdot (E_\gamma - E_C)} = 1 + \frac{m_e c^2}{E_\gamma} - \frac{m_e c^2}{E'_\gamma} \tag{4.1}$$

where E_γ is the *known* incident photon energy and $E_C = E_\gamma - E'_\gamma$ is the energy deposited in the interaction. Therefore, two interaction points, the first one of them corresponding to a Compton scattering, define a cone in the 3-dimensional space. As sketched in figure 4.1, the axis of the cone

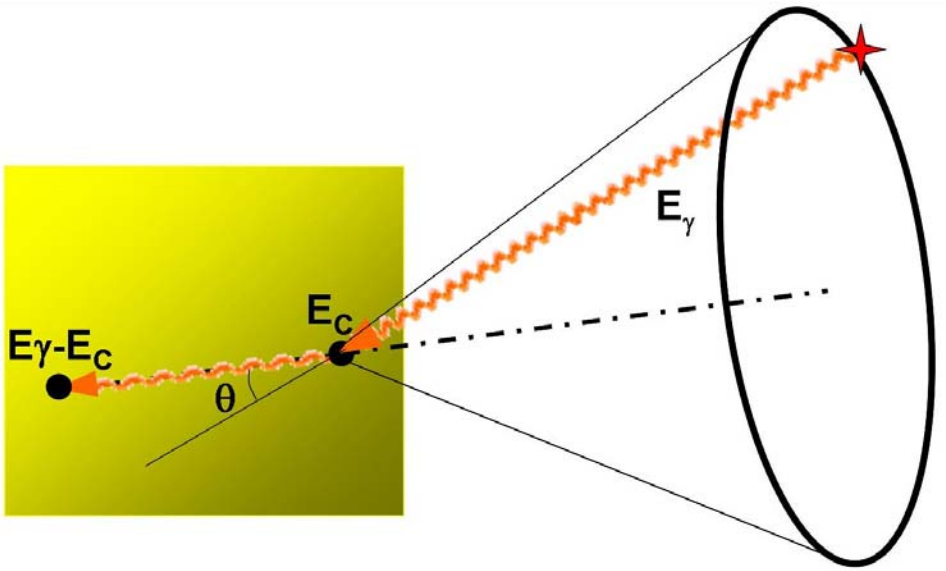

Figure 4.1: The possible positions of the source of radiation, determined by a Compton scattering sequence, are distributed on a conical surface in 3-dimensional space.

is the line passing through both interaction points and the opening angle of the cone is the scattering angle. It is obvious that, in case of a *single* event, the position of the source of radiation remains totally undetermined

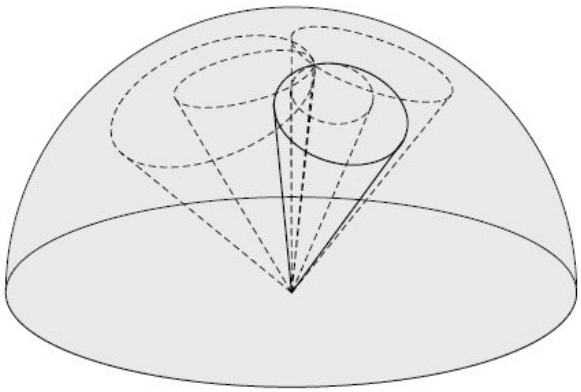

Figure 4.2: If the radioactive source is positioned far from the detector the intersection of back-projection cones reduces to the intersection of circles on a spherical surface.

alongside the direction of the cone. If more scattering events from the same source are observed, each of them will determine a different cone. All of these *back-projection* cones should overlap in a single point corresponding to the source of the radiation. In principle, three cones should be sufficient to determine the common origin of the radiation, but in practice much higher statistics is needed because of the finite precision on energy and position of each interaction point, resulting in errors in the determination of axis and opening angle of each cone.

In particular cases, the problem can be simplified depending on the (approximate) information available for the position of the source. For instance, if the source lies at a large distance from the detector (relative to the detector size), the problem can be reduced to that of forming a 2-dimensional image on the surface of a sphere. In this case, as depicted in figure 4.2, in order to find the position of the source it is sufficient to intersect circles on the spherical surface, rather than intersecting cones in the 3-dimensional space, and the direction of the photons is typically expressed in term of polar coordinates (θ, ϕ).

4.1.1 Sources of error in Compton imaging

As mentioned above, the position of a radioactive source with Compton imaging techniques could in principle be determined by measuring three Compton scattering events. In practice, all of the quantities entering equation 4.1 are affected by experimental errors propagating to the determination of axis and opening angle of each cone. Hence, in order to determine with precision the source position, a large number of cones (events) should be measured.

Three main sources of error should be considered, namely:

- the finite energy resolution of the detector;
- the Doppler broadening due to the non-zero momentum of the electron on which the photon scatters;
- the finite position resolution of the detector.

The first two error sources affect the determination of the opening angle of the cone, while the third one affects the determination of the axis of the cone. These sources of error will be discussed in more detail in the following.

In Compton imaging, as mentioned previously, the photon energy E_γ is assumed to be known, thus the only parameter in equation 4.1 which is affected by the finite energy resolution of the detector is the energy deposition E_C, or equivalently the energy of the photon after scattering $E'_\gamma = E_\gamma - E_C$. The error propagation gives:

$$\delta(\cos\theta)_E = \frac{m_e c^2}{E'^2_\gamma}\delta E'_\gamma \tag{4.2}$$

It should be observed that actually two independent estimates of E_C are available, the former being the direct measurement, the latter being the difference of the incident photon energy and of the energy depositions in the subsequent interaction points. It is therefore possible to improve the precision on E_C through a weighted average.

The Compton scattering formula 2.4 is derived under the assumption of free electron at rest. In practice, electrons in the detector material are bound and have a finite momentum $\mathbf{p}$, the distribution of which is known as the *Compton profile*. Considering this effect, the energy transferred to the electron by the incident photon is given by:

$$E_e = \frac{|\mathbf{k}|^2}{2m_e} + \frac{\mathbf{k}\cdot\mathbf{p}}{m_e} \tag{4.3}$$

where the scattering vector $\mathbf{k} = \mathbf{k_1} - \mathbf{k_0}$ is the momentum difference between the scattered and incident photons. The first term on the right-hand side of equation 4.3 is the same as given by the Compton scattering formula 2.4. The second term is the contribution of the finite momentum of the electron, which is linear in p_z (projection of the initial momentum of the electron on its final direction) and increases with the incident photon energy. Since the electrons have a finite momentum distribution, the energy of the scattered electrons will depend not only on the scattering angle, but on the initial momentum as well, resulting in an error in the determination of the photon scattering angle if the standard Compton scattering formula is used. More details on this effect can be found, for instance, in ref. [110], where it is shown that the effect of the Compton profile can be larger than the effect of the finite energy resolution of the detector.

The final source of error in the determination of the origin of the photons is the finite position resolution of the detector(s), affecting the determination of the direction of the axis of the back-projection cone. Assuming position resolutions δr_1, δr_2 respectively for the first and second interaction

points, lying at a distance $r_{1,2}$ from each other, the resulting error in the cone axis direction, or equivalently in the scattering angle, is given by:

$$\delta\theta_p \approx \frac{\sqrt{\delta r_1^2 + \delta r_2^2}}{r_{1,2}} \tag{4.4}$$

This formula is valid in the approximation that $\delta r \ll r_{1,2} \cdot \sin(\theta)$. It should be reminded that in principle δr_1 and δr_2 depend on the specific energy depositions.

The importance of the various causes of error in the determination of

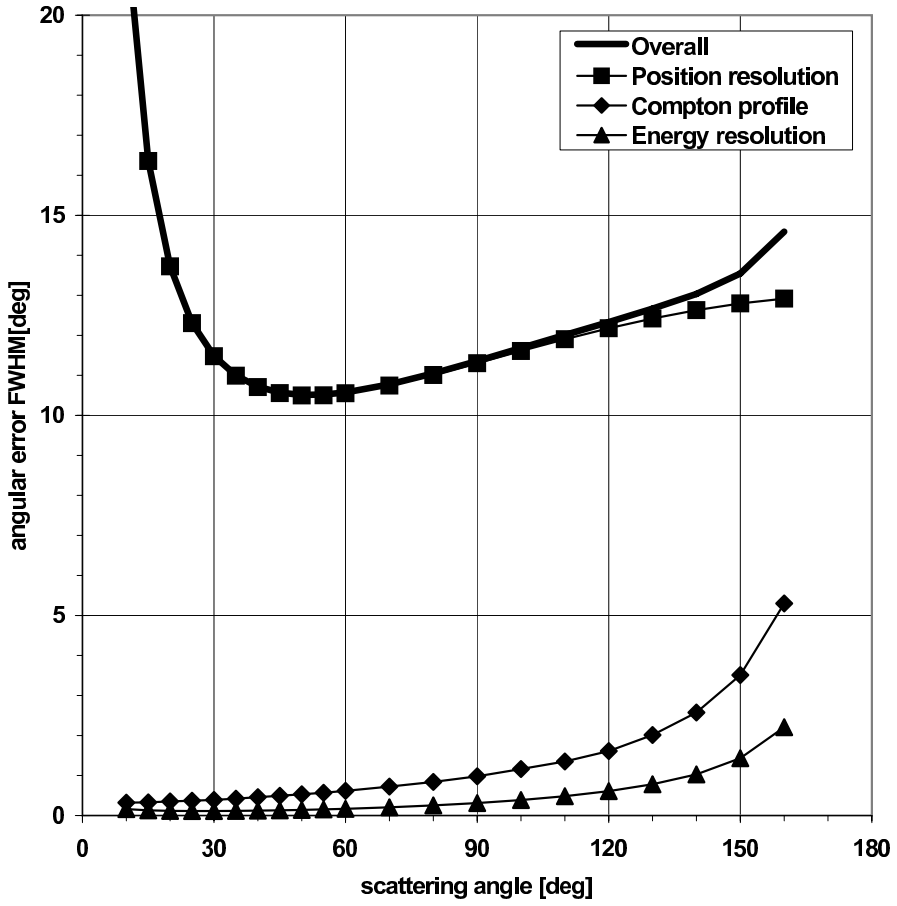

Figure 4.3: Impact of the different contributions to the angular uncertainty in Compton imaging using a segmented germanium detector. A γ-ray with energy of 1332 keV is assumed.

the position of the source is exemplified by the plot of figure 4.3, where gammas of 1332 keV in a germanium detector have been considered. In the calculation, the distance between the interaction points has been taken as 4 cm. The intrinsic energy resolution of the detector has been modelled, as usual, as $FWHM = \sqrt{a + b \cdot E}$, assuming respectively 1.0 keV and 2.3 keV at photon energies 122 keV and 1332 keV. An energy-dependent position resolution was considered, producing 5 mm FWHM for 1332 keV photons. The contribution of the Compton profile was taken from ref. [110]. It is apparent that the contribution due to the finite position resolution of the detector dominates on the other sources of error, being approximately an order of magnitude larger. This indeed suggests that the position resolution of a pulse shape algorithm on a segmented germanium detector, such as one of the prototype detectors of AGATA, can be inferred from the quality of a Compton-reconstructed image. Such a test could fruitfully complement the in-beam test performed at Cologne and it was actually carried out with prototype detector S#001 at the Laboratori Nazionali di Legnaro. In the following, the preliminary results from such a test will be presented.

4.2 Test of the imaging capabilities of the AGATA detector

As discussed in section 4.1.1, the main contribution to the angular uncertainty in Compton imaging comes from the finite position resolution of the detector. Hence, if the single interaction points are determined through a pulse shape analysis algorithm, the imaging capability of the detector can be exploited to evaluate the quality of the pulse shape analysis itself.

The imaging capabilities of the AGATA prototype detector S#001 were evaluated through a test performed at the Laboratori Nazionali di Legnaro using a ^{60}Co radioactive source positioned at 1 m from the crystal. The experimental setup is shown in figure 4.4. The signals from the germanium detector (36 segments + central contact) were digitised and acquired using ten N1728A cards [111] with a differential input manufactured by Caen, which are shown in the inset of figure 4.4 together with some modules used to generate the local trigger. These cards use 14 bits fast-ADCs with 100 MHz sampling frequency and calculate directly the amplitude (energy) of the input signal through a moving window deconvolution algorithm [86]

Figure 4.4: Photo of the experimental setup used during the imaging run. The ^{60}Co source is positioned at the lower left corner of the picture. The inset shows a detail of the N1728A digitisers and of the trigger electronics.

running on the on-board FPGA. A common clock was distributed in daisy chain to all of the cards, while the trigger signal, which was generated by a leading edge discriminator sensing the central contact of the AGATA detector, was distributed through a star connection. Each card was read independently by the other ones, the full event being reconstructed off-line by exploiting the time stamp information. The data rate was kept to an acceptable amount by reading out for each channel only the first 200 samples and the energy value calculated internally.

4.2.1 Presort

In the preliminary part of the analysis, the data from the AGATA detector were calibrated in energy. In order to simplify the analysis, it was decided to form the images only by using events in which two segments were firing in coincidence, each of them with a net charge signal.

As discussed in chapter 3, a proper time alignment of the signals is essential in order to perform a meaningful comparison with the signals of the reference basis. A preliminary inspection of the digitised data showed

that the delay between the trigger signal and the first acquired sample was depending on the specific electronics channel. However, thanks to the distributed clock signal, it was possible to verify that such delay was constant in time along the acquisition run and therefore it was possible to perform a proper time alignment. To this purpose, a reference signal with equivalent amplitude of about 4 MeV was injected into the system using the built-in pulser of the core preamplifier at a frequency of 100 Hz. As mentioned in section 2.6.1, this induces a signal in each of the segment preamplifiers, with equivalent amplitude $\sim$100 keV. The pulser data were identified as the events in which the 36 segments fire in coincidence. In fact, such a high segment multiplicity is extremely unlikely for a "real" photon-induced event. The constant delay characteristic of each of the 37 channels was extracted from the pulser data by using the digital CFD algorithm described in section 3.4.1.

It should be observed that the response of the dCFD algorithm depends on the shape of the signal. In particular, given the different bandwidth of the core and of the segment preamplifiers, a constant delay is expected between the segment and the core signals, which can be measured and corrected for. Knowing the delay of each channel relative to the core, the timing information provided by the core was sufficient to determine the timing for each segment and to align the segment signals with respect to the basis for the subsequent pulse shape analysis.

4.2.2 Pulse Shape Analysis

The individual interaction points were extracted using the grid search PSA algorithm described in section 3.7. Also with the "imaging" data set only one interaction point per segment was considered and a basis obtained with the MGS code was used, calculated at 2 ns intervals on a cubic lattice having 2 mm step. It should be remarked that in principle the orientation of the crystallographic axis and the preamplifier bandwidth should be taken into account by the PSA algorithm, as well as the possibility to search for a better timing in sub-sampling steps, as explained in section 3.7. These effects have not been considered in the present preliminary work and they are left for future optimisations.

4.2.3 Reconstruction of the scattering sequence

In order to calculate the back-projection cone starting from two interaction points, their time sequence must be established. Although in principle this would require quite a complex tracking procedure such as the one outlined in section 2.2, in this case it was decided to rely on a simpler "probabilistic" method, based on the empirical observation that the first interaction point corresponds with the highest probability to the largest energy deposition, which has been verified through detailed Monte Carlo simulations. This is not physically possible in case of scattering at small angles, resulting in energy depositions lower than the limiting value E_b calculated for a $180°$ scattering:

$$E_b = \frac{E_\gamma}{1 + \frac{2E_\gamma}{m_e c^2}} \tag{4.5}$$

Therefore, events in which one of the depositions was lower than than E_b were ordered assuming that the first one was the interaction with the lower energy deposit.

4.3 Image reconstruction and comparison with Monte Carlo simulations

During the imaging run, the radioactive source was positioned at 1 m from the detector so that the problem of imaging could be reduced to the problem of forming an image on a spherical surface centred on the detector itself. As mentioned previously, a point on such a surface is defined through two angular coordinates (θ, ϕ).

Although sophisticated and efficient imaging algorithms have been developed for several applications [47], in the present work a very simple approach was used. As explained in section 4.1, fixing the energy of the photons, the back-projection cone is defined through its axis **a**, namely the vector going from the second to the first interaction point, and its opening angle α; its intersection with the spherical surface is a circle. Our simple algorithm divides the spherical surface into pixels corresponding to discrete values of θ and ϕ. In the present work, a $0.5°$ step was chosen for both θ and ϕ. Once a pixel intersected by the back-projection circle is found, as it is sketched in figure 4.5, the algorithm checks which of the neighbouring pixels is intersected by the same circle, working recursively until the full circle

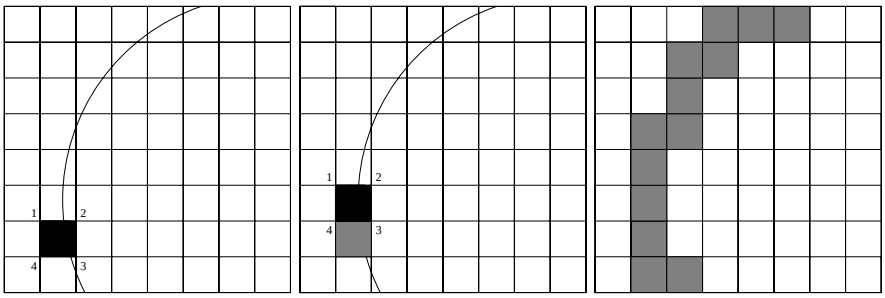

Figure 4.5: Schematic procedure for the reconstruction of the back-projection circle followed by the algorithm used in the present work. First a pixel intersected by the back-projection circle is found (left); a neighbouring pixel intersected by the same pixel is looked for (middle); the full circle is covered working recursively by neighbouring relationships.

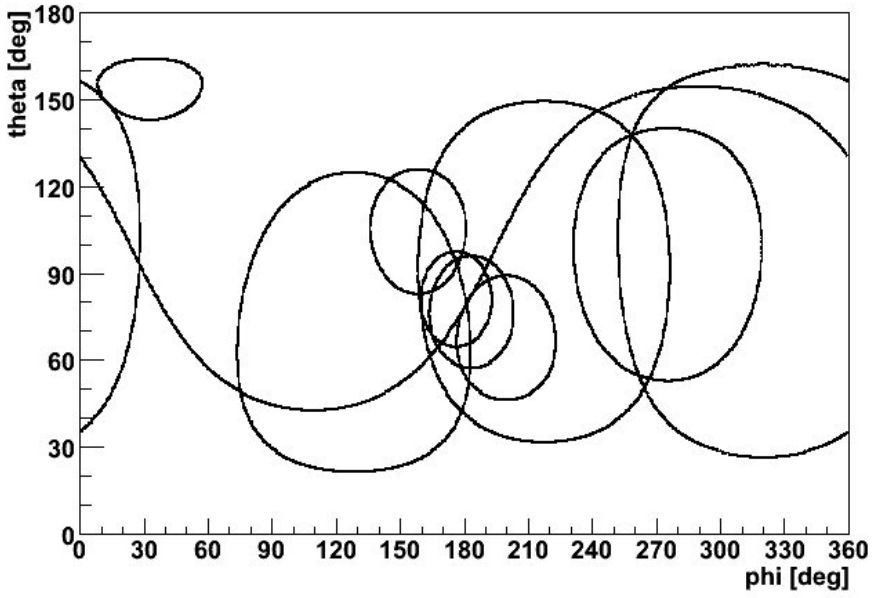

Figure 4.6: Image reconstructed by back-projecting 10 cones. Almost all of the circles, deformed as a consequence of the particular representation of the sphere, pass in proximity of the point with coordinates ($\theta = 180°$, $\phi = 90°$) where the source is located.

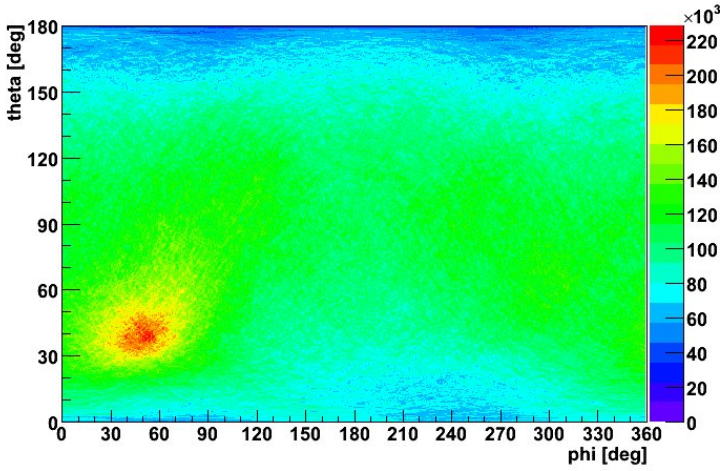

Figure 4.7: Image reconstructed with a simple back-projection of 47000 photons having 1332 keV energy.

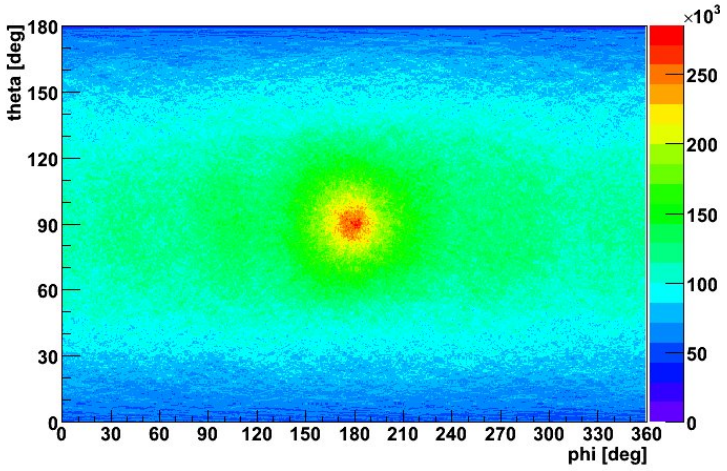

Figure 4.8: Same image as figure 4.7, reconstructed with a simple back-projection of 47000 photons having 1332 keV energy. A rotation of the reference frame has been applied in order to position the spot corresponding to the source as close as possible to $\theta = 90°$, $\phi = 180°$.

is covered. The final image is formed as the superposition of the individual back-projection circles, as shown for instance in figure 4.6 where 10 circles are drawn.

As an example, a high-statistics image is shown in figure 4.7. It should be observed that the (θ, ϕ) representation used here does not conserve areas and therefore distorts the image towards the "poles" (corresponding to $\theta = 0^\circ$ and $\theta = 180^\circ$). Therefore, it is convenient, once the approximate direction of the source is found, to rotate the reference frame so that the source is approximately positioned at $\theta = 90^\circ$, $\phi = 180^\circ$, where the geometrical distortion is minimal. The results shown in the rest of the chapter refer to the 1332 keV line of the ^{60}Co source rotated to the centre of the figure. For convenience, all the images have been normalised in order to have the same area.

The image of figure 4.8 was constructed with a simple back-projection of 47000 photons, with the technique outlined above. Although a brighter spot, corresponding to the source position, can be identified, the quality of the image is not good because of a diffused background with little dependence on θ and ϕ. It should be reminded that the performance of the PSA algorithm used here is degraded in case of interactions happening in neighbouring segments because of the overlap of the transient signals. On the other hand, in case of neighbouring segments the distance between the interaction points is small. Both factors induce a large uncertainty in the determination of the back-projection circles, resulting in a poor quality image.

The situation improves considerably by disregarding events where the interactions take place in neighbouring segments, defined through the pattern of figure 3.48. Furthermore, since the performance of the PSA algorithms is expected to depend on the amplitude of the signals, events in which one of the energy depositions was lower than 25% of the full energy of the photon were disregarded. By posing these more restrictive conditions, only 8000 photons remain, giving the matrix of figure 4.9 which has a smaller background and as a consequence a brighter and better defined spot size.

It should be pointed out that the circumference of the back-projection circles varies depending on the opening angle, which could induce distortions in the resulting image. This effect could be corrected for by weighting each back-projection circle according to the inverse of its circumference.

In addition, an angular error can be associated to each back-projection circle, as explained in section 4.1.1, mainly on the basis of the distance between the interaction points. The angular error could be used to further

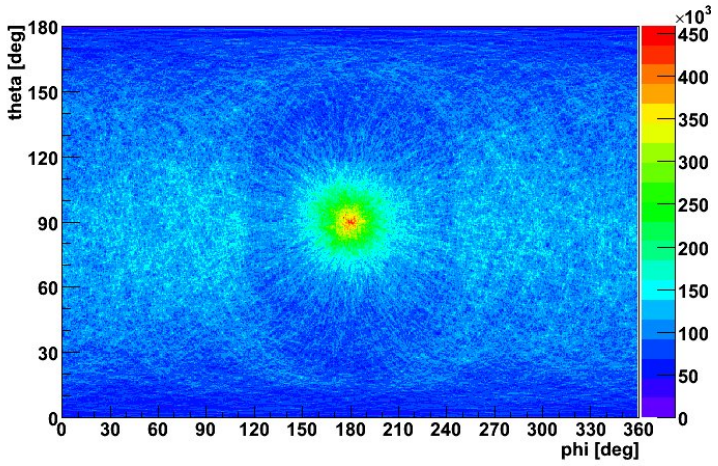

Figure 4.9: Image reconstructed with the back-projection of the same events as figure 4.8, disregarding events in which neighbouring segments were firing or events in which one of the energy depositions were lower than 25% of the full photon energy. Only 8000 out of 47000 events match the more restrictive conditions. A rotation of the reference frame has been applied in order to position the spot corresponding to the source as close as possible to $\theta = 90°$, $\phi = 180°$.

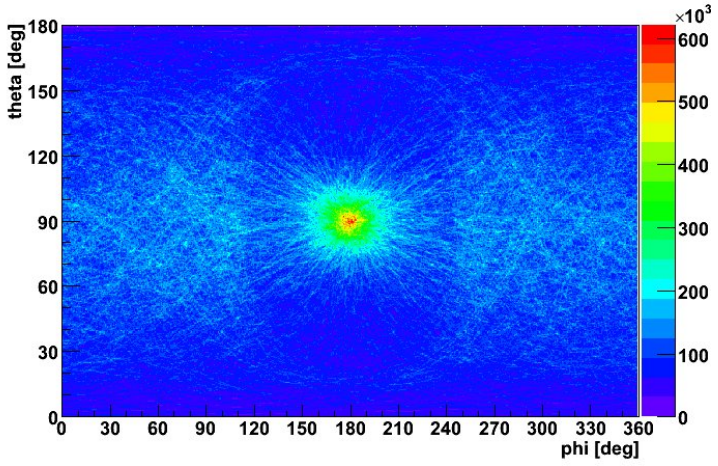

Figure 4.10: Same image as figure 4.9, in which each back-projection circle has been weighted according to the inverse of its circumference and to the angular error calculated as in section 4.1.1.

weigh the back-projection circles.

The result, considering both weights defined above, is shown in figure 4.10, which also corresponds to the back-projection of 8000 photons.

In order to compare quantitatively the quality of figure 4.9 and 4.10,

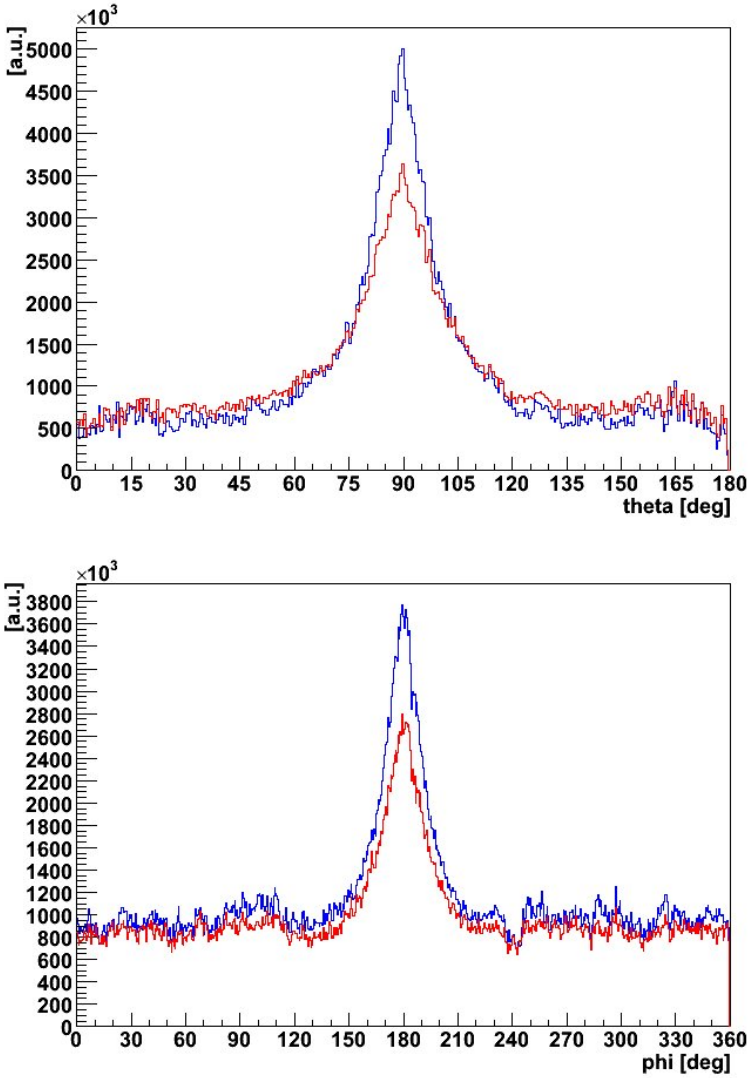

Figure 4.11: Projection of the matrices of figures 4.9 and 4.10 on the θ axis (top) and on the ϕ axis (bottom). The red line corresponds to figure 4.9, in which no weighting functions were considered, while the blue line corresponds to figure 4.10.

a possibility is to project the (θ, ϕ) on the two axes, obtaining a mono-dimensional spectrum with a peak, whose width can be estimated with standard techniques. The spectra obtained by projecting figures 4.9 and 4.10 on the θ axis (with a narrow gate on ϕ) are shown in figure 4.11 (top). The peak FWHM without taking into account the weighting functions is $20.5°$, which should be compared with $17.0°$ when the weighting functions are considered. The corresponding values for the projection on the ϕ axis (with a narrow gate on θ), shown in figure 4.11 (bottom), are $25.0°$ and $22.5°$ respectively.

The procedure used to extract the position resolution from the imaging dataset is similar to the one followed with the in-beam data, described in chapter 3, namely such value is deduced through a comparison between the experimental data and a detailed Monte Carlo simulation taking into account the relevant effects. The same Monte Carlo code described in sec-

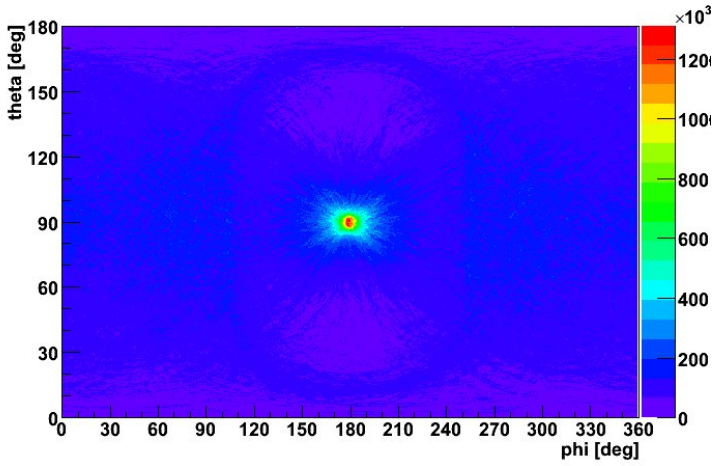

Figure 4.12: Image reconstructed from the dataset of simulated 1332 keV photons, disregarding events where neighbouring segments were firing or events in which one of the energy depositions is lower than 25% of the full energy, and weighting each back-projection circle according to the inverse of its circumference and to the angular error calculated as in section 4.1.1. A rotation of the reference frame has been applied in order to position the spot corresponding to the source at $\theta = 90°$, $\phi = 180°$. Energy and position of each interaction point are known with infinite precision.

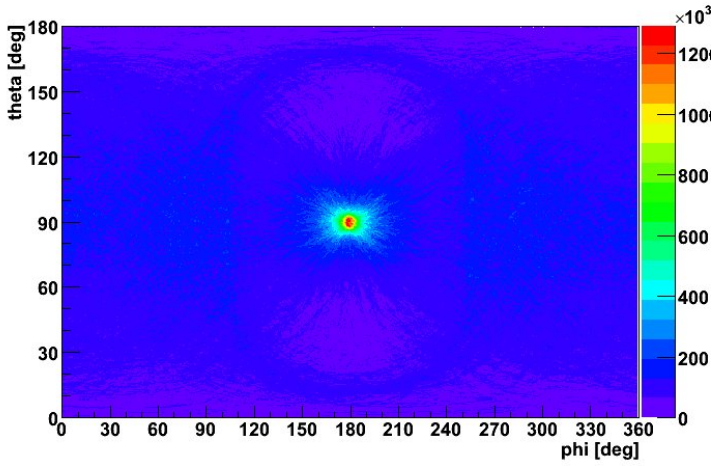

Figure 4.13: Image reconstructed with the same simulated data and the same conditions as in figure 4.12. In this case, a finite energy resolution consistent with the experimental data has been considered, while the position of each interaction point is taken with infinite precision.

tion 3.6 was used, implementing the description of the geometry of the single symmetrical detector. Monochromatic photons having 1332 keV energy were used from a point source positioned at 1 m from the centre of the crystal. The simulated data were converted into the same format of the experimental imaging dataset and they were analysed consistently with the same algorithm and event selections as the experimental data.

As remarked in section 3.6, the simulated data are produced with infinite precision both in energy and position. The image shown in figure 4.12 has been produced by analysing the direct output of the simulation after packing the interaction points within each segment into their centre-of-mass position. The same conditions as in figure 4.10 were requested, namely by disregarding events in which the interactions happen in neighbouring segments or in which one of the energy depositions is lower than 25% of the full energy, and weighting each event according to the angular uncertainty and to the inverse of the circumference of the back-projection circle. The image shown in figure 4.13 has been obtained from the same simulated dataset adding a smearing in energy consistent with the experimental energy resolution of the detector. Visually, the quality of the image is not degraded significantly with respect to the image of figure 4.12. If an

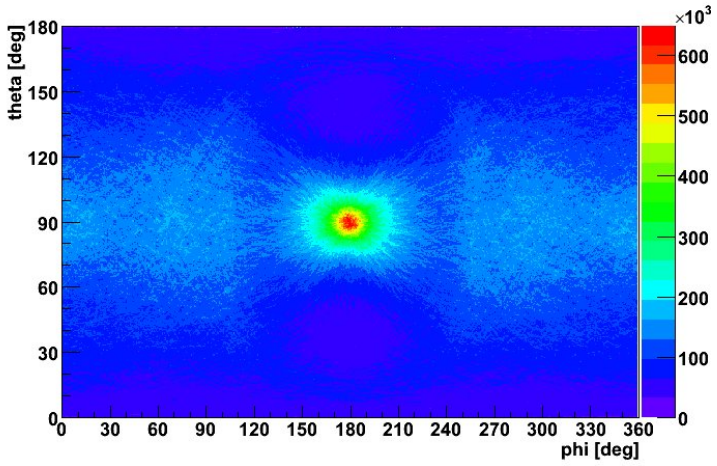

Figure 4.14: Image reconstructed with the same simulated data and the same conditions as in figure 4.12. In this case, finite resolutions consistent with the experimental data have been considered both for energy and position of the interaction points.

additional smearing in position is added, the image shown in figure 4.14 is obtained, for which a 5 mm FWHM position resolution was taken. In this case, the quality of the image is significantly lower than figure 4.12, confirming that indeed the positional error is the dominating factor in determining the quality of the image.

Several images were constructed imposing the same conditions as figure 4.14, each of them corresponding to a different value of position resolution. The quality of each image was estimated by determining the peak FWHM of the spectrum obtained projecting the matrices on the θ axis after a narrow gate on ϕ was put. The dependence of the peak FWHM on the position resolution is shown in figure 4.15. The experimental peak $\mathrm{FWHM} = 17.0^{\circ}$ corresponds to a position resolution of 5.4 mm. Considering instead narrow gates on θ and projecting the matrices on the ϕ axis, the plot of figure 4.16 is obtained, from which a position resolution of 4.7 mm can be extracted.

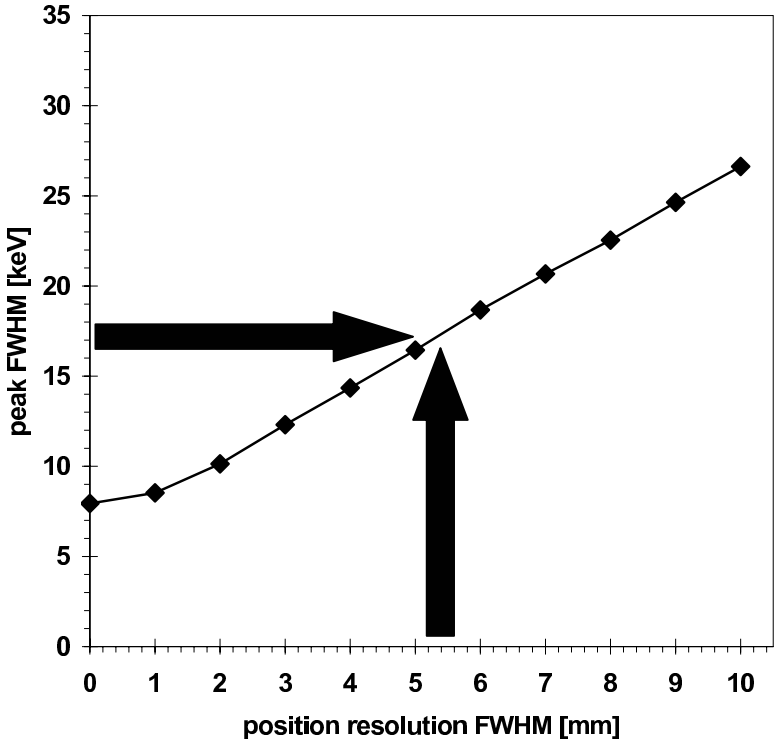

Figure 4.15: Simulated peak FWHM of the distribution in θ of the Compton reconstructed images as a function of the position resolution of the detector. The horizontal arrow indicates the experimental width. See text for details.

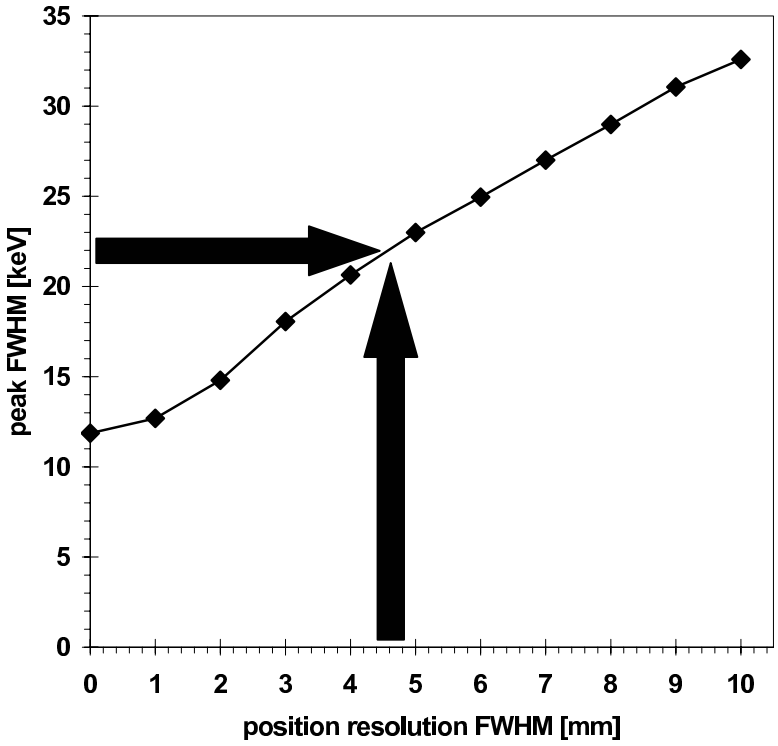

Figure 4.16: Simulated peak FWHM of the distribution in ϕ of the Compton reconstructed images as a function of the position resolution of the detector. The horizontal arrow indicates the experimental width. See text for details.

4.4 Discussion of the result

Similarly to the case of the in-beam experiment, it is not easy to evaluate the uncertainty on the present estimates of position resolution, obtained by projecting the image of figure 4.10 on the θ and ϕ axes. The statistics is quite limited and for this reason the present estimates should both be affected by an uncertainty of about 1 mm, thus resulting in mutual agreement. It should be pointed out that the average value of about 5 mm FWHM should be regarded as an average value for the interactions with a deposited energy ranging from 330 keV to 1 MeV. Therefore, considering that the position resolution depends on the energy deposition, the value obtained from the quality of the image reconstruction is compatible with the result of the in-beam experiment.

We believe that space is left for large improvements of this result using the developed PSA techniques described in section 3.7.1. We would like to remark again that the aim of this work was primarily to extract an estimate of the position resolution and not to study in depth the imaging capability of our segmented detector. It is clear however that imaging with the AGATA detectors is a promising field which is worthwhile exploring by means of the more refined algorithms used by the γ-ray imaging community.

Conclusion

The AGATA prototype triple cluster detector has been tested in an in-beam experiment performed in Summer 2005 at the Tandem accelerator of IKP Cologne. Data have been analysed using the grid search pulse shape analysis algorithm to find the individual photon interaction points. The comparison of the experimental results with a detailed Monte Carlo simulation suggests that the position resolution obtained in the present work is of the order of 5 mm for 1382 keV photons. Such value is considered adequate to reach the design performance of the AGATA array. The result from the in-beam experiment has been confirmed with a preliminary test of the imaging capabilities of the AGATA detectors.

Bibliography

[1] B. M. Nyakó, J. R. Cresswell, P. D. Forsyth, D. Howe, P. J. Nolan, M. A. Riley, J. F. Sharpey-Schafer, J. Simpson, N. J. Ward, P. J. Twin, Observation of Superdeformation in ^{152}Dy, Physical Review Letters 52 (1984) 507–510.

[2] B. Singh, R. Zywina, R. B. Firestone, Table of Superdeformed Nuclear Bands and Fission Isomers, Third Edition (October 2002), Nuclear Data Sheets 97 (2002) 241–592.

[3] P. F. Bortignon, A. Bracco, R. A. Broglia, Giant Resonances: Nuclear Structure at Finite Temperature, Harwood Academic Publishers, 1998.

[4] T. Tachibana, M. Uno, M. Yamada, S. Yamada, Empirical Mass Formula with Proton-Neutron Interaction, Atomic Data and Nuclear Data Tables 39 (1988) 251.

[5] J. Al-Khalili, An Introduction to Halo Nuclei, in: J. S. Al-Khalili, E. Roeckl (Eds.), The Euroschool Lectures on Physics with Exotic Beams, Vol. 651 of Lecture Notes in Physics, Berlin Springer Verlag, 2004, pp. 77–112.

[6] G. Audi, A. H. Wapstra, C. Thibault, The Atomic Mass Evaluation (II). Tables, graphs and references, Nuclear Physics A 729 (2003) 337–676.

[7] T. Otsuka, T. Matsuo, D. Abe, Mean Field with Tensor Force and Shell Structure of Exotic Nuclei, Physical Review Letters 97 (2006) 162501.

[8] M. A. Bentley, S. M. Lenzi, Coulomb energy differences between high-spin states in isobaric multiplets, Progress in Particle and Nuclear Physics 59 (2007) 497–561.

[9] A. G. M. van Hees, J. G. L. Booten, P. W. M. Glaudemans, Three-body forces and the description of light nuclei, Physical Review Letters 62 (1989) 2245–2248.

[10] J. Dobaczewski, I. Hamamoto, W. Nazarewicz, J. A. Sheikh, Nuclear shell structure at particle drip lines, Physical Review Letters 72 (1994) 981–984.

[11] R. F. Casten, New physics with radioactive beams: exotic structures in loosely bound systems, Journal of Physics G: Nuclear Physics 25 (1999) 747–753.

[12] S. Weinberg, Nuclear forces from chiral lagrangians, Physics Letters B 251 (1990) 288–292.

[13] D. B. Kaplan, A. V. Manohar, Nucleon-nucleon potential in the $1/N_c$ expansion, Physical Review Letters 56 (1997) 76–83.

[14] H. Grawe, A. Blazhev, M. Górska, I. Mukha, C. Plettner, E. Roeckl, F. Nowacki, R. Grzywacz, M. Sawicka, Shell structure from ^{100}Sn to ^{78}Ni: Implications for nuclear astrophysics, European Physical Journal A 25 (2005) 357–362.

[15] T. Otsuka, Shell model results for exotic nuclei, European Physical Journal A 20 (2003) 69–73.

[16] T. Otsuka, M. Honma, D. Abe, Effects of Spin-Isospin-Interactions on Nuclear Collective Motion, Nuclear Physics A 788 (2007) 3–11.

[17] T. Otsuka, T. Suzuki, R. Fujimoto, T. Matsuo, D. Abe, H. Grawe, Y. Akaishi, Evolution of shell and collective structures in exotic nuclei, Acta Physica Polonica B 36 (2005) 1213–1219.

[18] J. P. Schiffer, S. J. Freeman, J. A. Caggiano, C. Deibel, A. Heinz, C.-L. Jiang, R. Lewis, A. Parikh, P. D. Parker, K. E. Rehm, S. Sinha, J. S. Thomas, Is the Nuclear Spin-Orbit Interaction Changing with Neutron Excess?, Physical Review Letters 92 (2004) 162501.

[19] J. F. Berger, M. Girod, D. Gogny, Microscopic analysis of collective dynamics in low energy fission, Nuclear Physics A 428 (1984) 23–36.

[20] H. Grawe, New Vista of Shell Structure in Neutron-Rich Exotic Nuclei, Acta Physica Polonica B 34 (2003) 2267–2275.

[21] H. Grawe, M. Lewitowicz, Shell structure of nuclei far from stability, Nuclear Physics A 693 (2001) 116–132.

[22] A. Gadea, D. R. Napoli, G. de Angelis, R. Menegazzo, A. M. Stefanini, L. Corradi, M. Axiotis, L. Berti, E. Fioretto, T. Kroell, A. Latina, N. Marginean, G. Maron, T. Martinez, D. Rosso, C. Rusu, N. Toniolo, S. Szilner, M. Trotta, D. Bazzacco, S. Beghini, M. Bellato, F. Brandolini, E. Farnea, R. Isocrate, S. M. Lenzi, S. Lunardi, G. Montagnoli, P. Pavan, C. Rossi Alvarez, F. Scarlassara, C. Ur, N. Blasi, A. Bracco, F. Camera, S. Leoni, B. Million, M. Pignanelli, G. Pollarolo, A. Derosa, G. Inglima, M. La Commara, G. La Rana, D. Pierroutsakou, M. Romoli, M. Sandoli, P. G. Bizzeti, A. M. Bizzeti-Sona, G. Lo Bianco, C. M. Petrache, A. Zucchiatti, P. Cocconi, B. Quintana, C. Beck, D. Curien, G. Duchene, F. Haas, P. Medina, P. Papka, J. Durell, S. J. Freeman, A. Smith, B. Varley, K. Fayz, V. Pucknell, J. Simpson, W. Gelletly, P. Regan, Coupling a CLOVER detector array with the PRISMA magnetic spectrometer, European Physical Journal A 20 (2003) 193–197.

[23] A. M. Stefanini, L. Corradi, M. Trotta, A. Gadea, et al., The heavy-ion magnetic spectrometer PRISMA, in: J. Äystö, P. Dendooven, A. Jokinen, M. Leino (Eds.), Exotic Nuclei and Atomic Masses, 2003, p. 486.

[24] G. de Angelis, Future Perspectives in Nuclear Structure: From high intensity stable to radioactive nuclear beams, Nuclear Physics A 751 (2005) 533–551.

[25] G. de Angelis, Nuclear structure at the limits. Exploring the changing of shell structure with modern γ-ray detectors, Progress in Particle and Nuclear Physics 59 (2007) 409–417.

[26] S. Gales, SPIRAL2 at GANIL: A world leading ISOL facility at the dawn of the next decade, Progress in Particle and Nuclear Physics 59 (2007) 22–31.

[27] W. F. Henning, The future GSI facility, Nuclear Instruments and Methods in Physics Research B 214 (2004) 211–215.

[28] T. Motobayashi, RIKEN radioactive beam factory project, Progress in Particle and Nuclear Physics 42 (1999) 37–42.

[29] C. Gelbke, The National Superconducting Cyclotron Laboratory at Michigan State University: laboratory portrait, Nuclear Physics News 12 (2002) 5–14.

[30] H. J. Wollersheim, D. E. Appelbe, A. Banu, R. Bassini, T. Beck, F. Becker, P. Bednarczyk, K.-H. Behr, M. A. Bentley, G. Benzoni, C. Boiano, U. Bonnes, A. Bracco, S. Brambilla, A. Brunle, A. Burger, K. Burkard, P. A. Butler, F. Camera, D. Curien, J. Devin, P. Doornenbal, C. Fahlander, K. Fayz, H. Geissel, J. Gerl, M. Gorska, H. Grawe, J. Grebosz, R. Griffiths, G. Hammond, M. Hellstrom, J. Hoffmann, H. Hubel, J. Jolie, J. V. Kalben, M. Kmiecik, I. Kojouharov, R. Kulessa, N. Kurz, I. Lazarus, J. Li, J. Leske, R. Lozeva, A. Maj, S. Mandal, W. Meczynski, B. Million, G. Munzenberg, S. Muralithar, M. Mutterer, P. J. Nolan, G. Neyens, J. Nyberg, W. Prokopowicz, V. F. E. Pucknell, P. Reiter, D. Rudolph, N. Saito, T. R. Saito, D. Seddon, H. Schaffner, J. Simpson, K.-H. Speidel, J. Styczen, K. Summerer, N. Warr, H. Weick, C. Wheldon, O. Wieland, M. Winkler, M. Zieblinski, Rare ISotopes INvestigation at GSI (RISING) using gamma-ray spectroscopy at relativistic energies, Nuclear Instruments and Methods in Physics Research A 537 (2005) 637–657.

[31] B. Blank, M. Chartier, S. Czajkowski, J. Giovinazzo, M. S. Pravikoff, J.-C. Thomas, G. de France, F. de Oliveira Santos, M. Lewitowicz, C. Borcea, R. Grzywacz, Z. Janas, M. Pfützner, Discovery of Doubly Magic ^{48}Ni, Physical Review Letters 84 (2000) 1116–1119.

[32] E. Kugler, The ISOLDE facility, Hyperfine Interactions 129 (2000) 23–42.

[33] J. Cornell (editor), The EURISOL Report, GANIL, 2003.

[34] G. Prete (editor), SPES Technical Design for an Advanced Exotic Ion Beam Facility at LNL, INFN-LNL-220, 2007.

[35] C. Rossi-Alvarez, Nucl. Phys. News Europe 2 (1993) 10.

[36] D. Bazzacco, Proc. of Conf. on the Physics from Large γ-ray Detector Arrays, (Chalk River, Ontario, Canada) (1992) 376.

[37] M. A. Deleplanque, R. Diamond, Gammasphere proposal, Lawrence Berkley National Laboratory Report 5202.

[38] I. Y. Lee, The Gammasphere, Nuclear Physics A 520 (1990) 641.

[39] J. Simpson, The Euroball Spectrometer, Zeitschrift für Physik A Hadrons and Nuclei 358 (1997) 139.

[40] C. Rossi Alvarez, The EUROBALL array, Nuovo Cimento A Serie 111 (1998) 601.

[41] J. Gerl, W. Korten (editors), Technical proposal for the AGATA project, 2001.

[42] GRETA Steering Committee, Proposal for GRETINA, Lawrence Berkeley National Laboratory, 2003.

[43] C. W. Beausang, S. A. Forbes, P. Fallon, P. J. Nolan, P. J. Twin, J. N. Mo, J. C. Lisle, M. A. Bentley, J. Simpson, F. A. Beck, D. Curien, G. Defrance, G. Duchêne, D. Popescu, Measurements on prototype Ge and BGO detectors for the Eurogam array, Nuclear Instruments and Methods in Physics Research A 313 (1992) 37–49.

[44] J. Gerl, R. Lieder (editors), Euroball III, GSI Darmstadt, 1992.

[45] G. Duchêne, F. A. Beck, P. J. Twin, G. de France, D. Curien, L. Han, C. W. Beausang, M. A. Bentley, P. J. Nolan, J. Simpson, The Clover: a new generation of composite Ge detectors, Nuclear Instruments and Methods in Physics Research A 432 (1999) 90–110.

[46] M. Wilhelm, J. Eberth, G. Pascovici, E. Radermacher, H. G. Thomas, P. von Brentano, H. Prade, R. M. Lieder, The response of the Euroball Cluster detector to γ-radiation up to 10 MeV, Nuclear Instruments and Methods in Physics Research A 381 (1996) 462–465.

[47] T. Kröll, D. Bazzacco, Simulation and analysis of pulse shapes from highly segmented HPGe detectors for the γ-ray tracking array MARS, Nuclear Instruments and Methods in Physics Research A 463 (2001) 227–249.

[48] N. Warr, J. Eberth, G. Pascovici, H. G. Thomas, D. Weißhaar, MINIBALL: The first gamma-ray spectrometer using segmented, encapsulated germanium detectors for studies with radioactive beams, European Physical Journal A 20 (2003) 65–66.

[49] W. F. Mueller, J. A. Church, T. Glasmacher, D. Gutknecht, G. Hackman, P. G. Hansen, Z. Hu, K. L. Miller, P. Quirin, Thirty-two-fold segmented germanium detectors to identify γ-rays from intermediate-energy exotic beams, Nuclear Instruments and Methods in Physics Research A 466 (2001) 492–498.

[50] S. L. Shepherd, P. J. Nolan, D. M. Cullen, D. E. Appelbe, J. Simpson, J. Gerl, M. Kaspar, A. Kleinboehl, I. Peter, M. Rejmund, H. Schaffner, C. Schlegel, G. de France, Measurements on a prototype segmented Clover detector, Nuclear Instruments and Methods in Physics Research A 434 (1999) 373–386.

[51] P. Debye, X-ray interference patterns and atomic dimensions, Phys. Z. 31 (1930) 419–428.

[52] W. Franz, Rayleigh scattering of hard radiation by heavy atoms, Zeitschrift für Physik 98 (1935) 314–320.

[53] http://physics.nist.gov/PhysRefData/Xcom/Text/XCOM.html, Tech. rep.

[54] D. Bazzacco, The Advanced Gamma Ray Tracking Array AGATA, Nuclear Physics A 746 (2004) 248–254.

[55] G. J. Schmid, M. A. Deleplanque, I. Y. Lee, F. S. Stephens, K. Vetter, R. M. Clark, R. M. Diamond, P. Fallon, A. O. Macchiavelli, R. W. MacLeod, A γ-ray tracking algorithm for the GRETA spectrometer, Nuclear Instruments and Methods in Physics Research A 434 (1999) 481–481.

[56] A. Lopez-Martens, K. Hauschild, A. Korichi, J. Roccaz, J.-P. Thibaud, γ-ray tracking algorithms: a comparison, Nuclear Instruments and Methods in Physics Research A 533 (2004) 454–466.

[57] G. F. Knoll, Radiation detection and measurement, Radiation detection and measurement. 3rd ed. New York, NY: Wiley, 2000. xiv, 802 p. ISBN 0471073385, 2000.

[58] 5^{th} AGATA week Orsay, 15-19 / 01 / 2007.

[59] M. Dimmock, 5^{th} AGATA week Orsay, 15-19 January 2007.

[60] L. Nelson, M. R. Dimmock, A. J. Boston, H. C. Boston, J. R. Cresswell, P. J. Nolan, I. Lazarus, J. Simpson, P. Medina, C. Santos, C. Parisel, Characterisation of an AGATA symmetric prototype detector, Nuclear Instruments and Methods in Physics Research A 573 (2007) 153–156.

[61] T. M. Hoa, A. Korichi, 5^{th} AGATA week Orsay, 15-19 January 2007.

[62] S. Tashenov, 5^{th} AGATA week Orsay, 15-19 January 2007.

[63] W. Shockley, Currents to Conductors Induced by a Moving Point Charge, Journal of Applied Physics 9 (1938) 635–636.

[64] S. Ramo, Currents induced by electron motion, in: Proceedings of the I.R.E., 1939, p. 584.

[65] E. Gatti, G. Padovini, V. Radeka, Signal evaluation in multielectrode radiation detectors by means of a time dependent weighting vector, Nuclear Instruments and Methods 193 (1982) 651–653.

[66] V. Radeka, Low-noise techniques in detectors, Annual Review of Nuclear and Particle Science 38 (1988) 217–277.

[67] P. Medina, C. Santos, D. Villaumt, A Simple Method for the Characterization of HPGe Detectors, in: Proc. of Instrumentation and Measurement Technology Conference, 2005.

[68] Geant4 Collaboration, Geant4 - a simulation toolkit, Nuclear Instruments and Methods in Physics Research A 506 (2003) 250–303.

[69] E. Farnea, D. Bazzacco, A Monte Carlo code for the AGATA array, LNL-INFN(REP) 202 (2004) 158–159.

[70] E. Farnea,
http: / / agata.pd.infn.it / documents / simulations / comparison.html.

[71] J. Eberth, H. G. Thomas, P. V. Brentano, R. M. Lieder, H. M. Jäger, H. Kämmerling, M. Berst, D. Gutknecht, R. Henck, Encapsulated Ge detectors: development and first tests, Nuclear Instruments and Methods in Physics Research A 369 (1996) 135–140.

[72] A. Görgen, The position sensitivity of the AGATA prototype crystal analyzed using a database of calculated pulse shape., http://www-dapnia.cea.fr/Sphn/Deformes/Agata/local/files/report.pdf.

[73] M. Bellato, 5^{th} AGATA week Orsay, 15-19 January 2007.

[74] A. Georgiev, W. Gast, Digital pulse processing in high resolution, high throughput, gamma-ray spectroscopy, IEEE Transactions on Nuclear Science 40, Issue: 4, Part 1-2 (1993) 770–779.

[75] W. Gast, R. Lieder, L. Mihailescu, M. Rossewij, H. Brands, A. Georgiev, J. Stein, T. Kröll, Digital signal processing and algorithms for γ-ray tracking, IEEE Transactions on Nuclear Science 48, Issue: 6 (2001) 2380–2384.

[76] A. Pullia, F. Zocca, G. Pascovici, An Advanced Preamplifier for Highly Segmented Germanium Detectors, IEEE Transactions on Nuclear Science 53, Issue: 5, Part 2 (2006) 2869–2875.

[77] F. Zocca, New technologies for low-noise wide-dynamic-range preamplification of HPGe segmented detector signals, Ph.D. thesis, Università degli Studi di Milano (2008).

[78] T. Steinhardt, D. Weisshaar, J. Eberth, O. Thelen, H. Hess, A First In-Beam-Experiment with the 36-fold Segmented AGATA-Detector. 3^{rd} AGATA week Strasbourg, 21-25 November 2005.

[79] D. Weisshaar, MINIBALL: Ein neuartiges Gamma-Spektrometer mit ortsauflösenden Germaniumdetektoren, Ph.D. thesis, IKP Köln (2002).

[80] T. Kröll, D. Bazzacco, R. Venturelli, B. Quintana, C. A. Ur, M. Bellato, R. Isocrate, C. Manea, R. Menegazzo, P. Pavan, C. R. Alvarez, E. Farnea, A. Gadea, D. Rosso, P. Spolaore, F. Camera, B. Million, E. Musso, A. Pullia, O. Wieland, G. Casati, A. Geraci, G. Ripamonti, M. Descovich, Gamma-ray Tracking With The MARS Detector, in: P. Fallon, R. Clark (Eds.), Frontiers of Nuclear Structure, Vol. 656 of American Institute of Physics Conference Series, 2003, pp. 357–364.

[81] T. Kröll, D. Bazzacco, R. Venturelli, M. Nespolo, B. Quintana Arnés, C. Ur, M. Bellato, R. Isocrate, C. Manea, R. Menegazzo, P. Pavan,

C. Rossi Alvarez, E. Farnea, A. Gadea, D. Rosso, P. Spolaore, B. Million, A. Pullia, O. Wieland, A. Geraci, G. Ripamonti, M. Descovich, In-beam experiment with the γ-ray tracking detector MARS, Nuclear Instruments and Methods in Physics Research A Article in Press.

[82] M. Descovich, I. Y. Lee, P. Fallon, M. Cromaz, A. O. Macchiavelli, D. C. Radford, K. Vetter, R. M. Clark, M. A. Deleplanque, F. S. Stephens, D. Ward, In-beam measurement of the position resolution of a highly segmented coaxial germanium detector, Nuclear Instruments and Methods in Physics Research A 553 (2005) 535–542.

[83] J. F. Ziegler, SRIM-2003, Nuclear Instruments and Methods in Physics Research B 219 (2004) 1027–1036.

[84] H. Essel, N. Kurz et al., The GSI Multi Branch System. See also http://www.gsi.de, Tech. rep.

[85] B. Hubbard-Nelson, M. Momayezi, W. K. Warburton, A module for energy and pulse shape data acquisition, Nuclear Instruments and Methods in Physics Research A 422 (1999) 411–416.

[86] V. T. Jordanov, G. F. Knoll, Digital synthesis of pulse shapes in real time for high resolution radiation spectroscopy, Nuclear Instruments and Methods in Physics Research A 345 (1994) 337–345.

[87] R. Venturelli, D. Bazzacco, M. Bellato, A. Pullia, T. Kröll, Fold-dependent energy correction in segmented germanium detectors, LNL-INFN(REP) 198 (2003) 156–157.

[88] B. Bruyneel, P. Reiter, G. Pascovici, Characterization of large volume HPGe detectors. Part II: Experimental results, Nuclear Instruments and Methods in Physics Research A 569 (2006) 774–789.

[89] B. Bruyneel, Characterization of Segmented Large Volume, High Purity Germanium Detectors, Ph.D. thesis, Cologne University (2006).

[90] B. Bruyneel, 6^{th} AGATA week Legnaro, 12-16 November 2007.

[91] D. Bazzacco, S. Aydin, private communication.

[92] R. L. Chase, Pulse Timing System for Use with Gamma Rays on Ge(Li) Detectors, Review of Scientific Instruments 39 (1968) 1318–1326.

[93] Z. H. Cho, R. L. Chase, Comparative study of the timing techniques currently employed with Ge detectors, Nuclear Instruments and Methods 98 (1972) 335.

[94] R. Brun, F. Rademakers, ROOT - An object oriented data analysis framework, Nuclear Instruments and Methods in Physics Research A 389 (1997) 81–86.

[95] A. Gavron, Statistical model calculations in heavy ion reactions, Phys. Rev. C 21 (1980) 230–236.

[96] F. Pühlhofer, On the interpretation of evaporation residue mass distributions in heavy-ion induced fusion reactions, Nuclear Physics A 280 (1977) 267–284.

[97] E. Farnea, F. Recchia, D. Bazzacco, N. Marginean, O. Stezowski, Results from the Monte Carlo simulations for the AGATA array, LNL-INFN(REP) 204 (2005) 218–219.

[98] O. Stezowski, http:/ / agata.in2p3.fr.

[99] R. Venturelli, D. Bazzacco, Adaptive grid search as pulse shape analysis algorithm for γ-tracking and results, LNL-INFN(REP) 204 (2005) 220–221.

[100] R. Venturelli, 5^{th} AGATA week Orsay, 15-19 January 2007.

[101] P. Désesquelles, C. Diara, P. Médina, A. Olariu, C. Parisel, C. Santos, Real Time Pulse Shape Analysis for the γ-Interactions in AGATA, Real Time Conference, 2005. 14th IEEE-NPSS.

[102] J. Ljungvall, 5^{th} AGATA week Orsay, 15-19 January 2007.

[103] F. C. L. Crespi, F. Camera, O. Wieland, G. Benzoni, S. Brambilla, B. Million, D. Montanari, A pulse shape analysis algorithm for HPGe detectors, Nuclear Instruments and Methods in Physics Research A 570 (2007) 459–466.

[104] F. Crespi, 5^{th} AGATA week Orsay, 15-19 January 2007.

[105] M. Descovich, P. J. Nolan, A. J. Boston, J. Dobson, S. Gros, J. R. Cresswell, J. Simpson, I. Lazarus, P. H. Regan, J. J. Valiente-Dobon, P. Sellin,

C. J. Pearson, The position response of a large-volume segmented germanium detector, Nuclear Instruments and Methods in Physics Research A 553 (2005) 512–521.

[106] H. Anger, A new instrument for mapping gamma-ray emitters, Biology and Medicine Quarterly Report, University of California Radiation Laboratory, Berkeley, 1957.

[107] M. N. Wernick, J. N. Aarsvold, Emission Tomography: The Fundamentals of PET and SPECT, Elsevier, 2004.

[108] K. Pinkau, Die Messung solarer und atmosphärischer Neutronen, Zeitschr. f. Naturforschg. 21a (1966) 2100.

[109] R. S. White, An experiment to measure neutrons from the sun, Bulletin of American Physics Society 13 II (1968) 714.

[110] Y. Du, Z. He, G. F. Knoll, D. K. Wehe, W. Li, Evaluation of a Compton scattering camera using 3D position-sensitive CdZnTe detectors, in: R. B. James, R. C. Schirato (Eds.), Proc. SPIE Vol. 3768, p. 228-238, Hard X-Ray, Gamma-Ray, and Neutron Detector Physics, Ralph B. James; Richard C. Schirato; Eds., Vol. 3768 of Presented at the Society of Photo-Optical Instrumentation Engineers (SPIE) Conference, 1999, pp. 228–238.

[111] L. Arnold, R. Baumann, E. Chambit, M. Filliger, C. Fuchs, C. Kieber, D. Klein, P. Medina, C. Parisel, M. Richer, C. Santos, C. Weber, TNT Digital Pulse Processor, Real Time Conference, 2005. 14th IEEE-NPSS (2005) 265–269.

Ringraziamenti

Dino Bazzacco mi ha guidato e aiutato in questo lavoro di analisi. Lo ringrazio per gli insegnamenti, le stimolanti discussioni e soprattutto per l'esempio trasmessomi.

Enrico Farnea è stato fondamentale nella stesura di questa tesi, senza di lui non ci sarebbe. Un grazie enorme per la simulazione, che ho largamente usato in questo lavoro, per tutto il tempo dedicatomi e per l'inesauribile disponibilità.

Ringrazio Santo Lunardi per aver supervisionato e corretto questa tesi; Roberto Venturelli per il suo programma di PSA, per le molte idee ed il suo differente punto di vista. Un grazie a Calin Ur per la sua disponibilità. Ringrazio Andres, Nicu, Sezgin, Gabi e tutta la collaborazione PRISMA-CLARA, con cui ho avuto il piacere di lavorare. *I'd like to thank the AGATA group at IKP Cologne for the setup of the triple cluster experiment.*

Parte di questo lavoro è stato svolto grazie a una borsa di studio "Tracciamento gamma e capacità di imaging dei rilevatori al germanio dello spettrometro di nuova generazione AGATA", finanziata dalla Cassa di Risparmio di Padova e Rovigo, parte grazie a un contratto EUROpean Nuclear Structure n.506065. Ringrazio Enrico Fioretto per il suo continuo aiuto nei rapporti con EURONS.

Uno speciale grazie a mia madre e mia sorella per essermi state vicine e per aver creduto in me e a mio padre, il mio primo maestro di matematica, per avermi trasmesso curiosità per la scienza.

A Beatrice per il suo amore.